Coastal meltwater plume detection and its response to melting variations around the Greenland Ice Sheet

Wenkai Guo

12 June 2015

This dissertation is submitted for the degree of Master of Philosophy.

DECLARATION

This dissertation is the result of my own work and includes nothing which is the outcome of work done in collaboration except where specifically indicated in the text. The dissertation is no more than 20,000 words in length excluding the declaration, acknowledgements, list of references, tables, captions and appendices.

i. Abstract

Meltwater runoff is an important component of the mass balance of the Greenland ice sheet and is usually assessed using climate-mass balance models. In-situ measurements of runoff from the outlets are rare, and remote sensing platforms capable of monitoring runoff in rivers, lakes and fjords are in their infancy. Thus, there is a need to investigate new methods of observing meltwater losses. Preliminary studies have been conducted correlating measured meltwater discharge to different characteristics of plumes containing suspended sediment in fjords retrieved from remote sensing. However, suspended sediments are not directly representative of meltwater leaving the ice sheet, and later in the melt season the meltwater may have a very low sediment load due to exhaustion in sediment supply. Also, the spatial resolution of Moderate Resolution Imaging Spectroradiometer (MODIS) imagery used in these studies limits the accuracy of sediment plume retrieval, especially in areas of pervasive iceberg and sea ice cover.

For non-glacial environments, there have been successful attempts at delineating freshwater plumes in the ocean by their surface salinity and thermal signatures achieved from satellite imagery. For my MPhil dissertation, I propose to use multi-year Landsat data to derive a time series of water plume location, size and shape using proxies for identifying suspended sediment, salinity and thermal signals in several fjords in Greenland. Seasonal and inter-annual variations in the location, size and shape of the various plumes will then be compared against variations in ice-sheet melt extent achieved from Special Sensor Microwave/Imager (SSM/I) passive microwave data and cumulative melt derived from a positive degree model in order to examine the correlations between ice sheet melting and the delivery of water to the ice sheet margins.

ii. Table of Contents

iii. List of Figures

iv. List of Tables

v. Acknowledgements

I am first and foremost very grateful to my supervisor, Dr. Ian Willis, for his kind and continuous help on this project and on my MPhil studies in general. Dr. Neil Arnold provided constructive comments on this dissertation study. Dr. Gareth Rees provided great help in creating a detailed plan for my future PhD project. Dr. Mike Bithell offered helpful suggestions on using the IDL language in data processing.

I was partially funded by the Cambridge Trust Scholarship during my MPhil study, which was a tremendous financial help to get me through the course.

I would like to thank all the staff members and students at Scott Polar Research Institute for their continuous support and valuable suggestions to my project and my studies. I am also deeply grateful for the instructive courses provided by the Institute which exposed me to the frontier of polar research. I have found the Institute to be a friendly and intellectually stimulating place to study in, and the last year has been a valuable and rewarding experience to me, both personally and academically.

1. INTRODUCTION

The Greenland ice sheet (GrIS) has been known to respond most drastically to ongoing global climate change, and has been identified as one of the most sensitive and vulnerable "tipping elements" of global warming. The ice sheet contains enough water to raise sea level by 7 meters, and has been warming by approximately 2 ℃ per year since the 1990s, and is projected to further warm by 2 to 12 ℃ in the twenty-first century (Hanna et al. 2011). It has responded to rising global temperatures by enhanced melting and increased ice loss rates over the last 50 years (Fettweis et al. 2013). There has been an acceleration of $21.9 \pm 1\ \mathrm{Gt/yr^2}$ in Greenland ice sheet mass loss over the 1992 to 2011 period (Rignot et al. 2011), and since 2007, successive summers with record surface melt rates have been observed over the ice sheet (Tedesco et al. 2008; Tedesco et al. 2011; Tedesco et al. 2013). In the 2012 extreme melting event, more than 97% of the ice sheet surface area experienced melting, which is a record melt extent (Tedesco et al. 2013; Hanna et al. 2013). A total mass loss of 474 Gt between June 2012 and June 2013 was reported by NASA's Gravity Recovery and Climate Experiment (GRACE) record (Tedesco et al. 2015).

The Greenland ice sheet loses mass through two primary mechanisms: surface melting and ice discharge (Figure 1). Mass loss from these two processes have been found to be of similar significance (Hanna et al. 2005; van den Broeke et al. 2009; Rignot et al. 2011). Part of the meltwater is retained within the snowpack through refreezing (Fountain 1996; Hanna et al. 2005; Parry et al. 2007) to form superimposed ice at lower altitudes or wetted-refrozen snow and ice lenses at higher altitudes (Wadham & Nuttall 2002), or stored inside supra- or sub-glacial lakes and river channels (Jansson et al. 2003). Simulations show that, in total, 42±4% or rain and meltwater is retained or refrozen in the firn layer (Van Angelen et al. 2013).

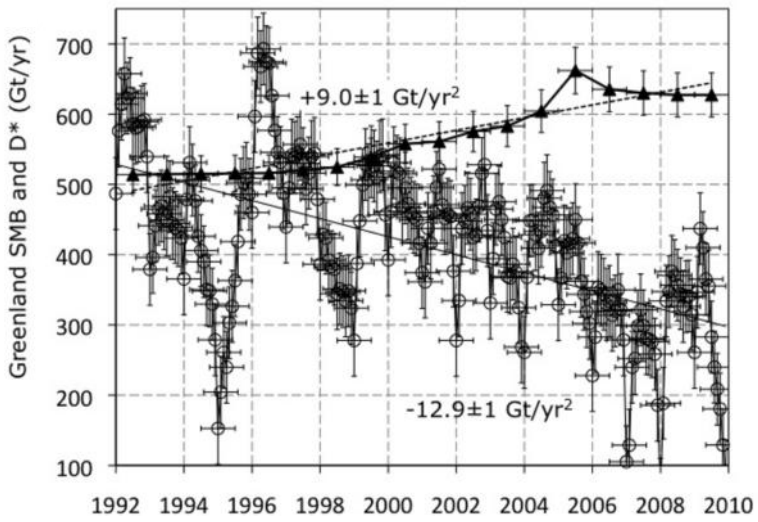

Figure 1 Monthly surface mass balance (open circle) and yearly ice discharge compensated for grounding line retreat (solid triangle) for Greenland. (From Rignot et al., 2011)

The rest of the meltwater becomes runoff into the ocean. Accurate estimates of Greenland's potential contribution to the global sea level rise requires constraints on meltwater output. However, due to scarcity of consistent and direct observations of fresh water leaving the ice sheet, it is difficult to incorporate meltwater runoff accurately into current mass balance models. Direct proglacial discharge measurements exists only for a few glacier outlets in Greenland, e.g. the Watson River station in Kangerlussuaq, West Greenland (Mernild et al. 2008; Mernild & Hasholt 2009), Skeldal River, northeast Greenland (Stott & Grove 2001) and Leverett Glacier, West Greenland (Bartholomew et al. 2011), and these measurements are usually for relatively short time periods due to the difficulty in installing and maintaining the gauging station networks in the ice sheet periphery (McGrath et al. 2010). Currently, most ice sheet mass balance studies have relied upon the modelling of surface meltwater retention (e.g. Hock 2005; van den Broeke et al. 2009), and existing research of meltwater release also largely consist of modelling studies (Lewis & Smith 2009; Mernild et al. 2010; Mernild et al. 2011).

Therefore, there is currently a need for reliable retrieval of meltwater runoff information in a wider spatial scale and over a longer time span, which is only achievable through the use of remote sensing techniques. Since remote sensing platforms capable of directly monitoring lake and river fluctuations are still yet to be developed (Chu et al. 2009), studies have been seeking 'proxies' for meltwater runoff that can be readily detected and monitored remotely. In alpine glaciers, it has been found that pulses of meltwater runoff are usually followed by increases in suspended sediment concentration in proglacial environments (Fenn 1987). It has long been found that these sediments are these sediments are easily quantifiable through visible/near infrared remote sensing (e.g. Doxaran et al. 2002; Miller & McKee 2004). Chu et al. (2009) found correlation between ice sheet melt extent and remotely sensed estuary sediment plumes, confirming the origin of the sediment plume to be ice sheet meltwater release. Later studies (2010) have also found correlation between plume length and river discharge. Thus, remote sensing of sediment plume behaviour proves to be a reasonable tool for monitoring the variability of ice sheet meltwater release.

It should be noted, however, that these studies have all utilized information from one spectral band from the Moderate Resolution Image Spectroradiometer (MODIS) in the identification of sediment plumes, and the band threshold used to quantify plume area is derived from site-specific studies of the relationship between band reflectance and suspended sediment concentration (SSC). This can potentially lead to false identification of sediment plumes when applied elsewhere. Moreover, the single band threshold approach in plume delineation can be problematic in late melt season when exhaustion in sediment supply may occur. Also, the spatial resolution of MODIS at 250m is relatively coarse for the study of sediment plumes especially in narrower glacier outlets around Greenland. In non-glacial environments, studies have attempted to use different physical variables to delineate freshwater plumes in coastal regions (e.g. Hopkins et al. 2013) with various varying degrees of success. Remote sensing of many of these

variables utilize information from multiple satellite bands which could potentially provide a more robust way of freshwater plume delineation.

1.1. Aims

The aims of this study are:

a. To evaluate the feasibility and reliability of using other variables previously used in studies of non-glacial environments rather than suspended sediment to detect the presence of freshwater output from glacier outlets.
b. To develop and experiment with different kinds of adaptive plume delineation algorithms that takes the characteristics of different study sites into consideration instead of applying single pre-determined band threshold in the extraction of freshwater plumes.
c. To use higher-resolution remote sensing imagery to better delineate and quantify freshwater plume extent.
d. To evaluate the proposed variables and algorithms over a wide range of glacier outlet environments in Greenland and examine their performance against plume delineation approaches in previous studies. This can be achieved by inter-comparison between freshwater plume delineation results from different methods, as well as comparing the derived plume area time series to melt extent variations in the catchment areas.

2. BACKGROUND

2.1. Remote sensing of meltwater runoff using suspended sediment plume

In non-glacial settings, there have been considerable efforts in the remote sensing of suspended matter in coastal waters (e.g. Ritchie et al. 1990; Doxaran et al. 2002; Miller & McKee 2004; Petus et al. 2010; Zhang et al. 2010). Chu et al. (2009) proposed the possibility of using downstream sediment plume, which is easily detectable from moderate-resolution satellite images, to represent variations in ice sheet surface hydrology, and successfully linked sediment plume area and suspended sediment concentration to surface melting variations in Kangerlussuaq Fjord, West Greenland. McGrath et al. (2010) found positive correlation between sediment plume length and observed water discharge also in the Kangerlussuaq Fjord, and then successfully used plume length to reconstruct cumulative discharge in 2007 and 2008. In a later study of fjords around ~80% of Greenland from 2000 to 2009, Chu et al. (2012) found significant geographic covariance but low temporal covariance between fjord suspended sediment concentration (SSC) levels and ice sheet melt, suggesting that plume dimensions instead of SSC best captures inter-annual runoff dynamics, while SSC is best used to capture variations in meltwater signals across different study areas. Tedstone et al. (2012) developed an automated sediment plume quantification system which identifies coherent plumes using spectral thresholds and polygon tracing, and applied the algorithm in deriving a time series of plume areas in 36 outlets along the West Greenland coast from 2000 to 2007. These studies have all utilized empirical relationships between the Red spectral band (0.62-0.67 μm) and SSC (an example is shown in the following figure) to detect sediment plumes, and uses a band 1 reflectance threshold in determining plume extent.

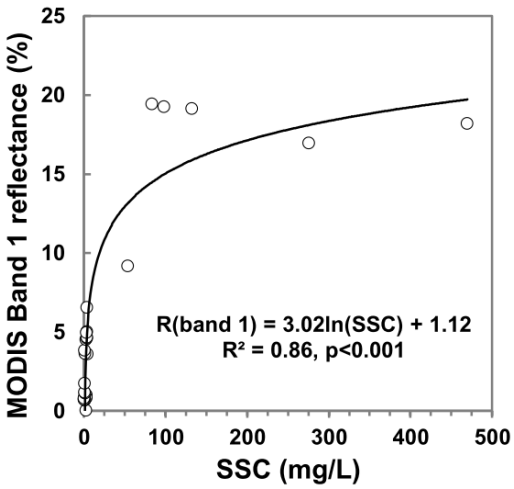

Figure 2 Empirical relationship between field SSC and MODIS band 1 reflectance derived from Kangerlussuaq Fjord. (From Chu et al., 2012)

These efforts have demonstrated the ability of sediment plumes to be used as an indicator of meltwater runoff, and currently sediment plumes have been identified as being a proxy for meltwater runoff that integrates poorly constrained processes including meltwater refreezing and supra- and en-glacial water storage (McGrath et al. 2010). However, limitations exist in current techniques of sediment plume extraction. Firstly, previous studies have relied on arbitrary thresholds of only one spectral band to determine the boundaries between sediment plumes, brackish plumes and ocean waters (Chu et al. 2009; McGrath et al. 2010; Chu et al. 2012; Tedstone & Arnold 2012), and a single threshold derived from regional studies is applied to multiple different glacier outlets in different time periods which can potentially have varied physical conditions such as different outlet geometry and different availability of sediment in the catchment area, etc., that can lead to different spectral responses from the sediment plumes, and thus possible misclassification of the different water types. Secondly, these studies have used MODIS imagery in the derivation of sediment plume extent. However, the 250m spatial resolution of MODIS images may not be sufficient to correctly characterize sediment plumes especially in smaller outlets. Thirdly, site studies as well as remote sensing studies have reported

late melt season exhaustion of sediment supply which results in freshwater output with very low or undetectable amount of suspended sediments. This is represented by a seasonal hysteresis between melt extent and plume area (Chu et al. 2009; Tedstone & Arnold 2012). This phenomenon has also been captured on a daily time scale, as shown in the following figure, in which SSC level drops earlier in the day than discharge (Stott & Grove 2001). Therefore, a more 'natural' thresholding technique on a higher-resolution record of a better indicator of meltwater discharge can greatly benefit the detection and monitoring of freshwater output from Greenland's many glacier outlets.

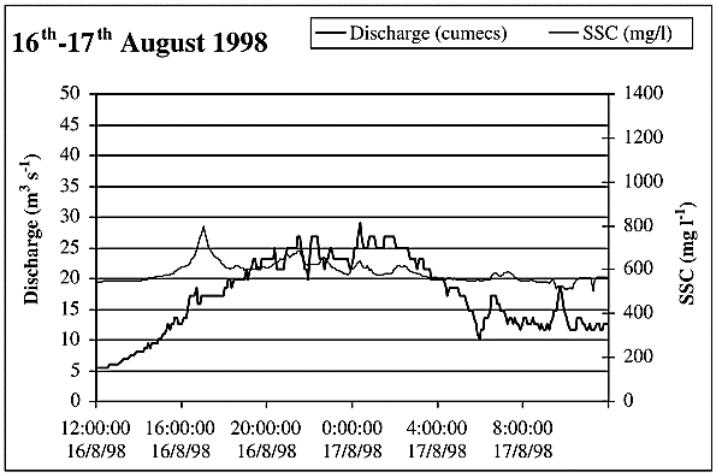

Figure 3 Discharge and SSC variation in the proglacial Skeldal River, north-east Greenland, from 16th to 17th in August 1998. (From Stott & Grove, 2001).

2.2. Remote sensing of freshwater output using other proxies

The direct way of detecting freshwater output from coastal regions is the monitoring of water surface fluctuations. For example, A recent study (Legleiter et al. 2014) uses spectrally based bathymetry mapping of supraglacial lakes and streams from WorldView2 (WV2) images to estimate Greenland's surface meltwater volume, which can potentially be used to provide estimates of transient meltwater fluxes through streams. However, current spaceborne platforms are only able to measure a few of the components of surface hydraulics, and no existing platform

is capable of singularly supplying the water volume and hydraulic measurements necessary to accurately calculate the water cycle, especially discharge. For example, profiling altimeters and the Gravity Recovery and Climate Experiment (GRACE) provides broad spatial coverage of surface elevation but lack spatial resolution; radar altimetry serves as an accurate technology to collect water surface elevation, but its data is only available along orbital profiles and thus misses the majority of the water surface; interferometric processing of synthetic aperture radar (InSAR) provides high resolution image of water level changes through time but requires vegetation to scatter back radar pulses (Kim et al. 2005); the Shuttle Radar Topography Mission (SRTM) collects images of water levels at a high spatial resolution, but its poor temporal resolution and significant errors over water surfaces limits its hydrological usage. More fundamentally, remote detection of water discharge needs measurement of the configuration of cross-sectional river channel geometry that requires high resolution satellite bathymetry which is currently unattainable. A satellite mission addressing all these issues and providing maps of global water storage changes at a reasonable spatial and temporal resolution is still yet to be undertaken (Alsdorf et al. 2007).

Another approach of remotely quantifying meltwater output is through various ‘proxies’ of fresh water that are more readily detectable using remote sensing methods. Apart from suspended sediments, studies have been using other signals in identifying freshwater plumes from rivers into the oceans. In a study of deep water upwelling in pine island bay, Antarctica, Landsat Enhanced Thematic Mapper Plus (ETM+) thermal infrared image reveals plume-like features from glacier outlets, as seen in the following figure. (Mankoff et al. 2012).

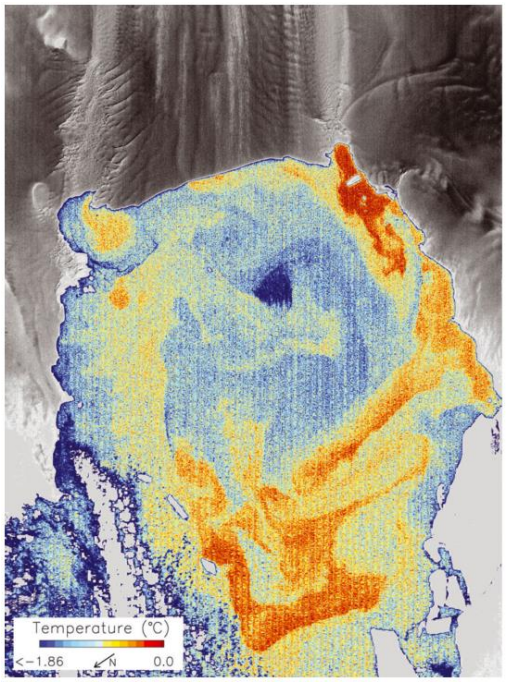

Figure 4 Landsat ETM+ thermal infrared image of Pine Island Bay and the Pine Island Glacier ice shelf, acquired 16 November 2008. Outflows from beneath the ice shelf have become entrained and mix in a large cyclonic gyre in Pine Island Bay. (From Mankoff et al, 2012)

Hopkins et al. (2013) used sea surface temperature, salinity, chlorophyll concentration (from ocean colour data) and sea level anomalies to detect the Congo River plume into the ocean. Due to the large spatial extent of the plume, the analysis is undertaken at coarse resolutions (0.25 degree for sea surface temperature and salinity data, 0.04 degree for chlorophyll images and 1/3 degrees for mean sea level anomaly data). Salinity and surface chlorophyll levels obtained from ocean colour datasets are reported to yield the strongest and most identifiable plume-like signatures:

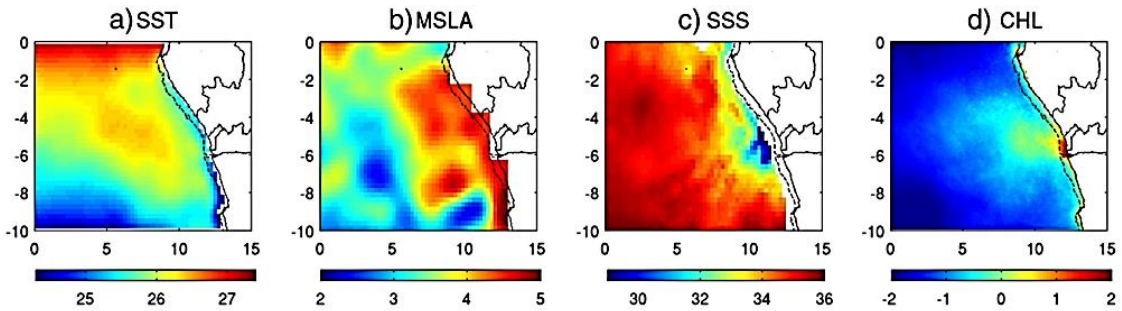

Figure 5 (a-d) Mean Sea Surface Temperature (SST, ℃), Mean Sea Level Anomaly (MSLA, cm), Sea Surface Salinty (SSS, pss) and Chlorophyll level (CHL, mg/m-3). (From Hopkins et al., 2013)

It can be inferred from these studies that a set of different variable detectable from satellite remote sensing can serve as potential proxies for meltwater output from river channels into the ocean, though most studies involving actual quantification of plume extents from these variables take place in non-glacial settings. Theoretically, this principle can easily be transferred into the study of Greenland meltwater output. However, given the relatively small spatial extent of glacial outlets in the GrIS compared to the above studies, the feasibility of using each of these variables to represent meltwater plumes requires further examination.

2.3. Selection of alternative indicators of meltwater output from the GrIS

In this section, the feasibility of utilizing several kinds of satellite data to represent Greenland meltwater output is assessed. Firstly, as discussed earlier, currently there is no available remote sensing altimetry system with sufficient spatial and temporal resolution to monitor river height changes in Greenland's glacier outlets in order to infer freshwater runoff. Secondly, although chlorophyll levels near the Greenland coasts are detectable and able to be monitored from space (Heide-Jørgensen et al. 2007), it is usually retrieved from ocean colour products from sensors with coarser resolution (e.g. MODIS: 250m resolution; MEdium Resolution Imaging Spectrometer (MERIS): 260m by 300m for land and coastal regions) than

desirable in this study. Even though efforts have been made to map chlorophyll levels from Landsat imagery (Bartholomew 2002; Torbick et al. 2008; Turner 2010), they have relied upon site-specific derivation of empirical relationship between chlorophyll levels and simple Landsat band ratios, which is therefore not considered robust methods of representing freshwater output across various outlet environments in Greenland.

Thirdly, thermal signal can theoretically be used to trace freshwater output from glacier outlets as meltwater runoff is expected to have a lower temperature than the ocean water in the fjords or bays. Landsat 8 TIRS and Landsat 7 ETM+ thermal band images can be converted to brightness temperature values following the procedures in the Landsat Handbook, which is automated in the ENVI 5.1 software package. An initial check at the brightness temperature data confirms this hypothesis, as can be seen from Figure 6 in which darker-coloured freshwater plume (lower temperatures) is visible near the outlets. However, experimental thresholding on the brightness temperature data shows difficulty in delineating reasonably coherent plume-like features (as seen in Figure 6). This is presumably due to faster mixing of waters of different temperatures than suspended sediments which may persist longer in a coherent and detectable plume. Also, although Landsat 7 and 8 thermal bands have a nominal spatial resolution of 30m, they have been resampled from 60m (Landsat 7 ETM+) and 100m (Landsat 8 TIRS) resolution, which further limits the ability of thermal signal in effectively characterizing freshwater plumes. Therefore, thermal signal from Landsat imagery is also considered an unstable proxy of meltwater output and not included in the analysis.

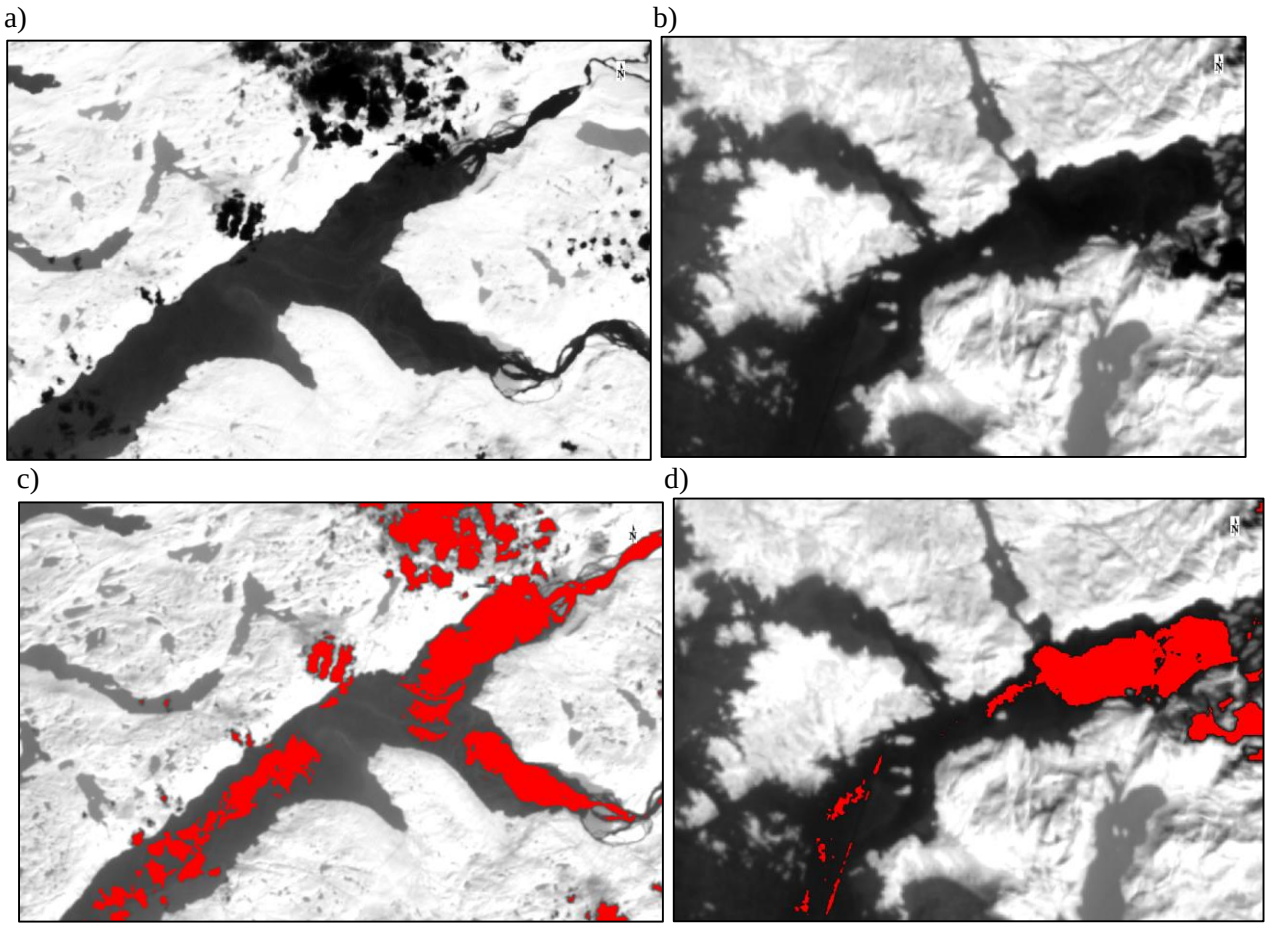

Figure 6 (a-b) Example of a Landsat 8 scene segment showing Outlet 1 (19/7/2014) and Outlet 2 (8/8/2014) calibrated to brightness temperature. (Lighter colour indicates higher brightness temperature). (c-d) Experimental thresholding of the brightness temperature images in an attempt to delineate plume-like features (in red). Temperature threshold for c): <276 Kelvin; temperature threshold for d): <273 Kelvin.

Finally, salinity signal seems intuitively to be a reasonable variable for the separation of meltwater output and the more salty ocean water. Remote sensing platforms directly capable of detecting sea surface salinity include European Space Agency's (ESA's) Soil Moisture and Ocean Salinity Mission and National Aeronautics and Space Administration's (NASA's) Aquarius satellite, but due to their coarse spatial resolution of 35km (at centre of field of view) and 150km, respectively, both of them cannot be used for delineating freshwater characteristics in Greenland's narrow outlets. Indirect retrieval methods of sea surface salinity (SSS) from various other remote sensing platforms also exist. One type of method derives salinity from

reflectance values of different satellite bands using numerical modelling e.g. multiple regression (Marghany & Hashim 2011), tree-based data mining and artificial neural network, etc. (Urquhart et al. 2012), using MODIS as well as Landsat imagery (Wang & Xu 2008). However, these methods again rely upon in-situ measurements in the development of a statistical relationship between band values and salinity, resulting in site-specific salinity retrieval models.

Another type of modelling approach tries to exploit the observed inverse relationship between surface salinity and coloured dissolved organic matter (CDOM) in coastal regions (Monahan & Pybus 1978; Bowers et al. 2000), which is likely due to conservative mixing of CDOM-rich freshwater runoff with ocean water (Palacios et al. 2009). CDOM is an important pool of absorbing substances in water bodies originated from humic substances on land transported through meltwater runoff and therefore is much more abundant in coastal and estuary areas (Ahn et al. 2008). CDOM is characterized by strong absorption of ultraviolet (UV) and blue light than other visible light, and many robust remote sensing algorithms have been developed to derive its absorption coefficient, a_{CDOM}, from satellite imagery that are applicable to a range of water bodies (e.g. Carder et al. 1999; Mannino et al. 2008; Griffin et al. 2011; Ficek et al. 2011). However, the process of deriving salinity from satellite estimates of a_{CDOM} still requires site measurements from which a regression model can be established. Given these limitations, this study explores the possibility of using a_{CDOM} directly as a proxy for freshwater plume delineation. There are currently no published a_{CDOM} values from Greenland ice sheet meltwater, but in a recent study, an $a_{CDOM}(350)$ (CDOM absorption coefficient at 350nm wavelength) level of 0.12 m^{-1} has been reported (Stedmon et al. 2015). Although this level is relatively low compared to coastal regions in lower latitudes, it can be detected using currently available remote sensing algorithms (Zhu et al. 2014).

3. DATA AND METHODS

3.1. Study area

Four glacier outlets in west Greenland are picked in order to test and examine the performance of the proposed freshwater delineation methods, as shown in the following figure. The selected glaciers cover the four outlet types as identified in Tedstone & Arnold (2012), namely proglacial river (Søndre Strømfjord) and outwash plain (Sermeq) for land-terminating glaciers, and calving (bay) (Chamberlin Gletsjer) and calving (fjord) (Kangerlussuup Sermia) for marine-terminating glaciers. In the meantime, these glaciers are picked so that they broadly cover the entire length of the west Greenland coast from North to South. The locations of these glaciers as listed in Table 1. Landsat scenes of the Outlet 1 region usually cover the three glaciers into the same bay, and therefore its catchment area includes those of the three glcier outlets. Søndre Strømfjord is also the study area of the Chu et al. (2009) study. Glacier names are derived from A. Bjørk et al. (2015).

Figure 7 (the following page). Sample scenes of the selected outlets and respective catchment areas (in blue) and their positions within the Greenland Ice Sheet.

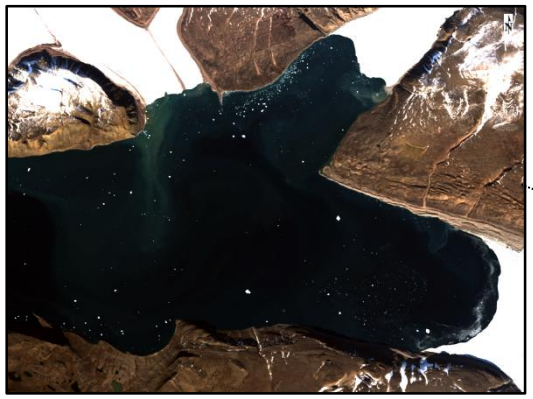

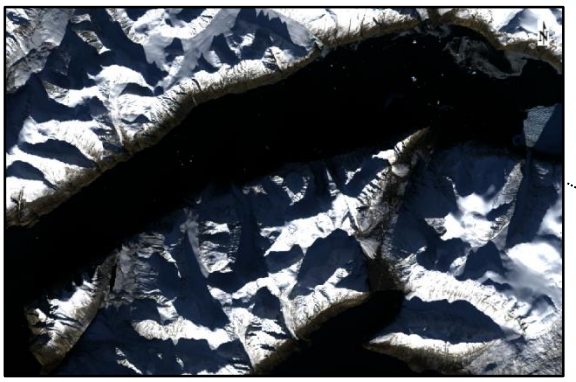

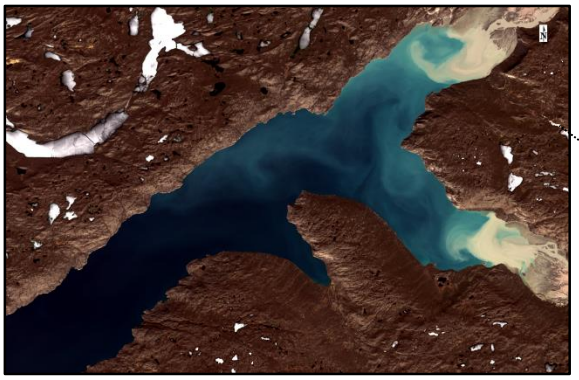

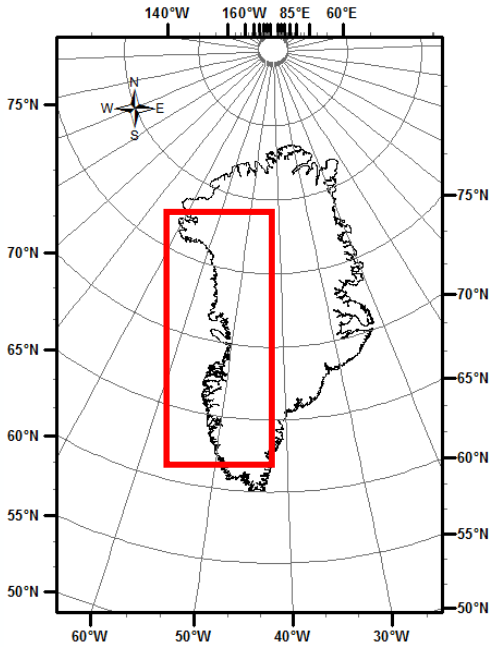
140°W
160°W
85°E
60°E
N
W
E
S
75°N
70°N
65°N
60°N
55°N
50°N
60°W
50°W
40°W
30°W

Table 1 Names, types and locations of the selected glacier outlets

Name	Code	Glacier type	latitude	longitude
Chamberlin Gletsjer	Outlet 1	Calving (bay)	76.719	-68.4795
Kangerlussuup Sermia	Outlet 2	Calving (fjord)	71.4614	- 51.6853
Søndre Strømfjord	Outlet 3	Proglacial river	66.9061	-51.3462
Sermeq	Outlet 4	Outwash plain	63.5242	-50.8639

3.2. Freshwater plume quantification

For this study, Landsat 7 Enhanced Thematic Mapper Plus (ETM+) (2000 -2012) to and Landsat 8 Operational Land Imager (OLI) and Thermal Infrared Sensor (TIRS) (2013-2014) imagery is used for the delineation of freshwater plumes in glacier outlets.

3.2.1. Landsat imagery acquisition and pre-processing

Landsat scenes covering the selected glacier outlets are manually picked using the USGS EarthExplorer tool (http://earthexplorer.usgs.gov/) in melt seasons (1 May to 30 September) from 2000 to 2014. Landsat 7 ETM+ scenes used in this study span from 2000 to 2012 which comes with a spatial resolution of 30m for visible and near and short-wave infrared (NIR and SWIR) bands, 15m for the panchromatic band, and 60m for the thermal band (products after 25 February resampled to 30m pixels); Landsat 8 OLI scenes are collected for 2013 and 2014 which are in the same sptial resolution as ETM+ scenes in the visible, NIR and SWIR bands, and in 30m resampled resolution (from 100m) for two thermal bands. Also, a new band 1 (ultra-blue) is added for coastal and aerosol studies, and a new band 9 is added for cirrus cloud

detection. Detailed band specifications of Landsat 7 and 8 bands are listed below (Department of the Interior & U.S. Geological Survey 2012):

*Table 2 Landsat OLI band specifications and Landsat 7 bands in corresponding wavelengths. * TIRS bands acquired at 100 meter resolution and resampled to 30 meter in delivered data product.** ETM+ Band 6 acquired at 60-meter resolution and resampled to 30m; products processed after February 25, 2010 are resampled to 30-meter pixel.*

Landsat 7 ETM+				Landsat 8 OLI & TIRS		
Landsat 7 Bands	Wavelength (micrometers)	Resolution (meters)	Band Type	Landsat 8 Bands	Wavelength (micrometers)	Resolution (meters)
			Ultra-blue	Band 1	0.43 - 0.45	30
Band 1	0.45-0.52	30	Blue	Band 2	0.45 - 0.51	30
Band 2	0.52-0.60	30	Green	Band 3	0.53 - 0.59	30
Band 3	0.63-0.69	30	Red	Band 4	0.64 - 0.67	30
Band 4	0.77-0.90	30	NIR	Band 5	0.85 - 0.88	30
Band 5	1.55-1.75	30	SWIR	Band6	1.57 - 1.65	30
Band 7	2.09-2.35	30	SWIR	Band 7	2.11 - 2.29	30
Band 8	0.52-0.90	15	Panchromatic	Band 8	0.50 - 0.68	15
			SWIR	Band 9	1.36 - 1.38	30
Band 6	10.40-12.50	60* (30)	Thermal Infrared	Band 10	10.60 - 11.19	100 ** (30)
			Thermal Infrared	Band 11	11.50 - 12.51	100 ** (30)

The number of acquired Landsat scenes (Landsat 7 and Landsat 8) for each outlet are: 45 scenes for Outlet 1, 98 scenes for Outlet 2, 81 scenes for Outlet 3, and 115 scenes for Outlet 4. Due to the large number of acquired Landsat scenes, atmospheric correction is conducted using the QUick Atmospheric Correction (QUAC) module in the ENVI 5.1 software package, and the process is automated through the use of the Interactive Data Language (IDL), version 8.3. QUAC determines atmospheric correction parameters directly from the pixel spectra in each scene and hence processing is much faster compared to physics-based first-principle methods

such as Fast Line-of-sight Atmospheric Analysis of Hypercubes (FLAASH), while producing reasonably accurate reflectance spectra within +/- 15% other methods (Bernstein et al. 2005).

Landsat 7 scenes since 30 May 2003 have wedge-shaped gaps due to the failure of the ETM+ Scan Line Corrector (SLC), resulting in an estimated 22% area loss in each scene. Various geostatistical methods have been devised to fill the data gaps for scientific analysis (e.g. USGS 2004; Maxwell et al. 2007; Roy et al. 2008), but most are computationally intensive and therefore have limited application in mass production of gap-filled scenes. In this study, gaps in Landsat 7 ETM+ SCL-off scenes (2003-2012) are not filled. Further data quality check reveals that pixels immediately adjacent to the data gaps tend to be missing data (having NaN values) in several or all of the spetral bands, thus limiting their usability. An automated algorithm is developed to filter out these 'bad pixels' (having NaN reflectance value in any band) from the analysis, and an example scene segment in which these pixels are highlighted can be found in Figure 8.

ETM+ Bands	Band 1	Band 2	Band 3	Band 4	Band 5	Band 7
Point A	NaN	NaN	0.1963	NaN	0.0149	0.0095
Point B	NaN	0.1705	0.2043	NaN	NaN	NaN
Point C	NaN	NaN	0.1246	NaN	NaN	NaN

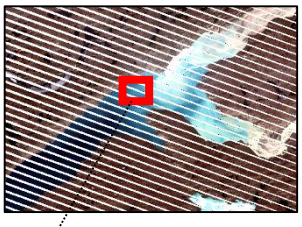

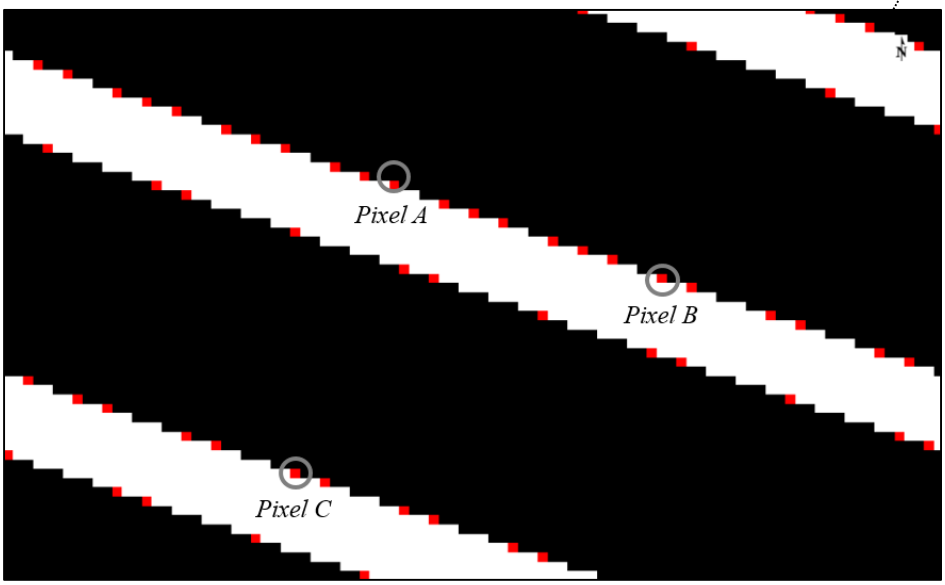

Figure 8 Sample image segment of Outlet 3 (19/6/2011) showing the derived data filter. Black: usable image; white: image gaps; red: pixels adjacent to image gaps that have been identified as 'bad pixels' (with one or more spectral bands having NaN values) and marked to be filtered out. The top table shows reflectance values in ETM+ visible bands for three randomly selected bad pixels (Pixels A, B and C).

3.2.2. Open water mask delineation

Due to the limited number of available Landsat imagery, scenes in which cloud cover does not cover the entire outlet region is included in the analysis (although a cloud cover maximum of 40% is applied in the data acquisition process). Therefore, some scenes suffer from cloud contamination on the outlet surface. Also, land surface and sea ice and icebergs floating on the outlet surface need to be excluded from the analysis. For each scene, a three-step process is applied in order to mask out land surface, ice (including land-fast ice, calving icebergs and sea ice), cloud cover as well as water bodies on land based on their respective spectral behaviors in Landsat's available bands, which is described as follows.

McFeeters (1996) proposed the normalized difference water index (NDWI) to separate water bodies from land surface, as shown in the following equation where Green is the reflectance value of a given pixel in a band encompassing green light and NIR represents that in a near-infrared band. The index is developed based on the fact that water bodies have relatively high reflectance of green lights and very low reflectance of NIR, while soil and vegetation features have high reflectance in the NIR band.

$$\text{NDWI} = \frac{Green - NIR}{Green + NIR}$$

Xu (2006) modified this index by substituting the NIR band with a middle infrared band. The new index, the modified NDWI (MNDWI), is shown to be able to achieve better water extraction result and can reveal more details of the open water surface (Ji et al. 2009; Li 2013; Du et al. 2014):

$$\text{MNDWI} = \frac{Green - MIR}{Green + MIR}$$

MNDWI is therefore used in this study to exclude land surface. Green corresponds to OLI band 3 (0.53-0.59 μm) or ETM+ band 2 (0.52-0.60 μm), and MIR corresponds to OLI band 6 (1.57-1.65 μm) or ETM+ band 5 (1.55-1.75 μm). A threshold of 0 can be used to distinguish between water featuress (positive MNDWI values) and soil/terrestrial vegetaion features (negeative MNDWI values). However, it has been found that cloud cover also tend to have positive values of MNDWI, and therefore the threshold of MNDWI is altered to 0.6 to eliminate clouds according to the following diagram of the different MNDWI and NIR reflectance values of water, snow and cloud cover. Note that the MNDWI is refered to as normalized difference snow index (NDSI) in many other applications (such as in this diagram) since it can also be used to delineate snow cover (Hall et al. 1995; Choi & Bindschadler 2004).

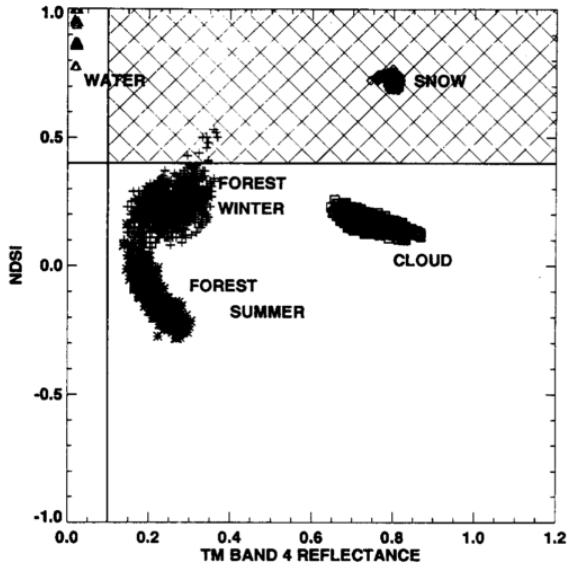

Figure 9 Different NDSI (MNDWI) and NIR band reflectance values of different land cover types. (From Hall et al., 1995).

The last land cover type left to be excluded is snow and ice. The above figure suggests that an additional criterion of NIR band reflectance < 0.11 (also suggested by Hall et al. (1995)) can achieve this task, but in our study the water body usually carry a considerable amount of sediment and these turbid waters can have NIR values larger than 0.11; on the other hand, wet

sea ice can have NIR values approaching the 0.11 threshold, too. Therefore, it has been found that a constant threshold value which filters out sea ice while keeping turbid water surface is difficult to derive. In this study, ice and water surface is separated by appplying a threshold of 0 on a band math of NIR – 0.5*Red (reflectance value in the NIR band minus half the reflactance value in the red band), as suggested by the Chu et al. (2012) study, which has shown superior performance than using NIR band thresholds. Pixels with positive values are identified as ice and excluded from the analysis. These processing steps yield water bodies in each scene, and finally, a manual mask is delineated for each outlet to define the approximate location of the outlet region in order to exclude water bodies on the land surface.

The end result of this filtering process is open water regions in the outlets with cloud and sea ice cover removed. The following figure shows comparisons of examples of original images versus derived open water filters (in dark blue) in each selected outlet:

a)

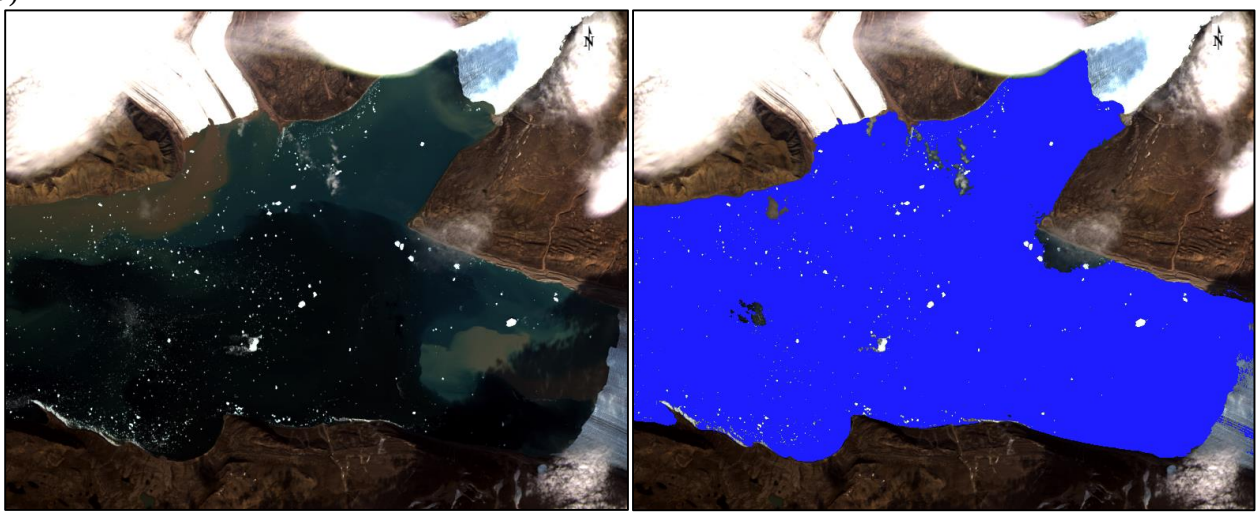

b)

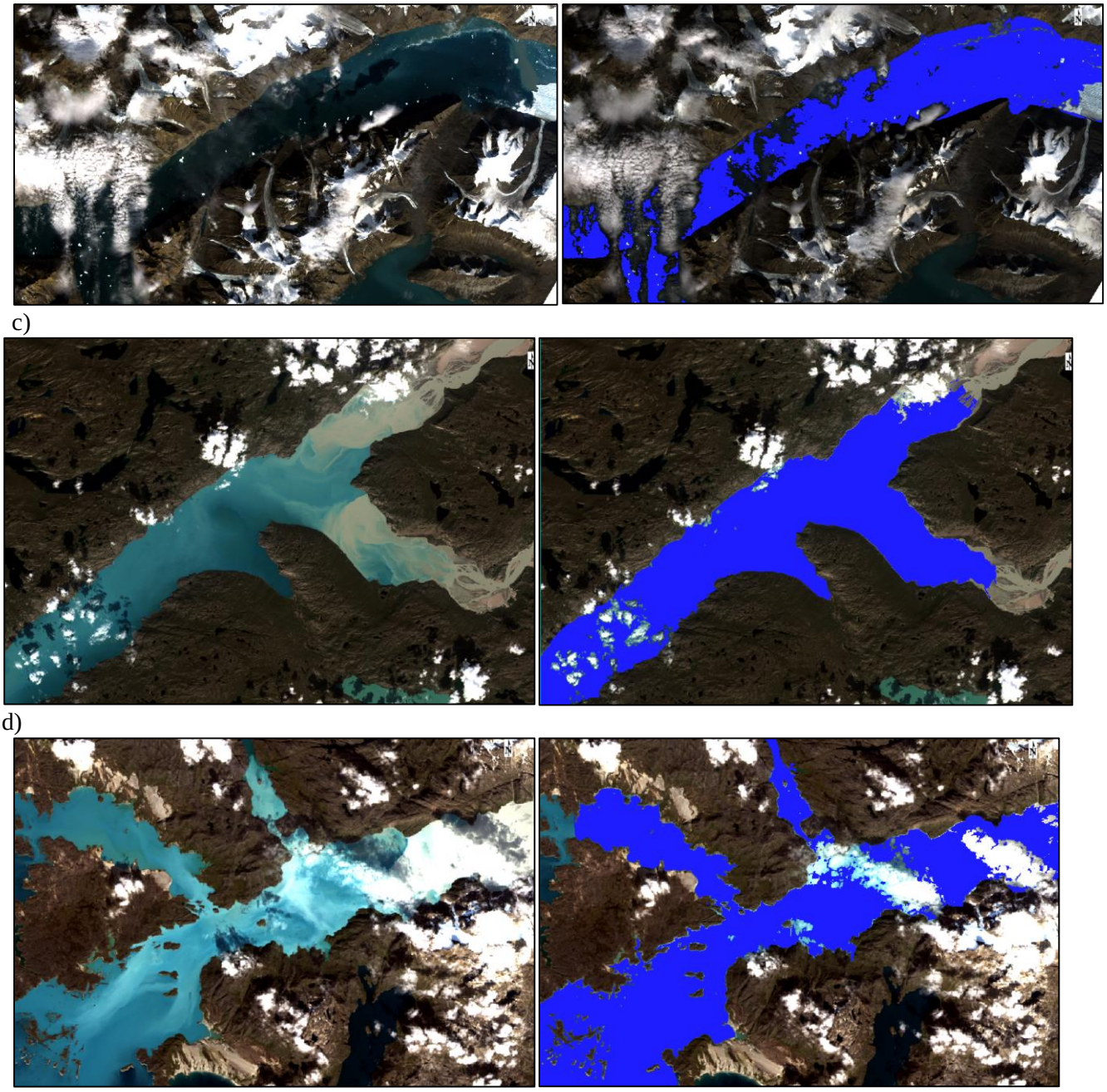

Figure 10 Examples of derived open water mask. Left: original image segment; right: open water mask (in dark blue) a): Outlet 1, 7/8/2014; b): Outlet 2, 23/7/2014; c): Outlet 3, 19/7/2014; d): Outlet 4, 15/8/2014.

3.2.3. Freshwater plume delineation

This study uses the quasi-analytical algorithm Carder-2 (Lee et al. 2002), which utilizes information from four specral bands, to calculate a_{CDOM} levels within each outlet. It is developed with large datasets expanding broad environmental conditions, and has been tested to consistently outprerform other algorithms. Although the Carder-2 algorithm has been found to overestimate a_{CDOM} levels in low CDOM environments, such as our study site, it have minimal impact on the results since this study only uses the differences in CDOM levels between freshwater runoff and ocean water to delineate plume features. $a_{CDOM}(443)$ has been widely recognized as the proxy of CDOM content (Zhu et al. 2014).

$$a_{CDOM}(443) = 10^{0.043-0.185p_{13}-1.081p_{23}+1.234p_{43}}$$

$$where\ p_{13} = \frac{R_{rs}(443)}{R_{rs}(551)}, p_{23} = \frac{R_{rs}(488)}{R_{rs}(551)}, p_{43} = \frac{R_{rs}(667)}{R_{rs}(551)}$$

$R_{rs}(\lambda)$ is the ground reflectance value of a spectral band centered at wavelengh λ.

Although this algorithm has been developed for use with MODIS spectral bands, Landsat band with similar central wavelength can be used for calculation, and Zhu et al. (2014) have proved that the change of bandwidth has no significant imapct on CDOM estimation accuracy.

Instead of using single thresholds on the Red band to delineate sediment plume, this study seeks to develop an adaptive plume delineation approach. More Specifically, this study experiments with three types of plume derivation algorithms : thresholding based on the collective information of a_{CDOM} levels across the entire study period in an outlet, unsupervised classification of individual a_{CDOM} images, and unsupervised classification on the original reflectance image.

3.2.3.1. Thresholding based on collective histogram

This approach uses information from all calculated a_{CDOM} scenes in the study period to construct a classification scheme from which the water body is separated into 3 categories: freshwater plume, peripheral plume and ocean water. This is achieved by stacking a_{CDOM} level histograms from all scenes into one collective histogram, and then determining optimal cut points which separates the water bodies 'naturally' for each outlet through Jenks natural breaks optimization (Jenks 1967). Then, plume area can simply be calculated by counting the resulting pixels in every classified water body category. This method keeps the objectiveness in thresholding the a_{CDOM} levels, and also the derived plume features are comparable across the time series, i.e. plumes identified in different scene are bounded by the same a_{CDOM} levels. The table below lists the derived acdom level thresholds.

Table 3 Derived cut points separating freshwater plume, peripheral plume and ocean water for the selective outlets.

	Threshold 1 (m^{-1})	Threshold 2 (m^{-1})
Outlet 1	0.086	0.25
Outlet 2	0.084	0.2
Outlet 3	0.078	0.5
Outlet 4	0.079	0.44

An example image for each outlet with identified freshwater plume and peripheral plume using this method is shown below.

a)

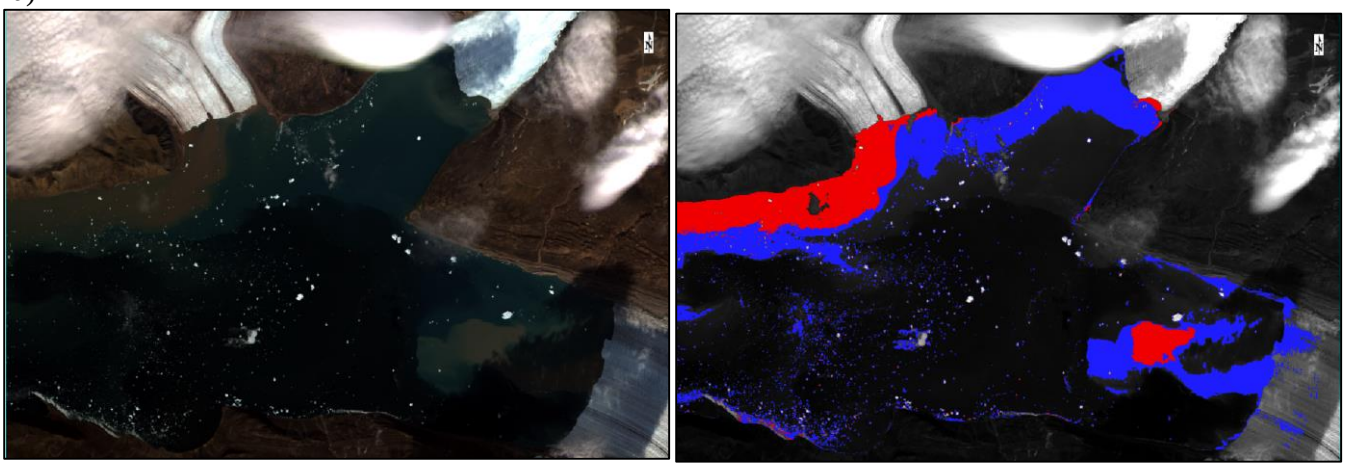

b)

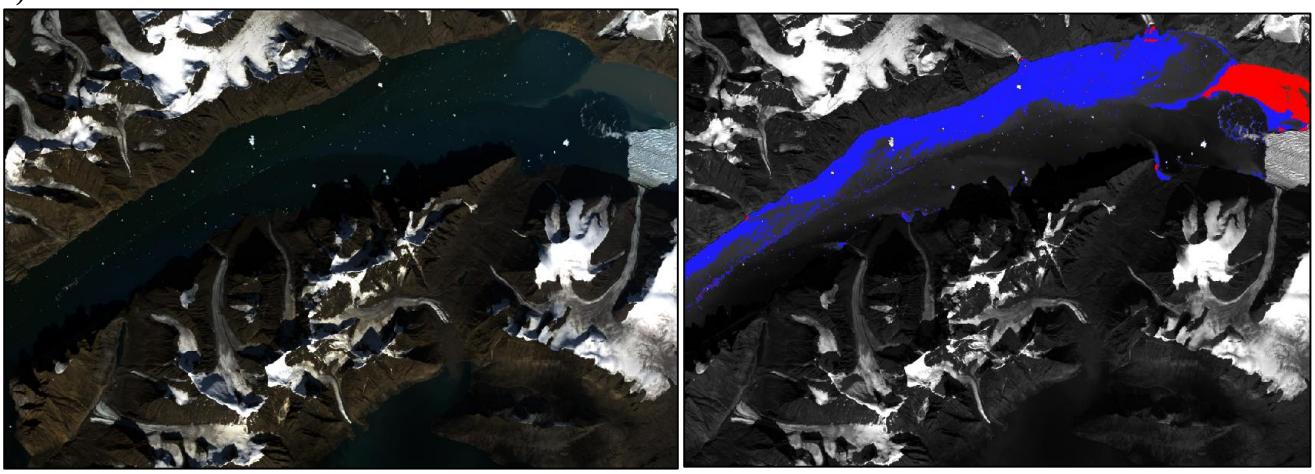

c)

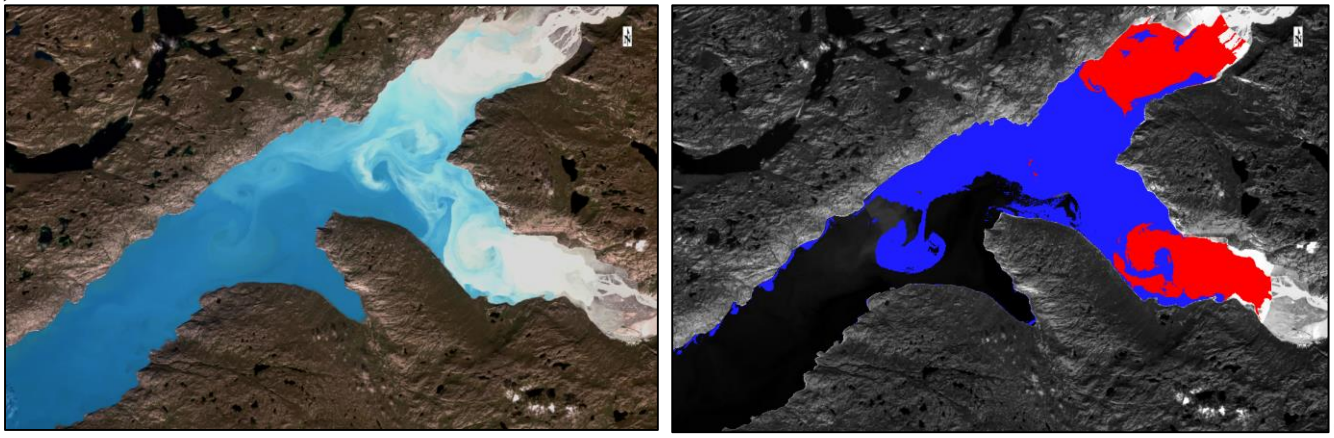

d)

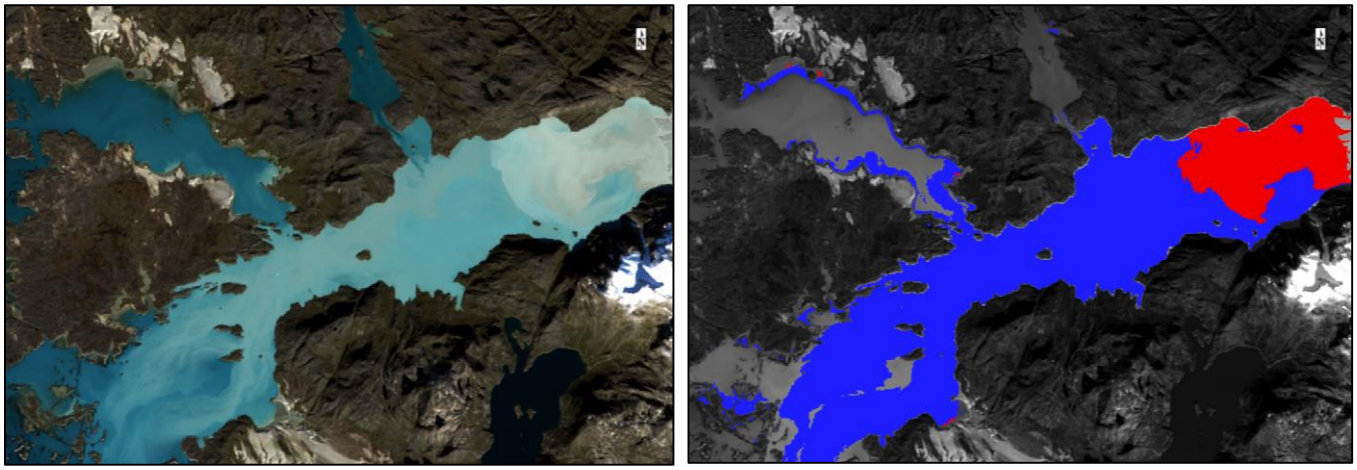

Figure 11 Example thresholding of acdom level for each of the selected outlet. Red: freshwater plume; blue: peripheral plume; transparent: ocean water. a) Outlet 1, 7/8/2014; b) Outlet 2, 2/8/2014; c) Outlet 3, 6/8/2014; d) Outlet 4, 9/9/2014.

3.2.3.2. Classification on individual a_{CDOM} scenes

Another approach of delineating freshwater plume is to apply image classification algorithms on individual a_{CDOM} scenes. Due to the large number of scenes to process, the unsupervised K-means classification method is used for this purpose, which is available in the ENVI 5.1. package. It is worth noting that since the classification algorithm is applied onto a 1-band image, it is essentially a 1-deminsion clustering process equivalent to the Jenks natural breaks optimization, this time for each individual a_{CDOM} scene.

The merit of this classification scheme lies in its objectivity in plume delineation which avoids arbitrary definition of index thresholds. More importantly, as discussed earlier, the amount of sediment and also CDOM carried into glacier outlets depends not only on freshwater output, but also on the availability of sediment and CDOM. Thus, in later melt season when their supply is exhausted, sediment or CDOM levels may be less than the threshold as determined from a collective histogram of all scenes, making the detection of freshwater output at these times much less effective. Classification of individual a_{CDOM}

image, however, takes into consideration the CDOM level in each image, and is able to avoid this issue.

This study classifies the open water area in each selected outlet into four categories using K-means classification (number of iterations: 50; change threshold: 5%), since experiments show that a three-class classification yields less satisfactory plume delineation results, and the use of more classes may result in excessive fragmentation of the classified image. An example of classified a_{CDOM} image for each outlet is shown in the following figure. Class 4 is determined to be the category 'freshwater plume', and class 2 and 3 combined forms the 'pheripheral plume' category. The rest of the open water surface falls into the 'ocean water' category. Note that for Outlet 3 (Figure 12 (c)), freshwater emenates from the outlet to the lower right coner of the image and the core plume appear within the open water surface and is not attached to the ice margin. The freshwater upwelling is likely indicative of freshwater coming from a sub-glacial conduit which then emerge to the water surface.

a)

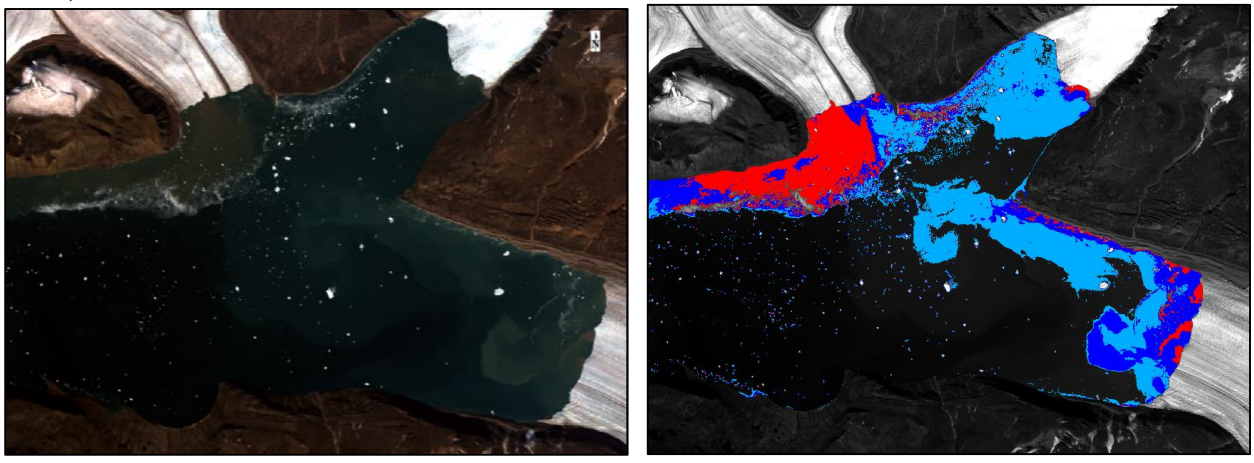

b)

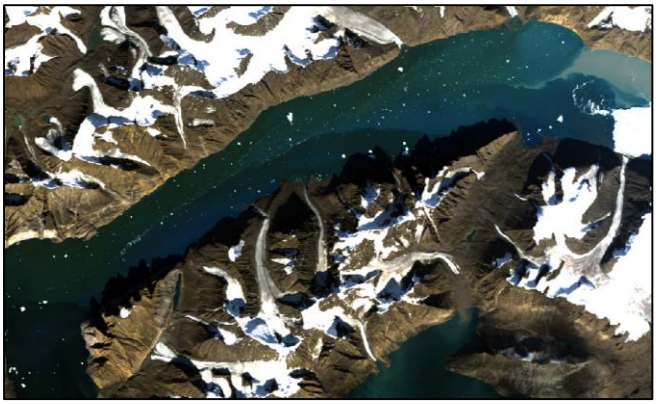

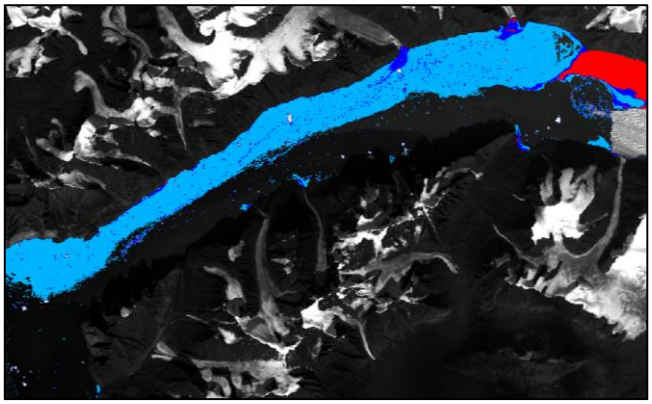

c)

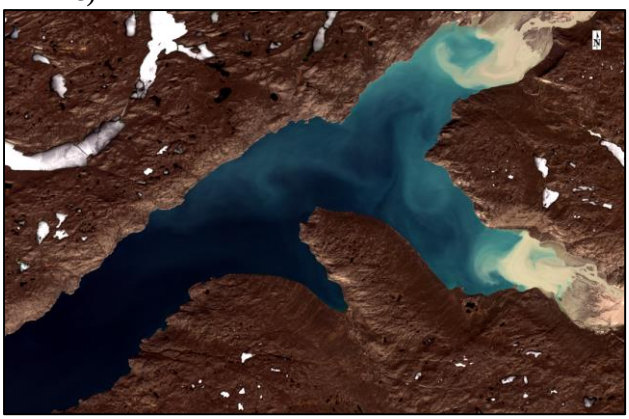

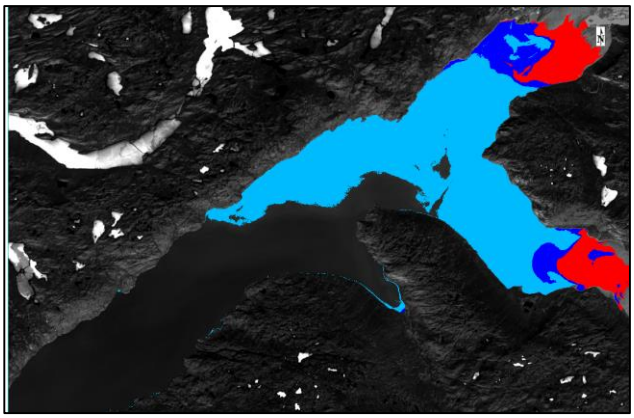

d)

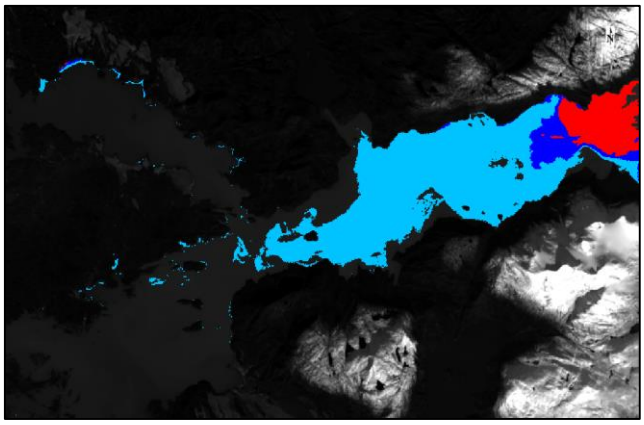

Figure 12 Example classifications of acdom images for each of the selected outlet. Red: freshwater plume; light blue and dark blue: peripheral plume; transparent: ocean water. a) Outlet 1, 12/8/2014; b) Outlet 2, 2/8/2014; c) Outlet 3, 10/6/2014; d) Outlet 4, 16/9/2014.

3.2.3.3. Classification on original reflectance images

This method applies k-means unsupervised classification on the original ground reflectance image cropped by the open water mask. The same number of classes (four) are chosen to be the same as classification on individual a_{CDOM} image. Similarly, Class 4 is determined to be the category 'freshwater plume', class 2 and 3 combined forms the 'pheripheral plume' category.

Due to the image gaps in Landsat 7 ETM+ scenes, plume areas derived for each scene from these two methods are divided by the total surface area of open water, resulting in the proportion of freshwater plume in the open water area.

3.3. Daily melt extent extraction

Brightness temperature data from the Special Sensor Microwave Imager (SSMI) and Special Sensor Microwave Imager/Sounder (SSMIS) is used for the derivation of melting areas in the catchment area for each outlet for comparison with the derived plume record.

3.3.1. Brightness temperature and Greenland hyrological datasets

Melt information can be retrieved from the Level-3 Equal-Area Scalable Earth-Grid (EASE-Grid) Brightness Temperature dataset generated from the Special Sensor Microwave/Imager (SSM/I) and the Special Sensor Microwave Imager/Sounder (SSMIS) provided by Defence Meteorological Satellite Program (DMSP) (Table 4). The dataset provides

brightness temperature data for the whole globe at 0.1K precision. The data comes in global cylindrical equal-area projection, and has a nominal spatial resolution of 25km for all channels and is available daily from July 1987 to present (Armstrong et al. 1994). Data are contained in flat binary files and are downloaded via the National Snow and Ice Data Centre (NSIDC) FTP server.

As the study period is from 2000 to 2014, only data from SSMI F13 and SSMIS F17 platforms are used for the analysis. There is an overlap in F13 and F17 data from 14 December 2006 through 29 April 2009. Where possible, F17 data is used. The new source data version provides cross-calibration between all SSM/I and SSMIS sensors, thus ensuring inter-consistency of brightness temperatures derived from the sensors.

Table 4 Different satellite sensors contributing to the Brightness Temperature dataset and their time periods.

Satellite sensor	**Temporal Coverage**
DMSP SSMI F8	9 July 1987 – 18 December 1991
DMSP SSMI F11	3 December 1991 – 12 January 1998
DMSP SSMI F13	3 May 1995 – 31 December, 2007
DMSP SSMIS F17	14 December 2006 – most current processing date

Catchment areas of the selected outlets is derived from the Lewis & Smith (2009) Greenland hydrologic catchments dataset (Figure 7). The hydrological drainage network is derived for the whole of Greenland Ice Sheet from bedrock digital elevation models (DEMs) and surface topography. The data comes in shapefiles and is processed using the ArcMap 10.2 software package from which catchment areas for each of the four selected outlets are extracted and exported for use in further anlaysis.

3.3.2. Daily melt extent calculation

Melt extent is determined through the commonly used XPGR (cross-polarized gradient ratio) technique proposed first by Abdalati and Steffen, 1995 (the following equation) which utilizes the vertical 37GHz ($T_b(37V)$) and horizontal 19GHz ($T_b19H)$) channels of the SSM/I-SSMIS sensors to detect the depolarization effect of melting snow (Abdalati & Steffen 1995). Also according to the works of Abdalati and Steffen, a threshold of -0.0158 is used in detecting melt so that all values below this threshold represent dry snow and those above it represent wet snow (melting pixels).

$$XPGR = \frac{T_b(19H) - T_b(37V)}{T_b(19H) + T_b(37V)}$$

After melt information has been derived from the brightness temperature record, melt area within the catchment area of each outlet is calcualted using the methology of Tedstone et al. (2012). Each corner coordinate of a melting pixel that fall into the catchment area contributes to a melt area equivalent to a quarter of the SSM-I/SSMIS grid size ($156.25km^2$). Total daily melt area of each catchment area is calculated which forms a melt extent time series over the melt seasons from 2000 to 2014 for comparison with derived plume area time series. The entire process of deriving melt information from brightness temperature dataset and then conducting statistical analysis of the relationship between melt extent and plume proportion time series is implemented using MATLAB. An overall flowchart of this study is shown as follows:

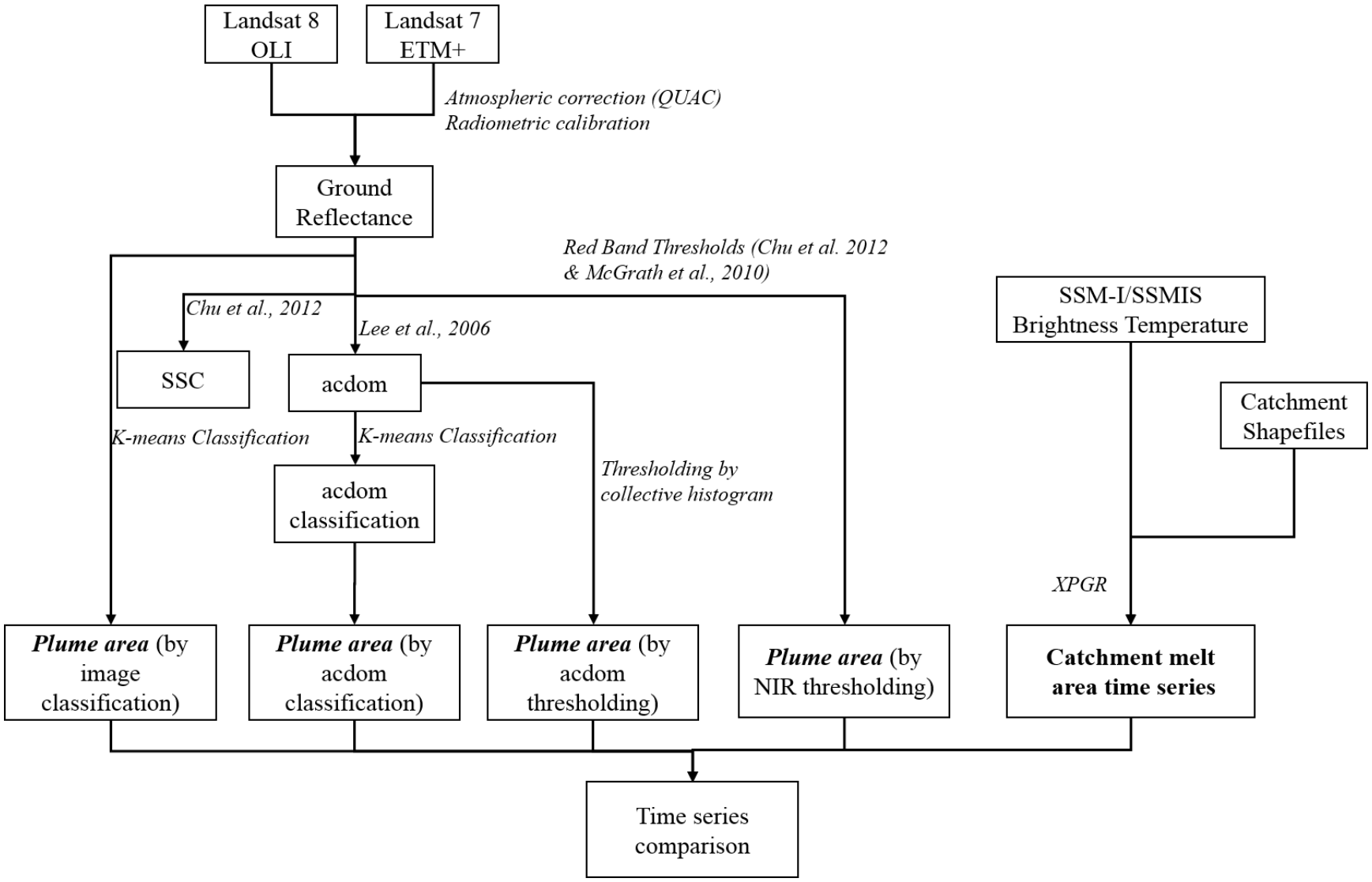

Figure 13 Data processing and analysis flowchart

4. RESULTS

4.1. Temporal variability in meltwater output and surface melt

4.1.1. Annual average melt extent and plume proportions

The figures below illustrate inter-annual variations in average melt extent and derived plume proportion in the melt season. Figure 14 shows annual averge plume proportions extracted using methods proposed in this study: a_{CDOM} thresholding, classification on individual a_{CDOM} scenes, and classification on the entire reflectance image; Figure 15 shows those derived from thresholding reflectance values in the Landsat Red band using thresholds proposed by Chu et al. (2012) (Red>0.12) and McGrath et al. (2010) (Red>0.10).

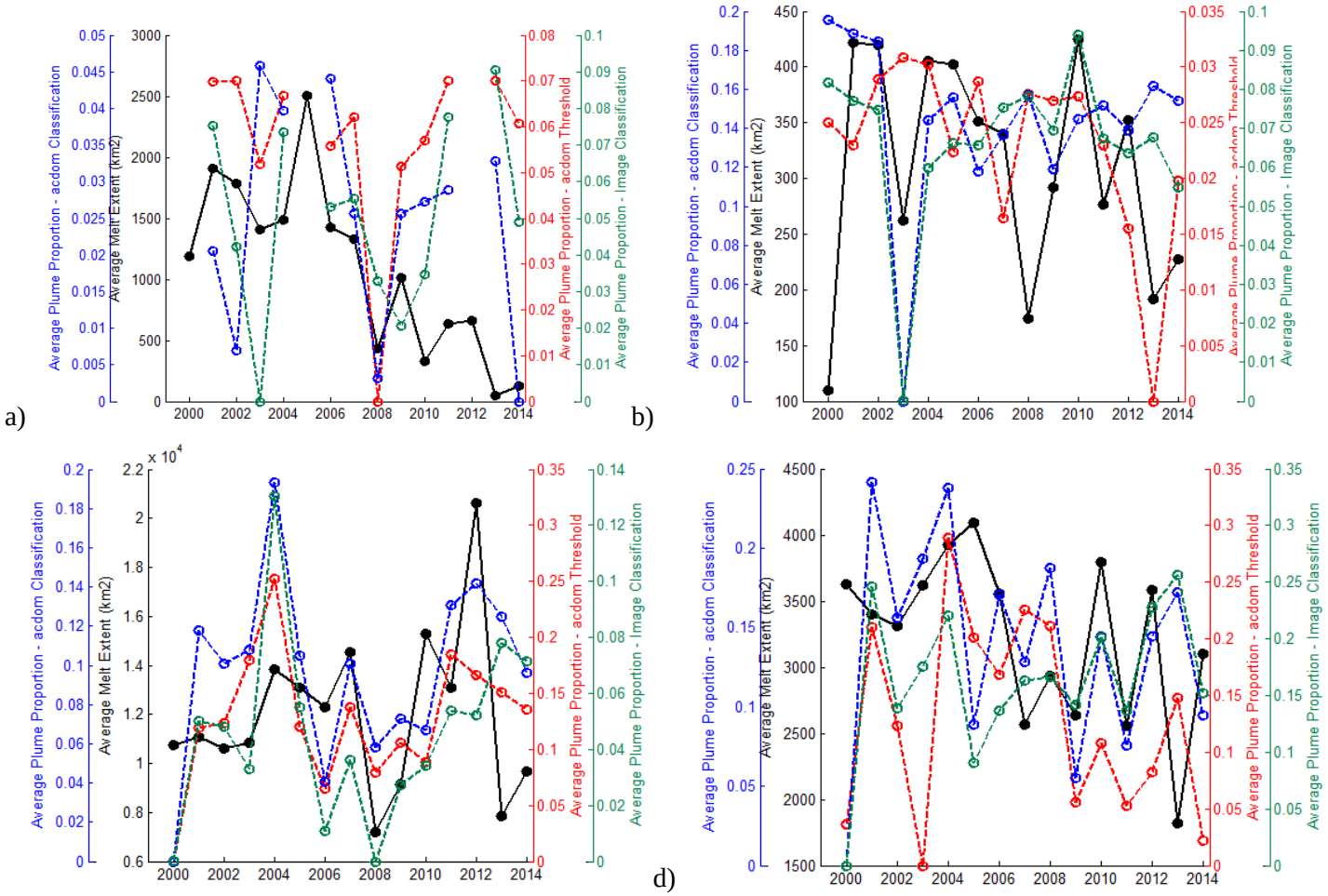

c)

Figure 14 Annual average melt extent (solid circle, black solid line) and plume proportions (hollow circle, dashed lines) derived from the proposed methods (red: from acdom threshold; blue: from acdom classification; green: from reflectance image classification). (a): Outlet 1;.(b):Outlet 2; (c):Outlet 3;(d): Outlet 4.

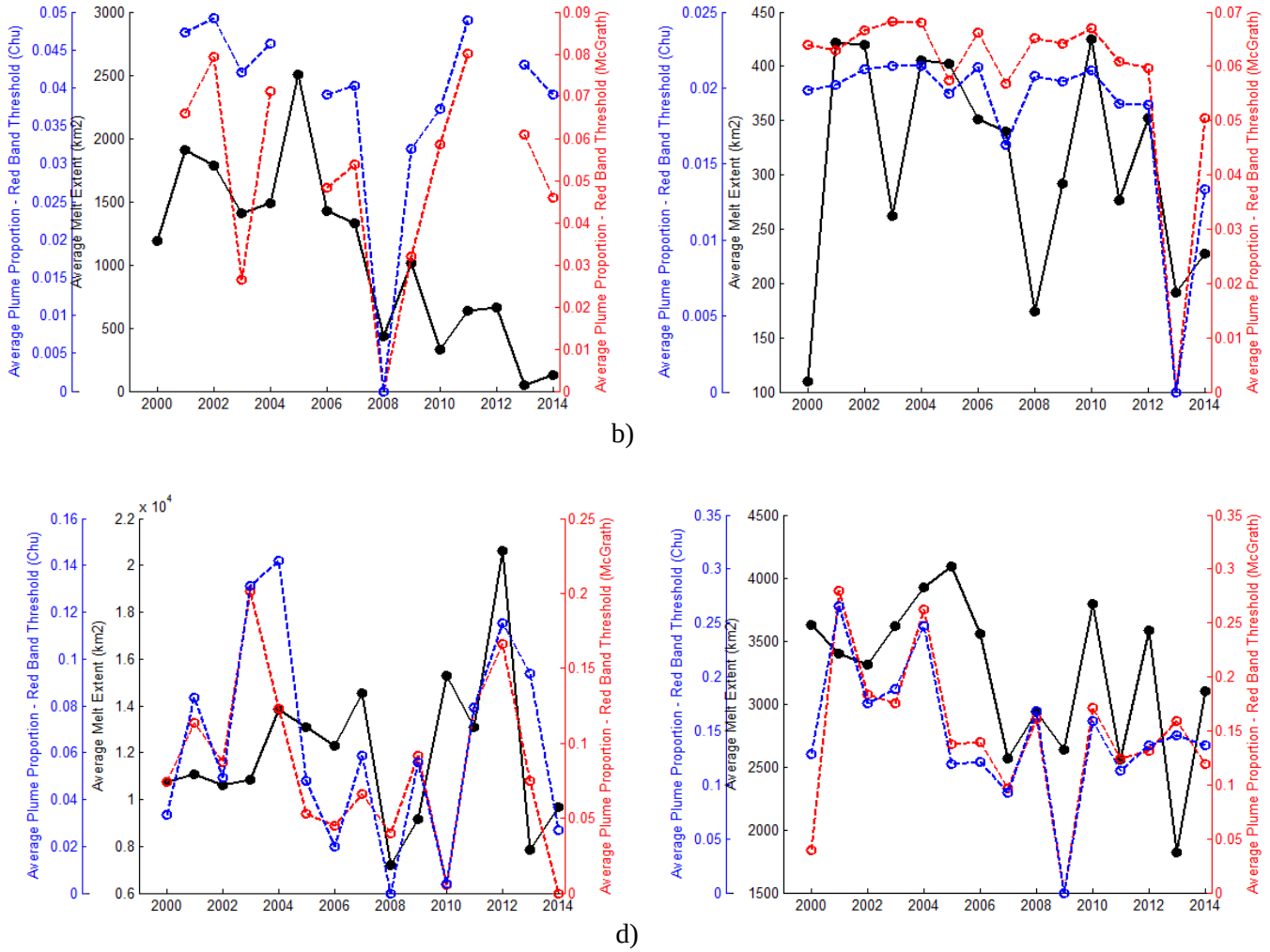

Figure 15 Annual average melt extent (solid circle, black solid line) and plume proportions (hollow circle, dashed lines) derived from Red band thresholding methods (red: from McGrath's Red band threshold: >0.12; blue: from Chu's Red band threshold:>0.10). (a): Outlet 1;.(b):Outlet 2; (c):Outlet 3;(d): Outlet 4.

For Outlet 1, there are apparent missing plume proportion data in the years of 2000, 2005 and 2012 (Figure 14 (a)). This is due to the fact that no usable Landsat scenes are available for these particular years. In 2003, the melt extent and both plume proportions derived from a_{CDOM} thresholding and reflectance image classification experience an increase from a local low point; the same occurred in 2008 for the melt extent and plume proportiosn derived from a_{CDOM} thresholding and a_{CDOM} classification. More importantly, an overall similar change pattern can be seen from the curves of melt extent and plume proportions: from the low point in 2003-2004 they increase towards 2005, and experience another low poing in 2008-2009, and increase again to a

peak around 2010-2012. This pattern can also be observed in a comparison between the melt extent and plume proportions derived from the two Red band thresholding methods (Figure 15 (a)). These two curves track each other closely in pattern, which is expected given they use the same single spectral band in delineating sediment plumes.

For Outlet 2, a same generall trend can be observed as in Outlet 2, which holds true for the melt extent and plume porportions derived from the two classification methods (Figure 14 (b)). However, plume proportions derived from acdom thresholding (red curve) seems to be lagging behind the rest of the curves by ~1-2 years, except its low point in 2013 coincide with the others. Moreover, it can be seen that the trend in plume proportions derived from the two Red band thresholding methods (Figure 15 (b)) resembles closely that of plume proportions derived from acdom thresholding, a pattern also apparent in Outlet 1. This suggests the similarity in thresholding technqiues in deriving freshwater plumes.

For Outlet 3, melt extent and plume proportions derived using methds proposed by this study track each other very closely (Figure 14 (c)), as can be seen from their common turning points in the years of 2001, 2004, 2006, 0007 and 2008, and a genearl pattern of reaching low points in 2002-2003, 2006, 2008 and peaking in 2004 and around 2010-2012 can be summarized from the trends in the four curves. Plume proportions derived from Red band thresholding also very closely follow the trend of the melt extent curve except in the year of 2010 when plume areas derived from both methods drop to a very low value while melt extent is at a local peak (Figure 15 (c)).

In Figure 14 (d), the trend in plume proportion curves for Outlet 4 only broadly trace that of melt extent, being at low points around 2002-2004, 2006-2007 and 2011, and peaking around 2004-2006, 2007-2008, 2010, and 2012-2013, althrough their turning points don't tend to coincide (except in the years of 2010 and 2012 when all four curves share the same trend). Plume proportions derived from Red band thresholding (Figure 15 (d)) also follows the melt extent curve loosely. Also similar to Figure 14 (d), these two curves follow the melt extent more closely after 2007, before which the trends of melt extent and plume proportions don't coincide well.

Table 5 Correlation between annual average melt extent and plume proportions time series

	Outlet 1		Outlet 2		Outlet 3		Outlet 4	
Plume Derivation Method	Correlation coefficient	p-value	Correlation coefficient	p-value	Correlation coefficient	p-value	Correlation coefficient	p-value
acdom Threshold	0.223	0.424	0.352	0.199	0.287	0.301	0.308	0.264
acdom Classification	0.361	0.186	0.393	0.146	0.340	0.215	0.393	0.147
Reflectance Image Classification	0.015	0.959	0.134	0.635	0.194	0.489	0.254	0.361
Red Threshold (McGrath)	0.248	0.374	0.267	0.337	0.290	0.294	0.118	0.648
Red Threshold (Chu)	0.324	0.239	0.016	0.954	0.300	0.278	-0.236	0.397

In an attempt to quantify the correlation between annual average melt extent and plume proportions in each outlet, correlation coefficients between these two time series and the corresponding p-values area calculated and recorded in Table 5. Due to Landsat data gaps in Outlet 1, the missing values in its plume proportion time series have been linearly interpolated using the two nearest values. Although none of these correlations are significant judging from the p-values, it can be seen that plume proportions derived from a_{CDOM} thresholding and a_{CDOM} classification have relatively higher correlations to melt extent, and plume proportions derived using a_{CDOM} classification have consistently higher correlation coefficients than others. This suggests that methods using the derived a_{CDOM} image generally trace the trend in melt extent more closely.

4.1.2. Melt extent and plume proportion time series comparison

Figures below show the comparison between time series of melt extent and plume proportion derived using different methods during the melt season in every year, followed by

scatterplots of plume proportions and melt extent in the days when plume proportions are calculated (when Landsat scenes are acquired) in each outlet. It should be noted that due to the limitation in available Landsat scenes, the starting and ending dates of plume appearance cannot be used as an indication of the duration of meltwater runoff, and also the analysis of short-term variations in plume proportion is not feasible.

4.1.2.1. Outlet 1

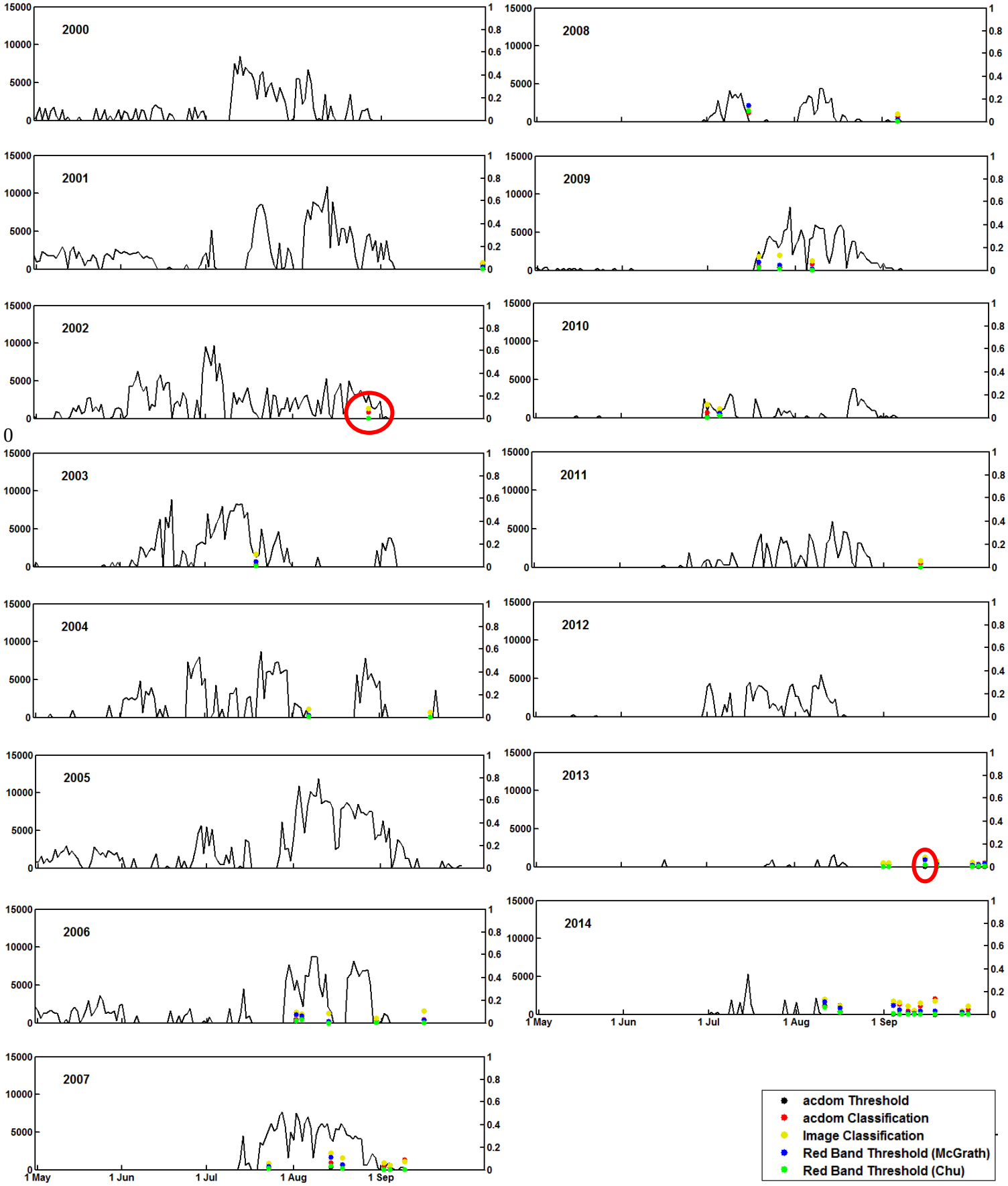

Figure 16 Outlet 1: plume areas derived from different methods (points) vs. daily melt extent in the catchment area during the melt season, 2000-2014

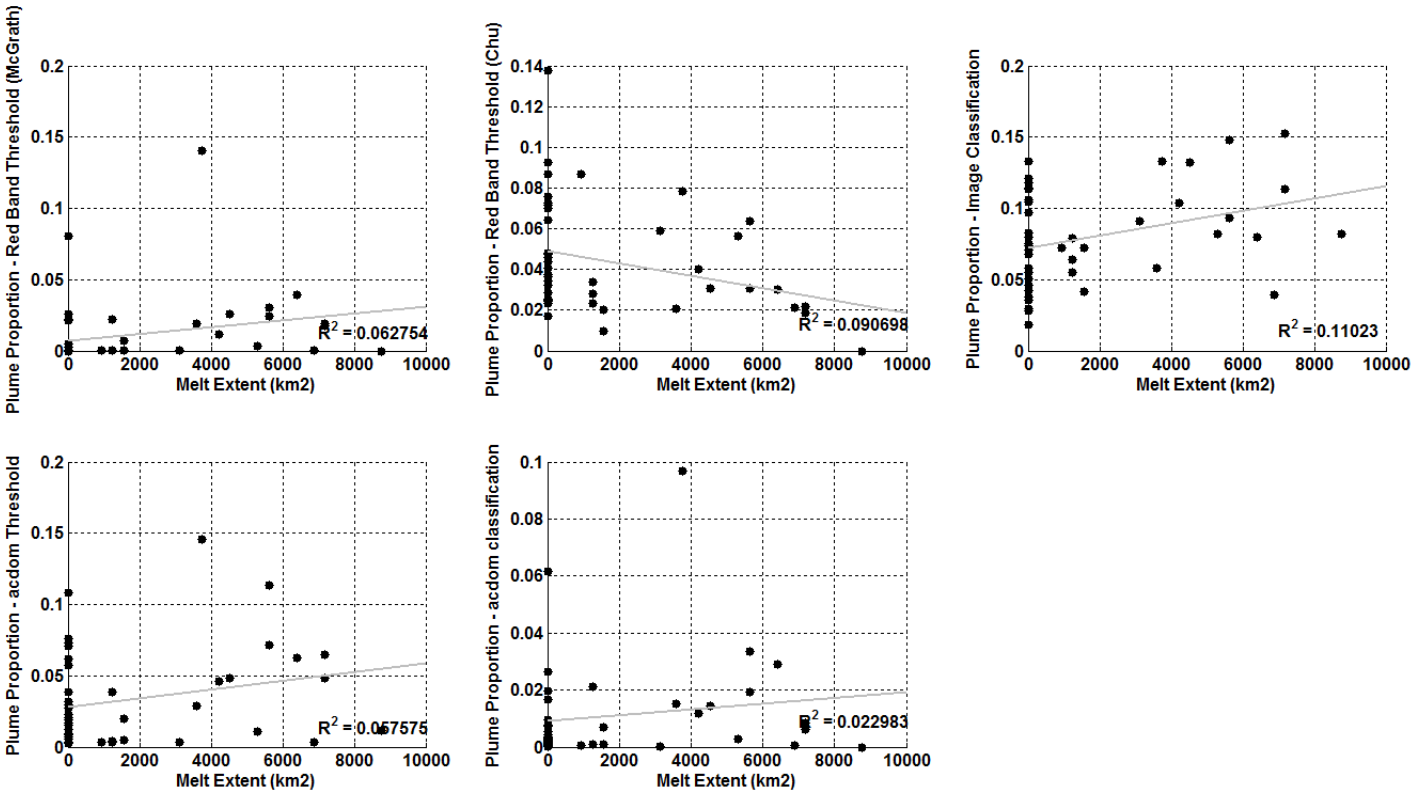

Figure 17 Outlet 1: scatter plots of melt extent (x axis) vs plume proportions derived by different methods (y axes).

The availability of usable scenes for Outlet 1 is particularly limited: only 45 scenes are acquired which contain enough open water area in the outlet region to allow the analysis to be undertaken. It can be seen from Figure 16 that generally, plume proportions derived by the two classification methods (red and yellow) are larger than those derived by thresholding techqniues (blue, green and black). A further check at the data shows that plume proportions derived by a_{CDOM} thresholds (black) has been consistenly covered those derived by Red band thresholding (green), both resulting in very low plume proportions. Due to limited data availability, data points of plume proportion are distributed sparsely along the time series. In the years of 2013 and 2014, relatively more plume proportion data are available. However in these years only minimal melt extents have been recorded. Thus, few patterns can be recognized regarding relationship the melt extent and plume proportion time series. Also from Figure 17, no apparent patterns can be observed between plume proportions and melt extents in the days when Landsat data is available. However, for all the graphs in Figure 17, a considerable number of data points reside on or near the y axis, suggesting that freshwater plumes are detected when melt extent in the catchment is

shown to be zero. as can be seen from later melt seasons in the years of 2006, 2007, 2013 and 2014 (Figure 16).

In order to check how the plume proportion derived from different methods compare to each other in more details, a further scatter plot is created as follows which shows a comparison between plume proportion derived from Red band thresholding and the three proposed methods. It can be seen that the plume proportions derived from a_{CDOM} thresholding (Figure 18 (a & d)) is comparable to that from Red band thresholding (slightly lower than plumes extracted from McGrath's threshold and slightly higher than that from Chu's threshold). However, in the plots showing the comparion between the two classification methods and the two Red band thresholding methods (Figure 18 (b, c, e & f)), clusters of points can be found near the y axis, again suggesting consistently larger plumes extracted by the classification methods than the thresholding methods.

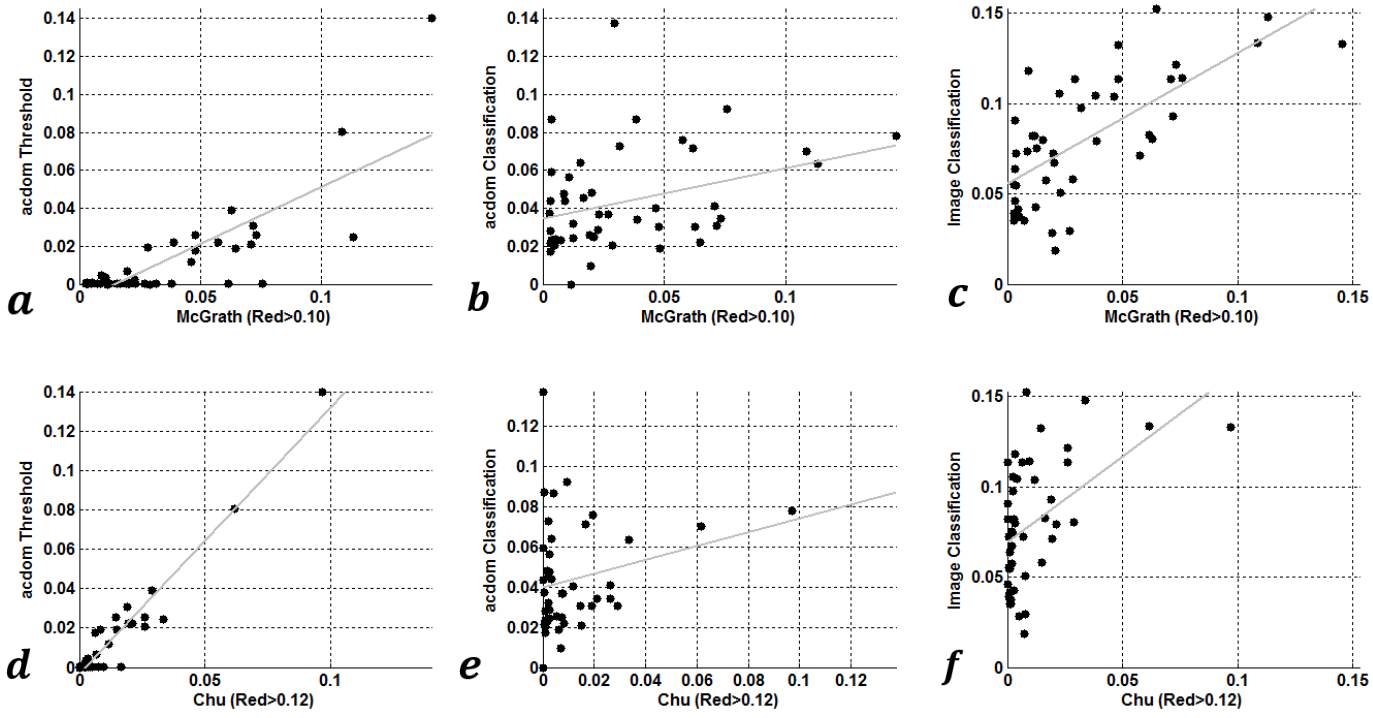

Figure 18 Outlet 1: Comparison between plume proportion derived from Red band thresholding (x axes) and methods proposed in this study (y axes).

In an attempt to check the reason causing this systematic different in derived plume proportions, scenes are checked individually, and below are two examples (also marked in Figure 16 by red circle). Figure 19 (a) shows the reflectance image in the day of 23/8/2002, and it can be seen that the image is partially obscured by cloud cover near the outlet location, which has been filtered out by the open water masking process. Figure 19 (b) shows the frequency distribution of reflectance values of its red band with McGrath's (solid red line) and Chu's (dashed red line) Red band thresholds overlaid. As both threshold are larger than all Red band reflectance values, no plume is extracted from Red band thresholding on this day. The same can be concluded about a_{CDOM} thresholding (Figure 19 (c)) and no plume is detected using this method either.

However, visual inspection of the original reflectance image reveals plume-like features emenating from the three outlets in the scene, and both classification on the original image and on the a_{CDOM} image managed to capture these features while other methods fail (Figure 16, data points within red circle). Note that as the cloud cover is relatively shallow, part of the cloud edge is included in the open water mask, resulting in it being classified as plume features. Nevertheless, the real plume features near the outlet have been succesfully recorded by the algorithm. This suggests the SSC level on this day is too low for the plume to be recorded by the universal thresholds of Red band reflectance, which are both established from field studies of Søndre Strømfjord (Outlet 3), a much more sediment-rich outlet than Outlet 1. Figure 20 shows a day with similar situation. These case studies, along with other dates in which classification methods report the existence of freshwater plumes while thresholding method do not, suggests that extracting plumes based on one single-band threshold is not reliable when applied to different locations, and that classification methods has the potential of registering freshwater output much more efficiently.

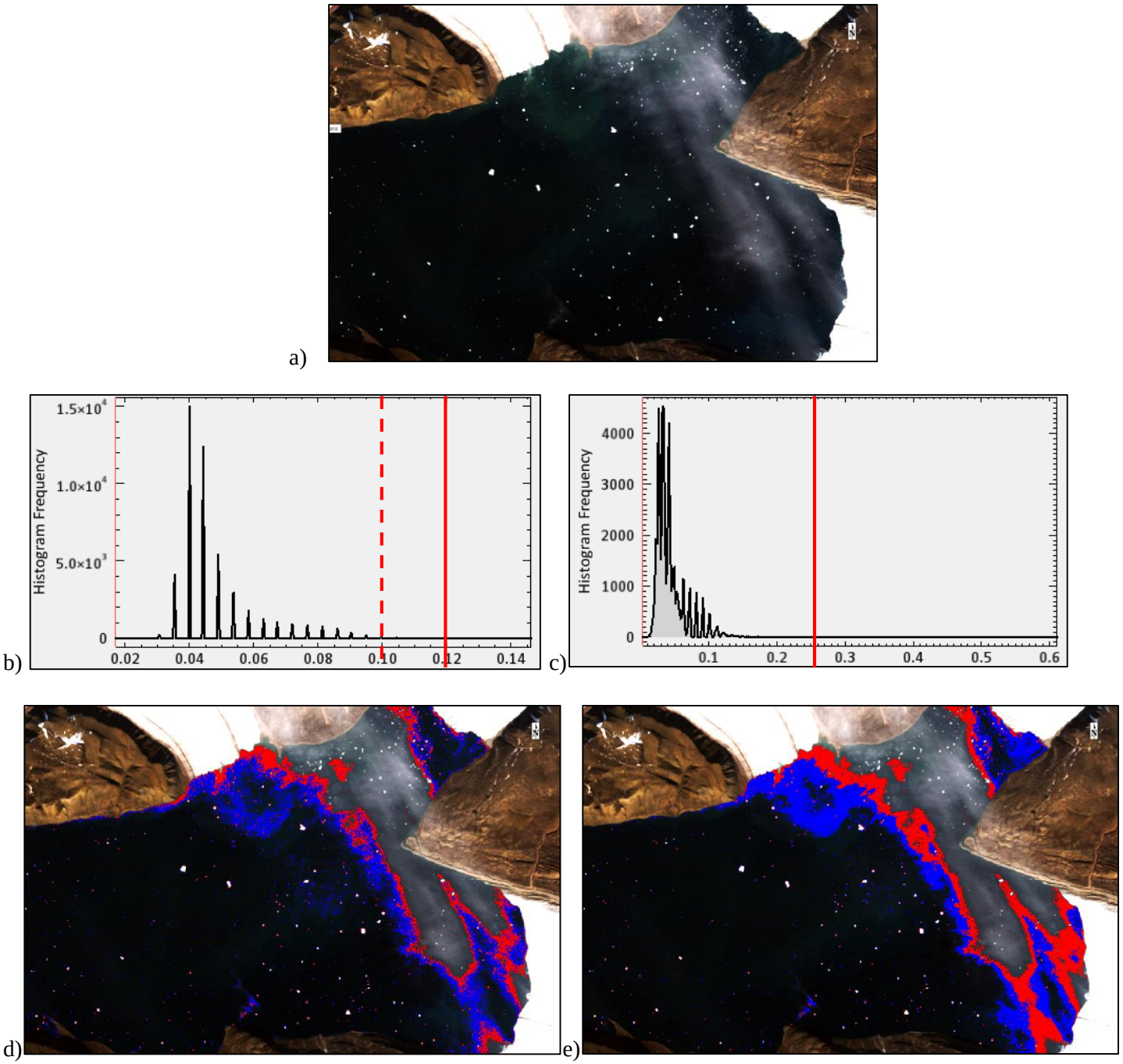

Figure 19 a) Original reflectance image: Outlet 1, 23/8/2002; b) Frequency distribution of reflectance values in Landsat Red band within the open water mask (dashed red line – Chu's Red band threshold: 0.12; solid red line – McGrath's Red band threshold: 0.10); c) Frequency distribution of acdom level within the open water mask (red line: acdom threshold: 0.25); d) Core plume (in red) and peripheral plume (in blue) extracted by classification of the acdom image; e) Core plume (in red) and peripheral plume (in blue) extracted by classification of the original image.

a)

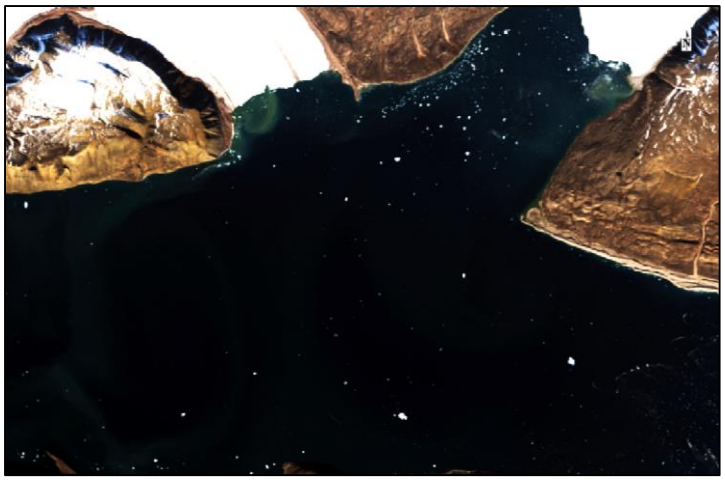

b)

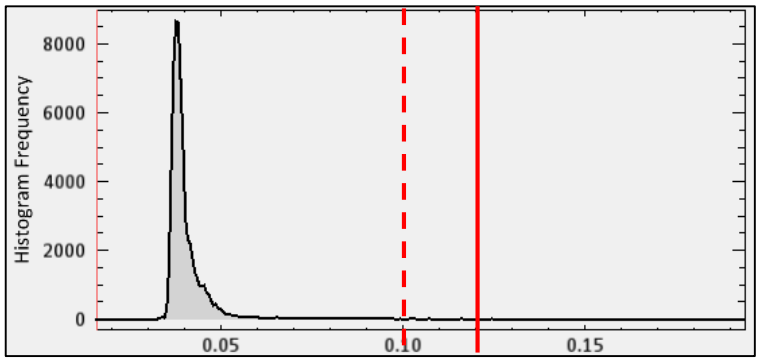

c)

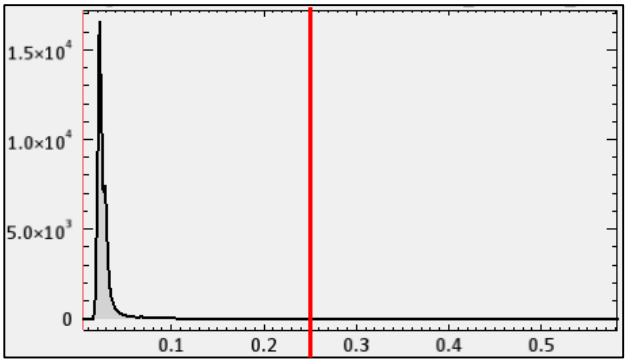

d)

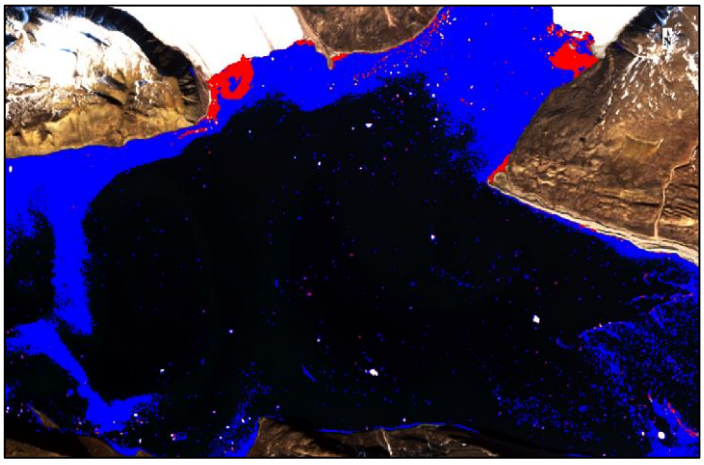

e)

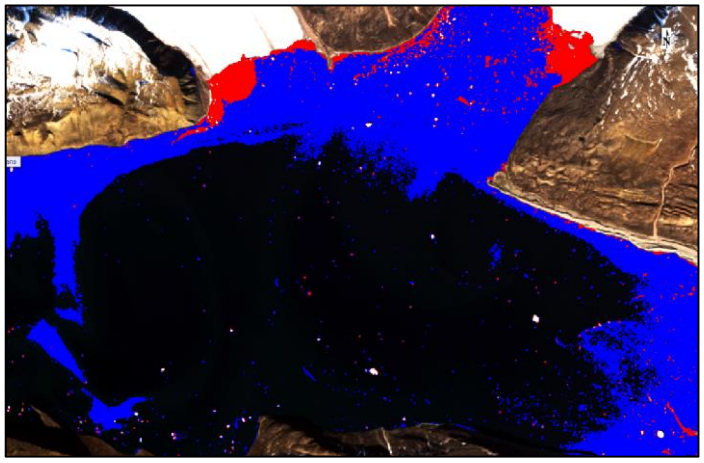

Figure 20 Outlet 1, 13/9/2013, as Figure 19

4.1.2.2. Outlet 2

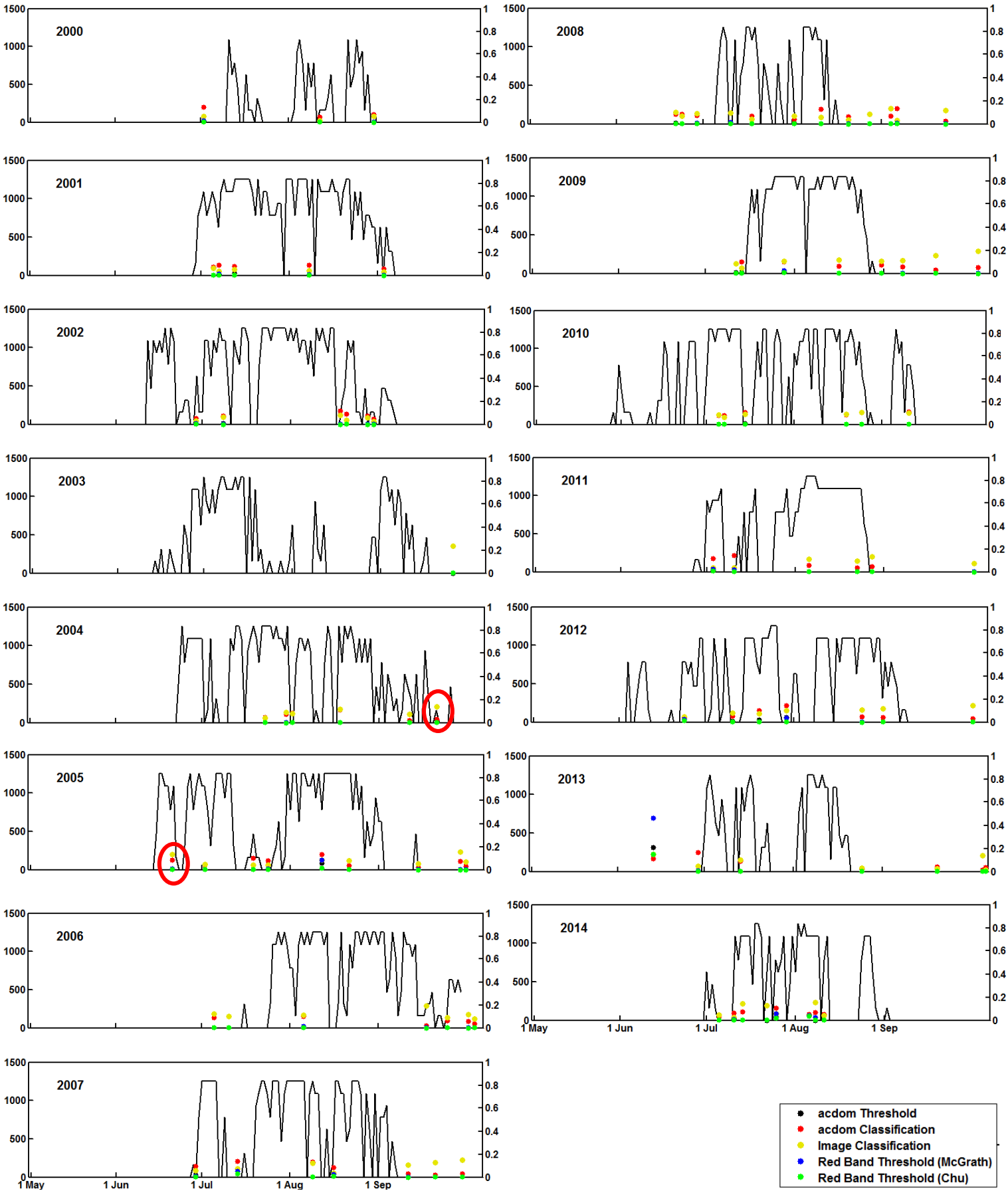

Figure 21 Outlet 2: plume areas derived from different methods (points) vs. daily melt extent in the catchment area during the melt season, 2000-2014

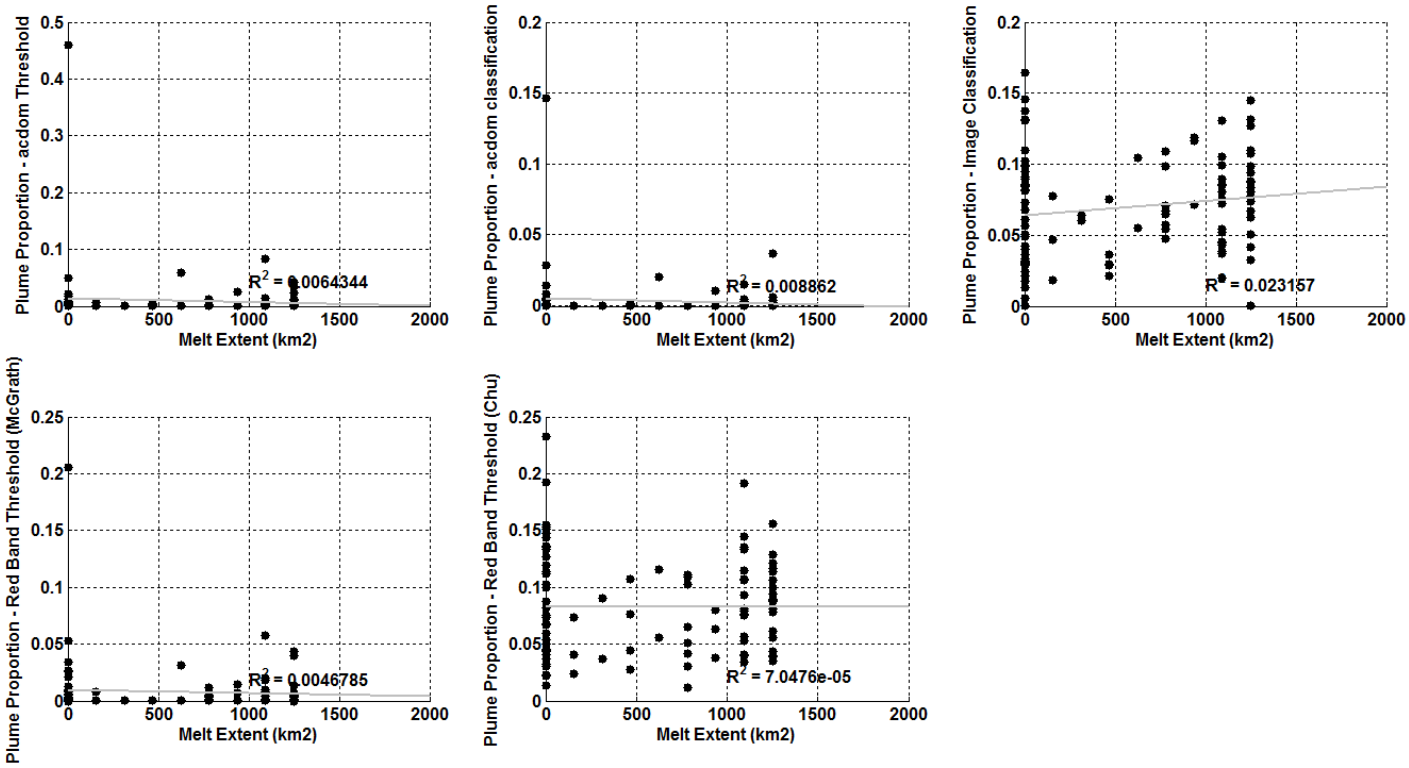

Figure 22 Outlet 2: scatter plots of melt extent (x axis) vs plume proportions derived by different methods (y axes).

More data points are available for Outlet 2 than Outlet 1 which allows for more detailed analysis on the two time series. Figure 21 shows that variations in plume proportions in Outlet 2 is relatively small within the melt season as well as inter-annually, and no apparent relationship is found between melt extent and meltwater runoff from this outlet. The same can be concluded from Figure 22, which again shows point clusters on the y axis corresponding to plumes captured later in the melt season when melt extent is found to be zero. This phenomenon is especially prominent for plume proportions derived from Chu's Red band threshold and also classification on the reflectance images.

Plume proportions generated by classification methods are generally larger than those derived from thresholding methods. Note that in 2003, 2007, 2009, 2012 and 2013, plume proportions derived by a_{CDOM} (red dots) generally follow the increasing and decreasing trend of the melt extent time series, and gradually drop to a low level towards melt season; however, plume proportions derived by classification of the original reflectance image remain at the same

level or slightly increase, which corresponds well with the behavior of plume proportions derived from reflectance image classification in Figure 22. This is suggestive of erronous classification of freshwater plumes by the classification on the original image, since exhausion of meltwater supply in late melt season followed by shrinking melt extent theoretically cannot result in an increase in freshwater runoff.

The scatterplot of plume proportions derived from thresholding methods and classification techniques (Figure 23) shows similar patterns to that from Outlet 1. a_{CDOM} thresholding (a & d) returns similar plume proportions to those derived by Red band thresholds, while classification methods returns consistently higher plume proportions than those from Red band thresholding (b,c,e and f).

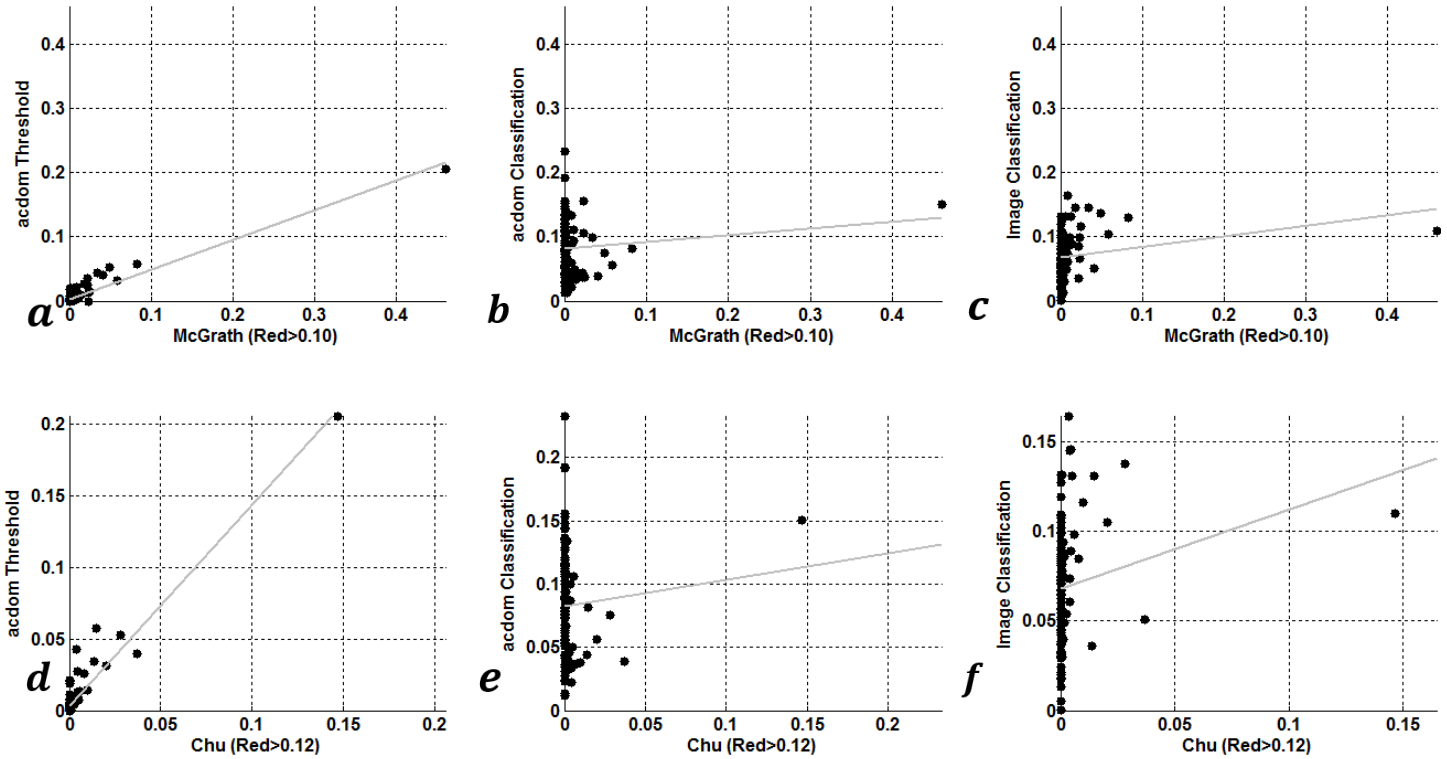

Figure 23 Outlet 2: Comparison between plume proportion derived from Red band thresholding (x axes) and methods proposed in this study (y axes).

Two examples of a detailed check at the difference between plume proportions derived by different methods are shown below. In both figures, the reflectance image suggests the existence of freshwater plume existing the outlet, and classification methods successfully capture

plume-like features while Red band thresholding methods fail to do so. Although peripheral plumes (in blue) can be very fragmented, core plume areas (in red) remain relatively coherent. For 15/9/2014 (Figure 24), a_{CDOM} thresholding fails to detect plume features as the a_{CDOM} levels are much lower than the collective threshold. However, a_{CDOM} thresholding does capture the core and peripheral plumes in the 18/6/2005 image, and the result is similar to that captured by a_{CDOM} classification. A look at these two dates on Figure 21 (data points within red circles) reveals that the melt extent is at a local peak in both dates, and the classification methods capture coincident freshwater output while Red band thresholding techniques do not, and a_{CDOM} thresholding captures plume features in one of these two dates. Also, for both dates, plume proportions derived from classification of the original reflectance image are larger than those derived from classification of the a_{CDOM} image, which is consistent with the findings above.

a)

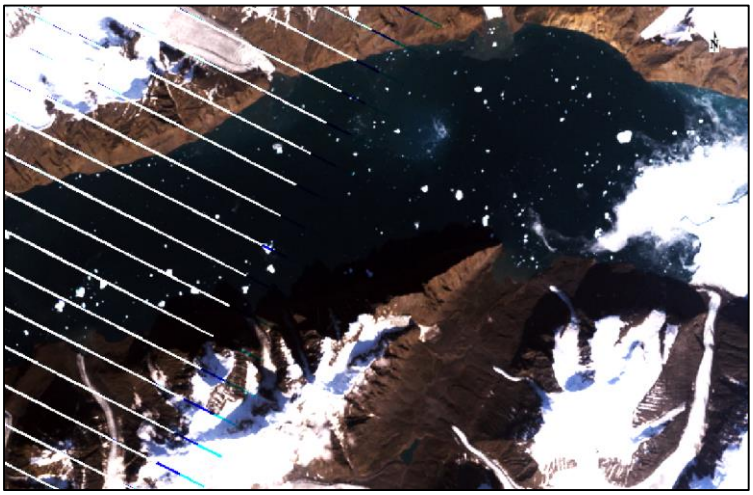

b)

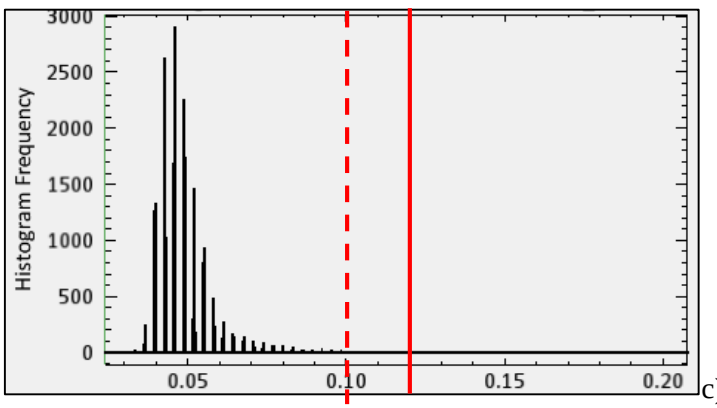

c)

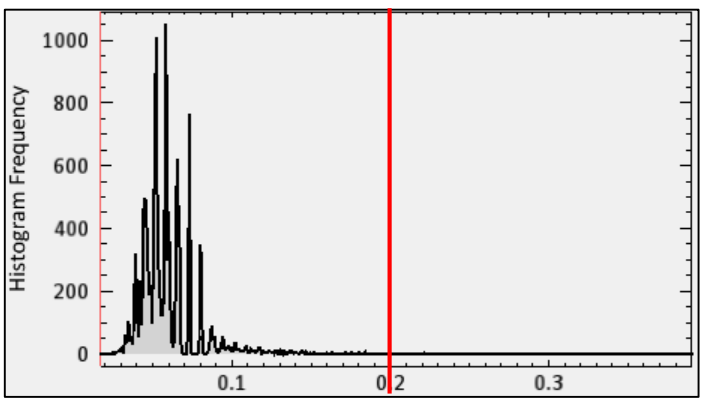

d) 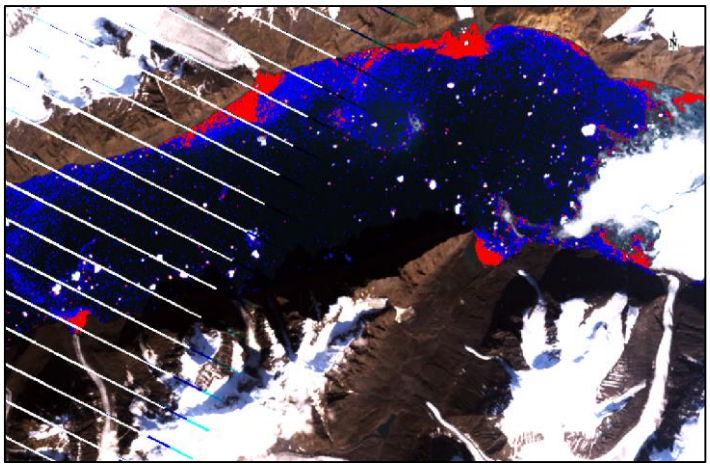

e) 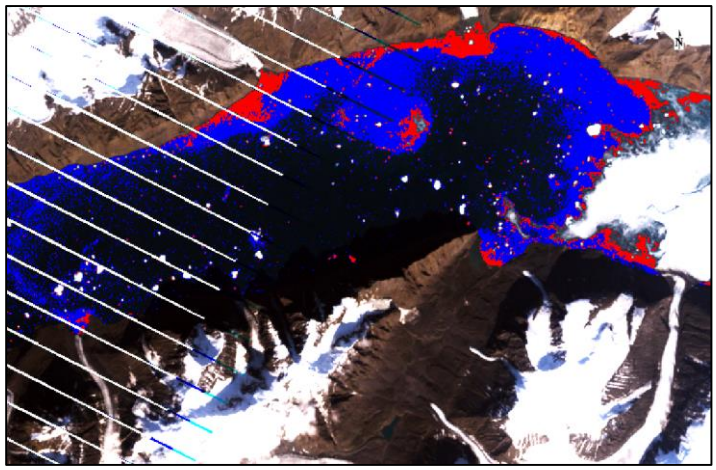

Figure 24 a) Original reflectance image: Outlet 2, 15/9/2004; b) Frequency distribution of reflectance values in Landsat Red band within the open water mask (dashed red line – Chu's Red band threshold: 0.12; solid red line – McGrath's Red band threshold: 0.10); c) Frequency distribution of acdom level within the open water mask (red line: acdom threshold: 0.2); d) Core plume (in red) and peripheral plume (in blue) extracted by classification of the acdom image; e) Core plume (in red) and peripheral plume (in blue) extracted by classification of the original image.

a) 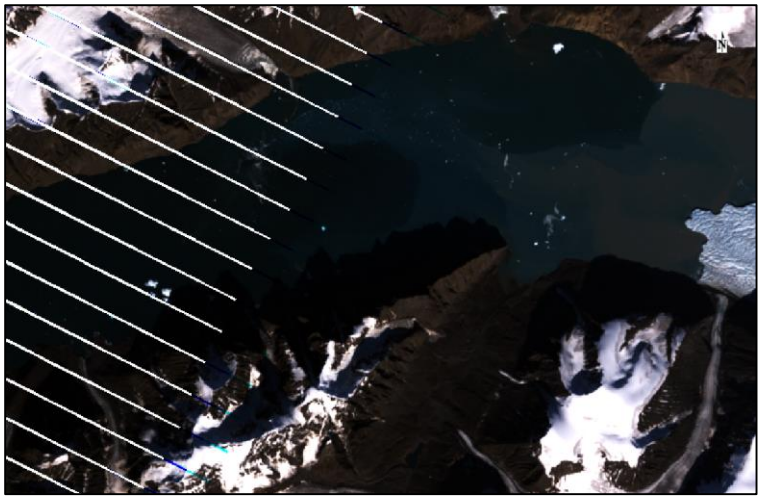

b) 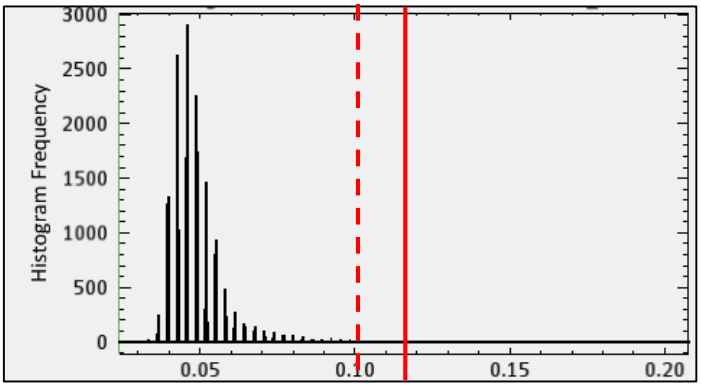

c) 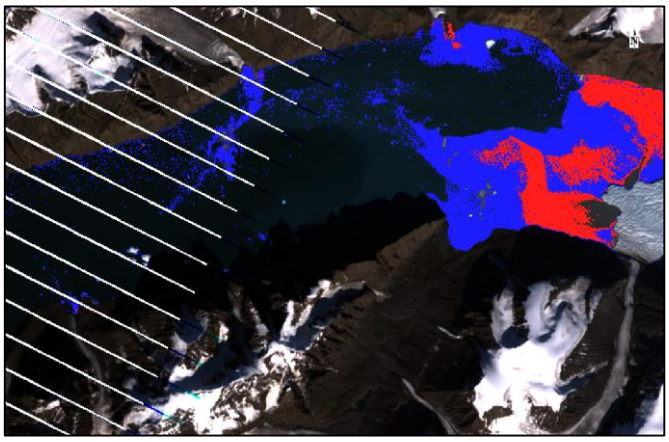

d) 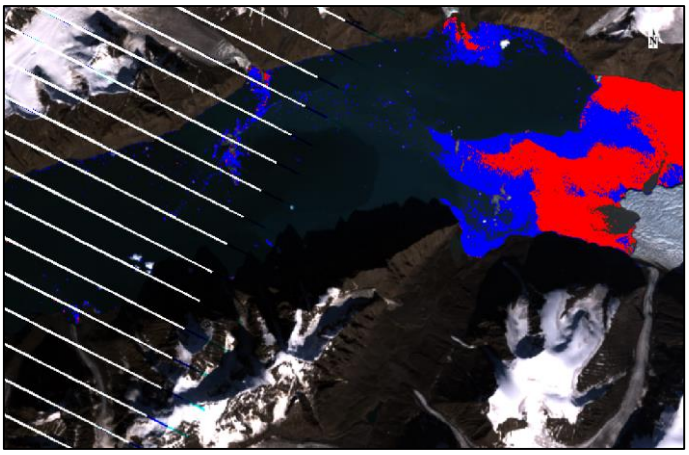 e) 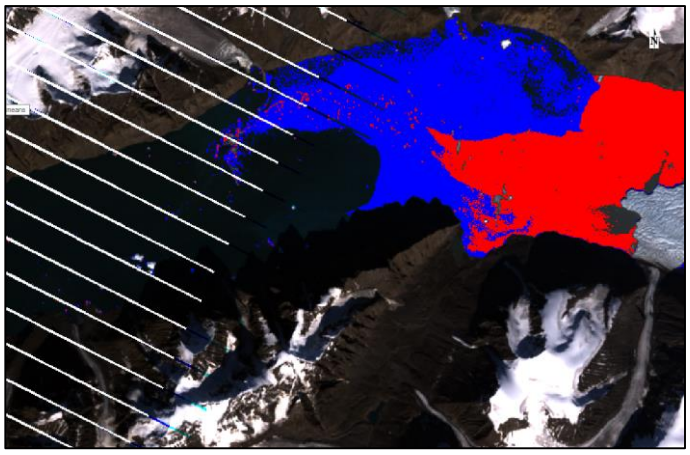

Figure 25 a) Original reflectance image: Outlet 2, 18/6/2005; b) Frequency distribution of reflectance values in Landsat Red band within the open water mask (dashed red line – Chu's Red band threshold: 0.12; solid red line – McGrath's Red band threshold: 0.10); c) Core plume (in red) and peripheral plume (in blue) extracted by acdom threshold; d) Core plume (in red) and peripheral plume (in blue) extracted by classification of the acdom image; e) Core plume (in red) and peripheral plume (in blue) extracted by classification of the original image.

4.1.2.3. Outlet 3

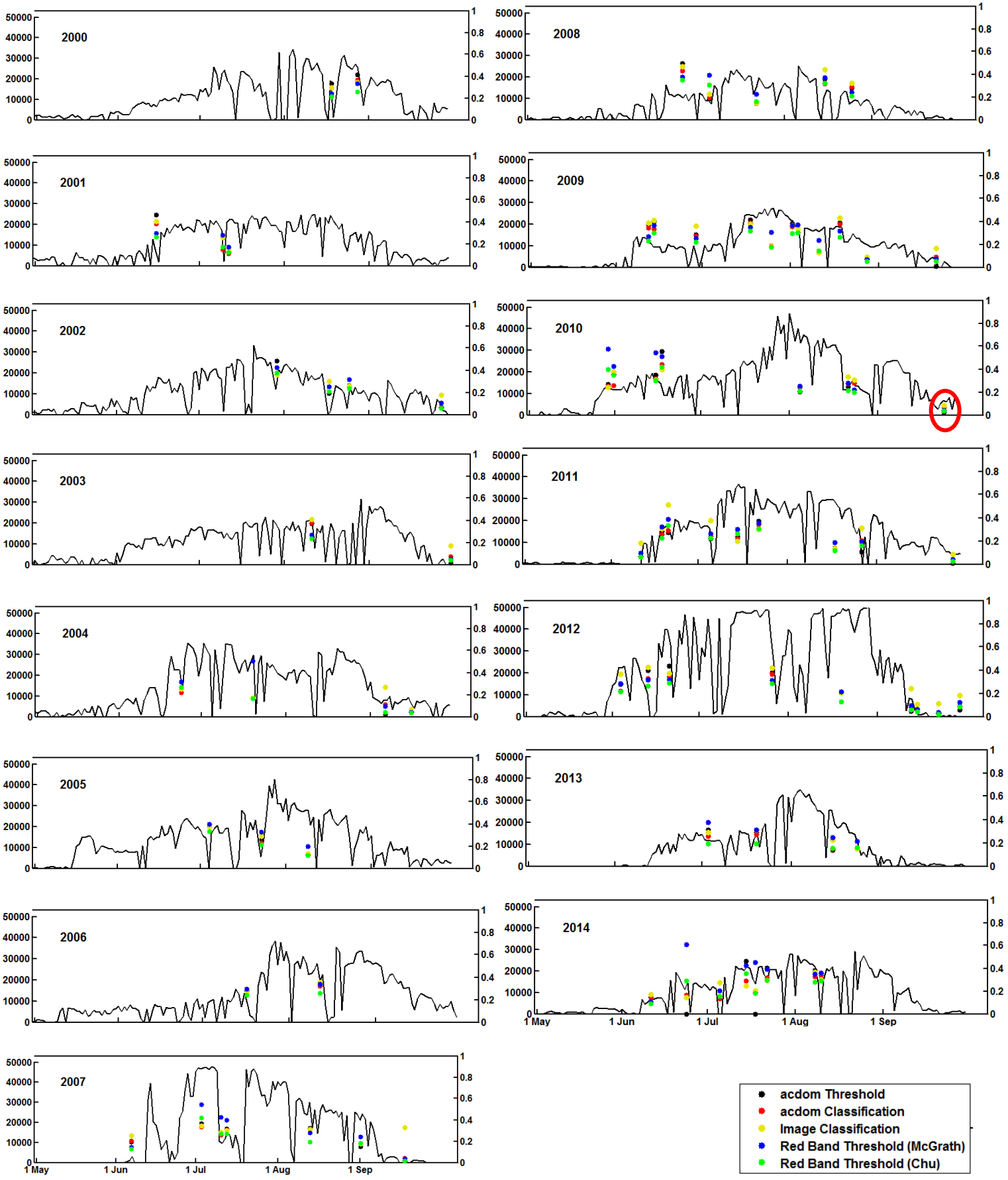

Figure 26 Outlet 3: plume areas derived from different methods (points) vs. daily melt extent in the catchment area during the melt season, 2000-2014

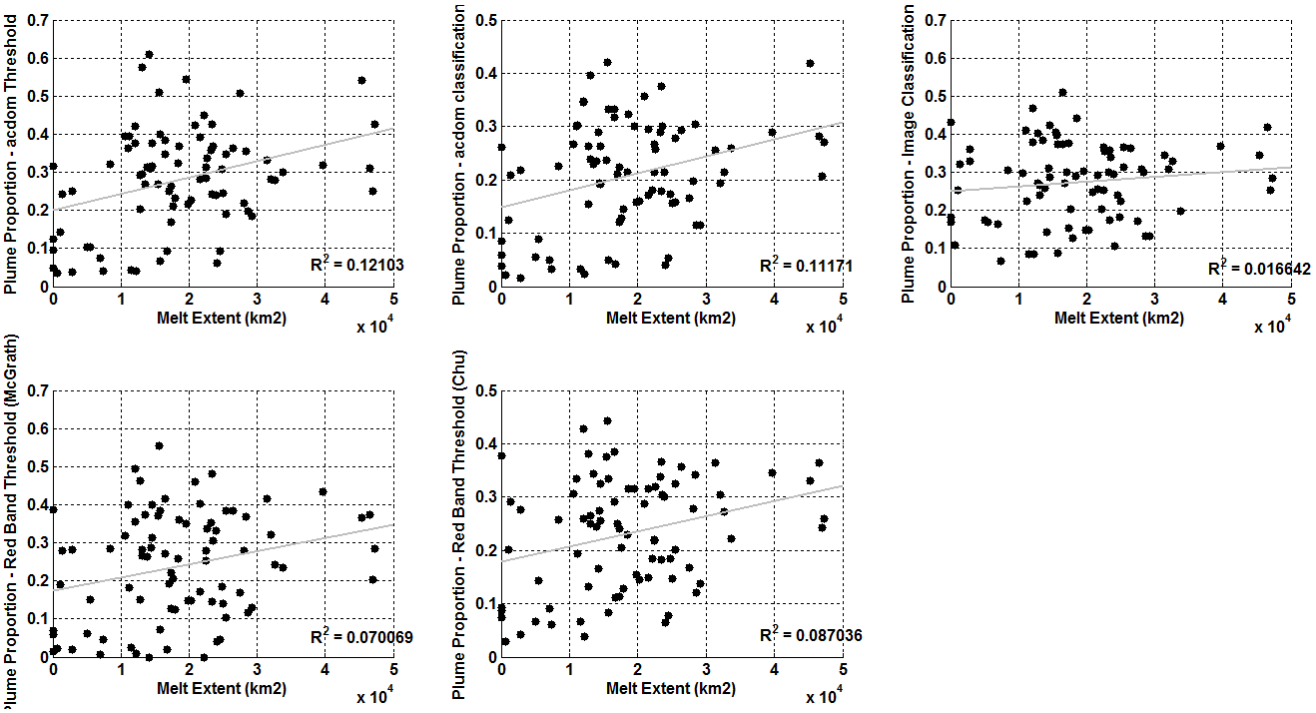

Figure 27 Outlet 3: scatter plots of melt extent (x axis) vs plume proportions derived by different methods (y axes).

From Figure 26, it can be seen that for Outlet 3, plume proportion time series generally trace melt extent better than the previous two outlets. Similar trends in the two time series can be identified in many dates, e.g. coincident local peaks in early July 2007, mid-July 2009, late June 2011, and mid-July 2014. Note that the 2007 and 2012 extreme melt record is registered in the melt extent in the catchment area as well as the plume proportions, which is not so much the case with Outlets 1 and 2, presumably due to the outlet's location further south from the previous two outlets and the larger size of the catchment area.

In the scatter plot of melt extent versus plum proportions (Figure 27), a more prominent relationship can be observed between the two datasets as the plume proportions generally increase with increasing melt extent. Also, all plume derivation methods now return comparable results, as can be seen from Figure 27 as well as the following figure showing the comparison between plume proportions derived from different methods. Plume proportions reported by plume derivation methods proposed in this study (a_{CDOM} threshold, a_{CDOM} classification, and classification on the original image) are generally lower than those generated by Red band thresholds. Note that the two plume extraction algorithms based on a_{CDOM} levels (a_{CDOM}

thresholding and classification on the a_{CDOM} image) returns plume proportions that better trace melt extent variation, as can be indicated by their slightly larger coefficient of determination values (R^2) in the linear regression models (Figure 27).

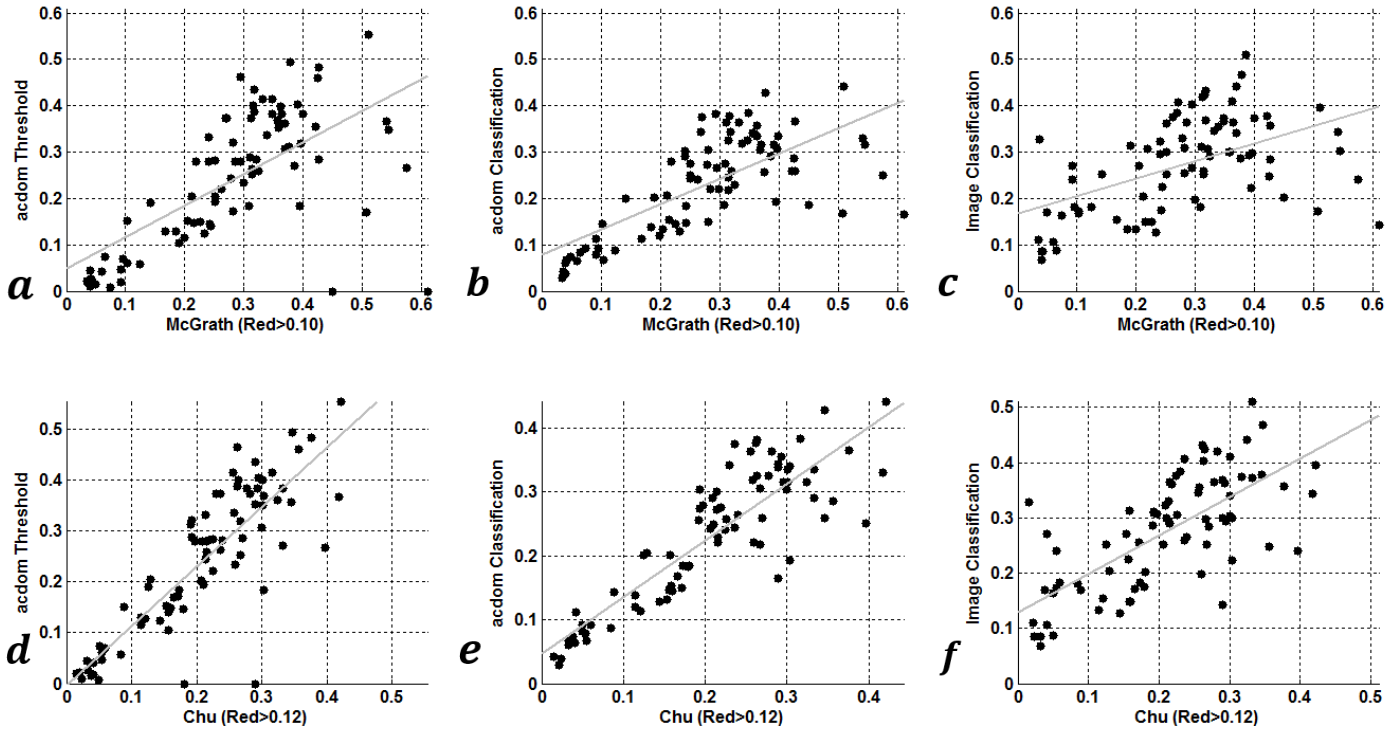

Figure 28 Outlet 3: Comparison between plume proportion derived from Red band thresholding (x axes) and methods proposed in this study (y axes).

Figure 29 shows an example image of Outlet 3 (4/8/2014) and plume identification by the five different methods. Both Red band thresholds (b & c) return similar and larger core plume sizes (in red) than those captured by the three other methods, and a_{CDOM} thresholding results in very similar core plume to those derived by classification methods in size and shape (d-f). Visual inspection suggests that the core plume area reported by a_{CDOM} thresholding and the two classification methods more closely trace the most turbid part of the freshwater output as seen in the reflectance image (a). The Red band thresholds that frequently return little or no plume size for the previous two outlets now likely overestimate the plume area due to generally higher SSC levels in Outlet 3. This again suggests the lack of adaptiveness of single thresholds that can result in different directions of potential errors in plume identification in different study sites.

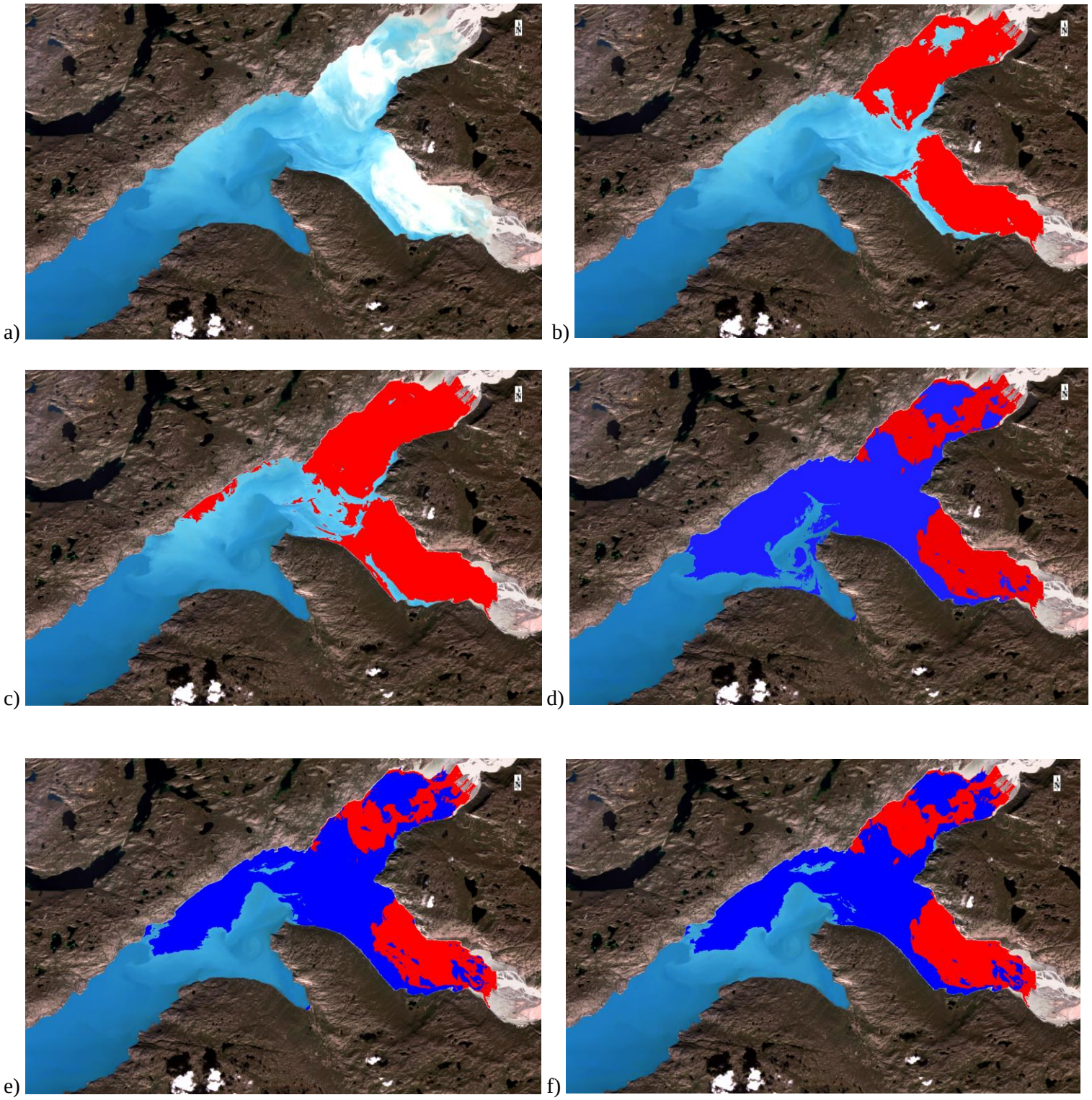

Figure 29 a) Original reflectance image: Outlet 3, 4/8/2014;
b) Core plume (in red) extracted by Chu's Red band threshold (>0.12)
c) Core plume (in red) extracted by McGrath's Red band threshold (>0.10)
d) Core plume (in red) and peripheral plume (in blue) extracted by acdom thresholds;
e) Core plume (in red) and peripheral plume (in blue) extracted by classification of the acdom image;
f) Core plume (in red) and peripheral plume (in blue) extracted by classification of the original image.

A more detailed look at Figure 24 reveals several occurences in late melt season when thresholding methods return very low plume proportions while those reported by classification

methods are significantly higher, which coincide with local peaks in melt extent, e.g. mid-September of 2002,2003, 2004, 2009, 2010 and 2012. This suggests the impact of limited sediment supply in late melt season which results in the failure of thresholding techniques to capture freshwater plumes using the predefined threshold. Further examination of these individual scenes support this hypothesis, and below (Figure 30) is an example (18/9/2010, as indicated by red circle in Figure 26) of this type of scenes. As can be visually interpreted from the reflectance image (a), visible freshwater plumes carrying suspended sediments are exiting from both water channels. Both Red band thresholds (b) and a_{CDOM} threshold (c) return negligible plume areas, while classification methods (d & e) captures reasonble core and pheripheral plume areas as can be interpreted from the reflectance image. Note that the core plume areas to the top right of the scene is partially covered by cloud, which is filtered out by the open water mask and results in the fregmented core plumes identified by the classification methods. Therefore, it can be infered that classification methods are more resistent to the effect of low sediment supply in early or late melt season which can cause failure in freshwater plume identification from thresholding techniques.

a) 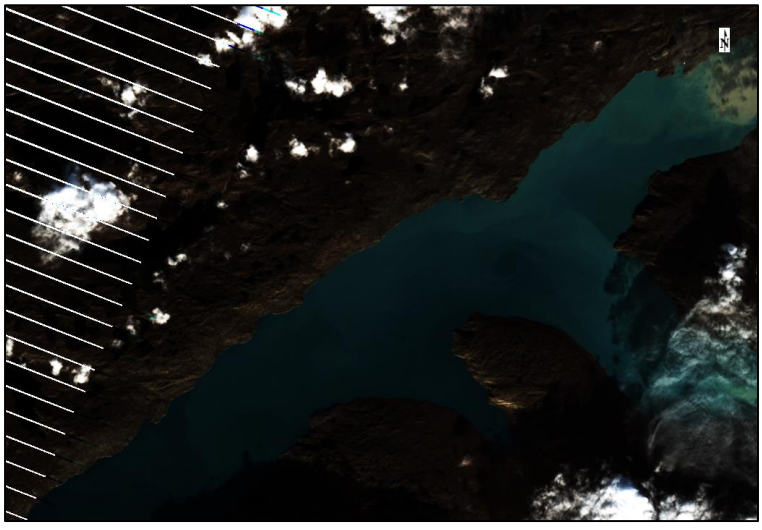

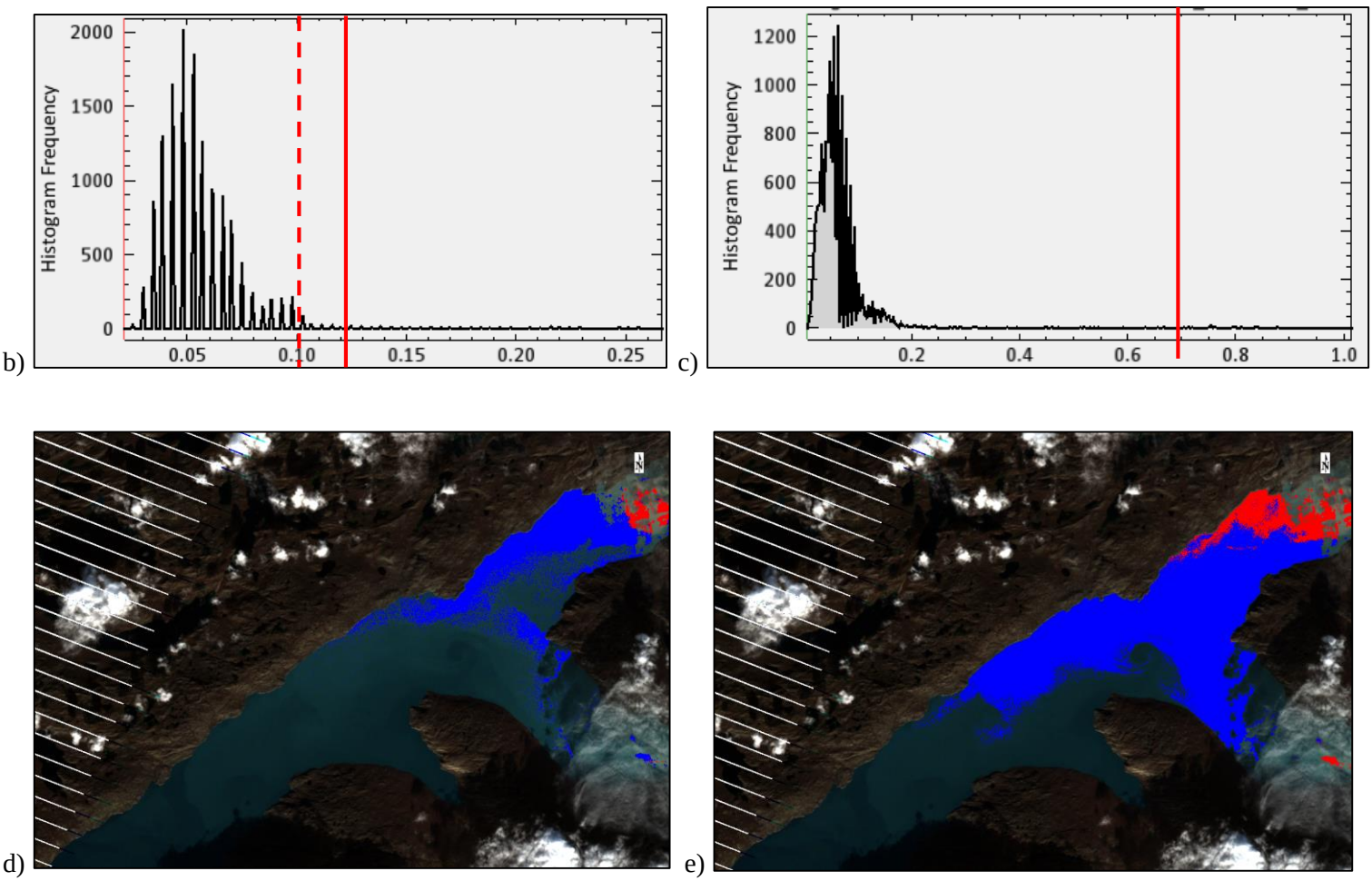

Figure 30 a) Original reflectance image: Outlet 3, 18/9/2010; b) Frequency distribution of reflectance values in Landsat Red band within the open water mask (dashed red line – Chu's Red band threshold: 0.12; solid red line – McGrath's Red band threshold: 0.10); c) Frequency distribution of acdom level within the open water mask (red line: acdom threshold: 0.7); d) Core plume (in red) and peripheral plume (in blue) extracted by classification of the acdom image; e) Core plume (in red) and peripheral plume (in blue) extracted by classification of the original image.

4.1.2.4. Outlet 4

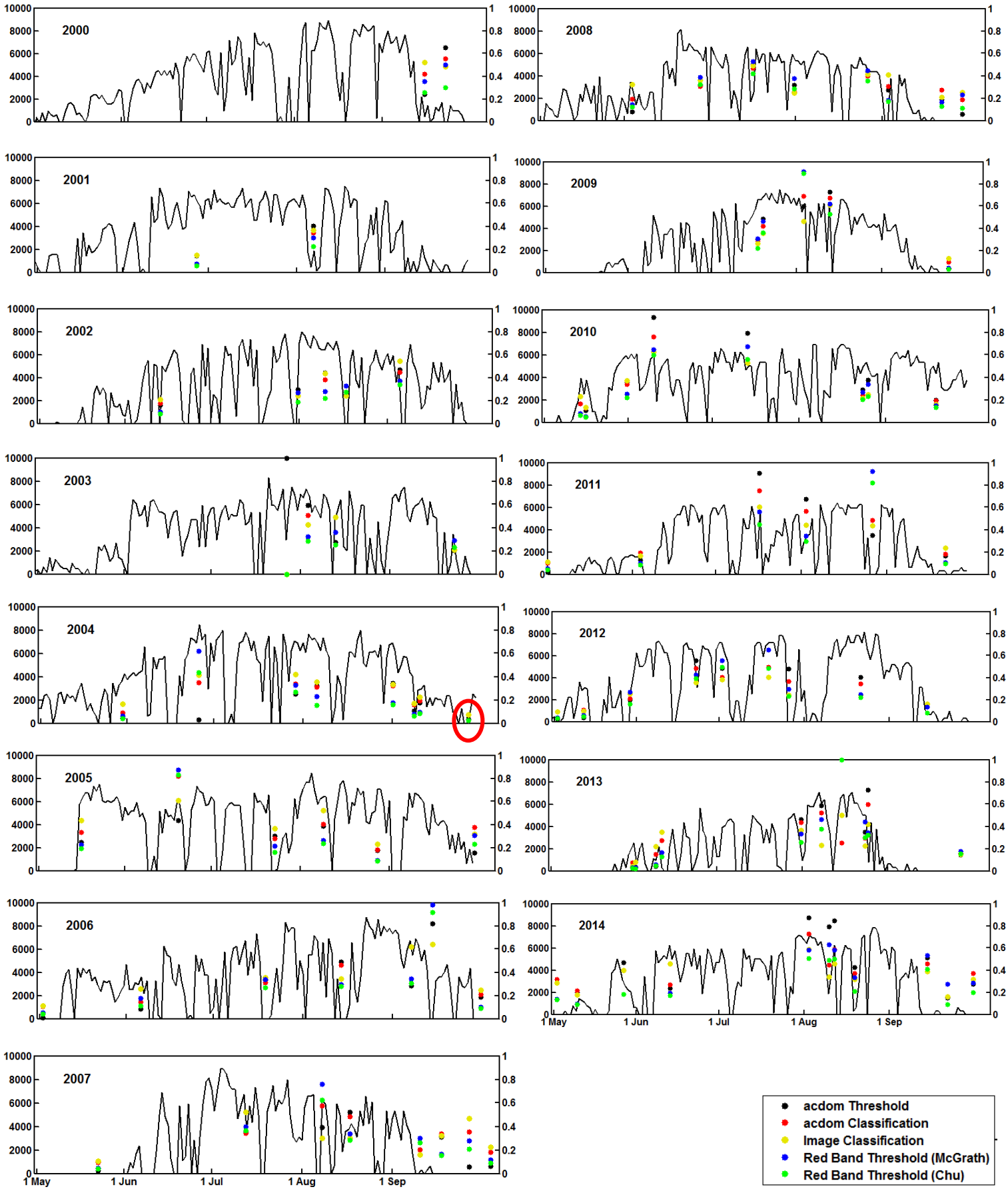

Figure 31 Outlet 4: plume areas derived from different methods (points) vs. daily melt extent in the catchment area during the melt season, 2000-2014

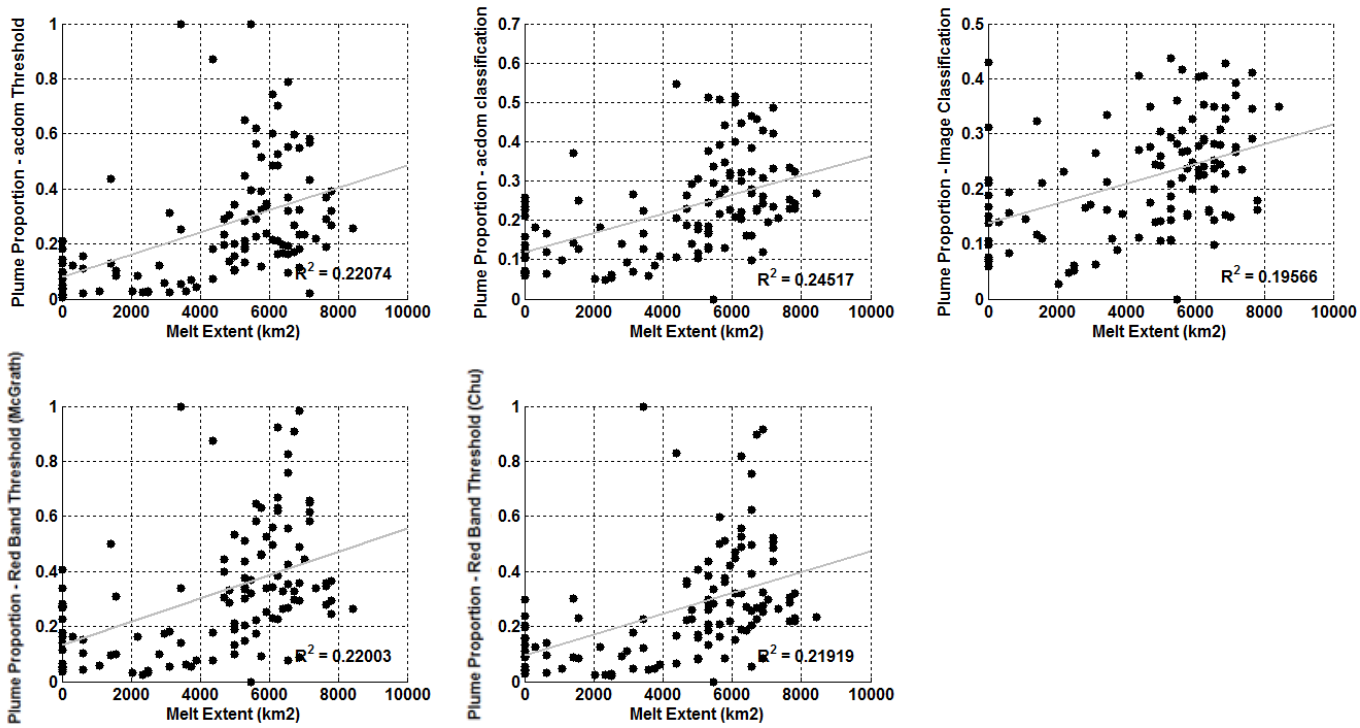

Figure 32 Outlet 4: scatter plots of melt extent (x axis) vs plume proportions derived by different methods (y axes).

Plume proportions in Outlet 4 generally follow the trend in melt extent time series (Figure 31), which is better recognized in the years when more plume proportion records area available, e.g. 2007, 2009, 2011, 2012 and 2014. Similar to Outlet 3, classification methods (red and yellow) tend to report higher plume proportions in early and late melt seasons than other methods, e.g. late September 2002, 2003, 2009, 2010, 2011 and 2012 and early June 2007 and 2009. Also similar to Outlet 3, Red band thresholding generally report higher plume proportions than those derived using the three methods in this study (Figure 31 and Figure 33). Note that the two plume derivation methods based on the use of a_{CDOM} levels again more closely trace variations in corresponding melt extents, suggested by their higher R^2 values (Figure 32).

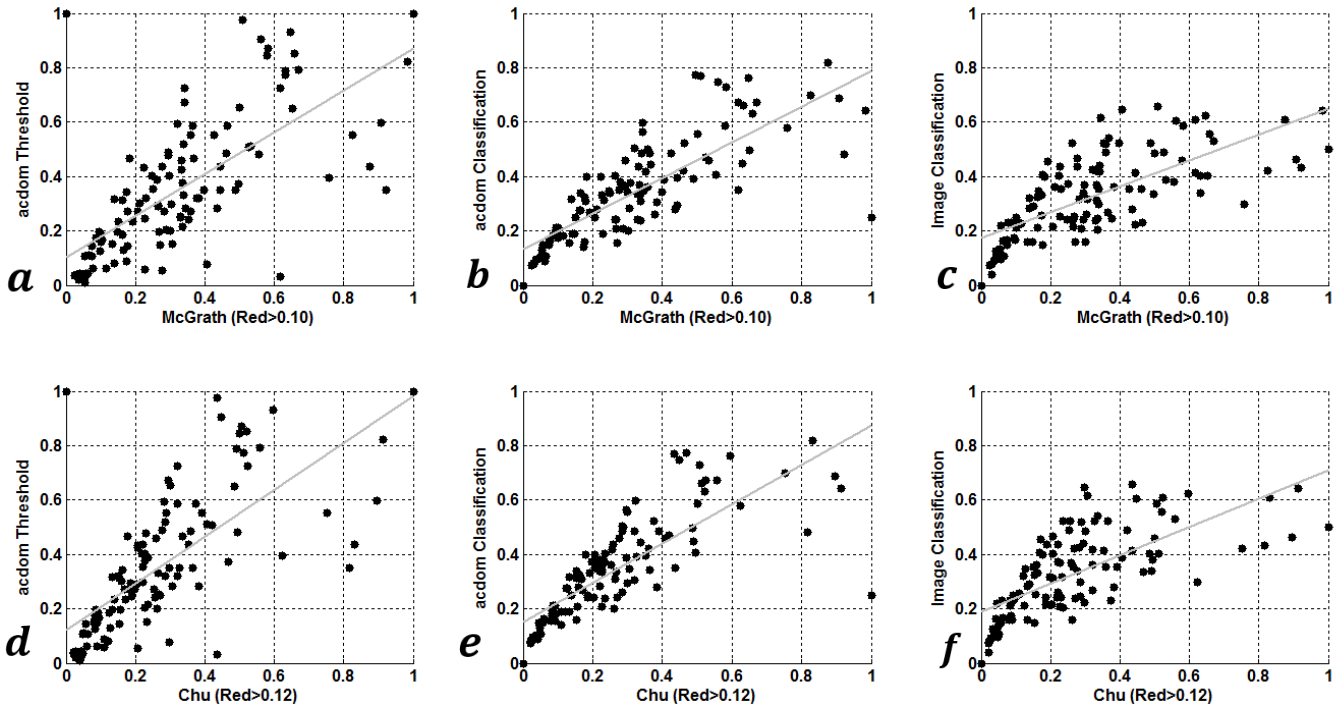

Figure 33 Outlet 4: Comparison between plume proportion derived from Red band thresholding (x axes) and methods proposed in this study (y axes).

Below is an example scene (8/9/2014) covering Outlet 4, showing core plume areas extracted by the five different methods. As expected, Red band thresholds generate higher core plume (in red) proportions which are similar in shape and size to peripheral plumes identified by other methods (b & c). a_{CDOM} threshold, a_{CDOM} classification and classification on the reflectance image produce very similar core plumes (d-f).

a) 

b) 

c)  d) 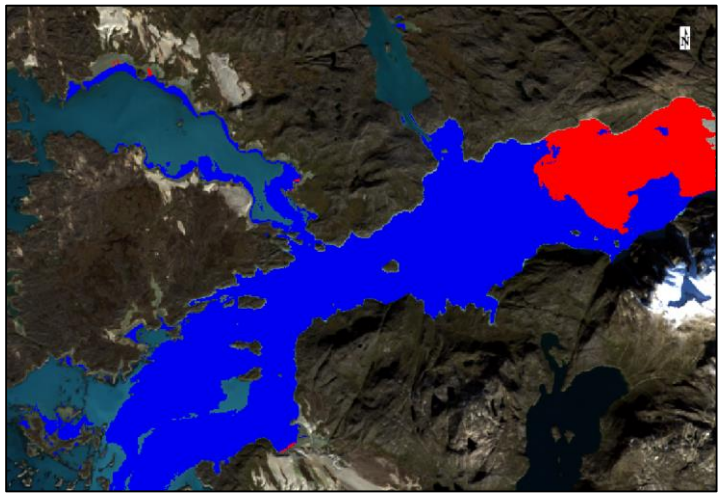

e) 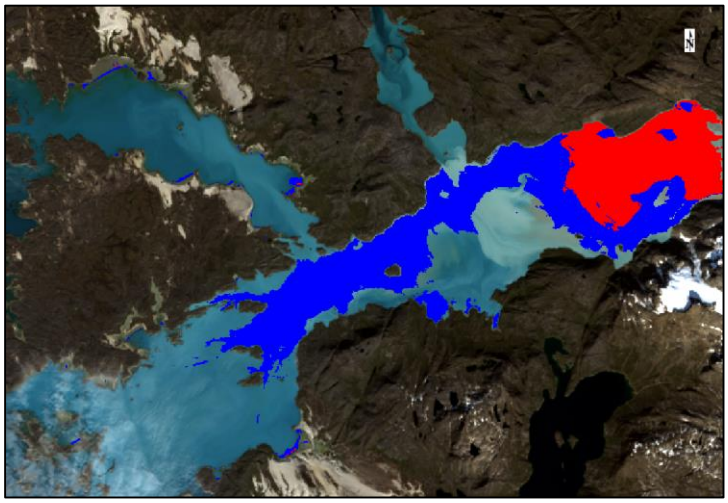 f) 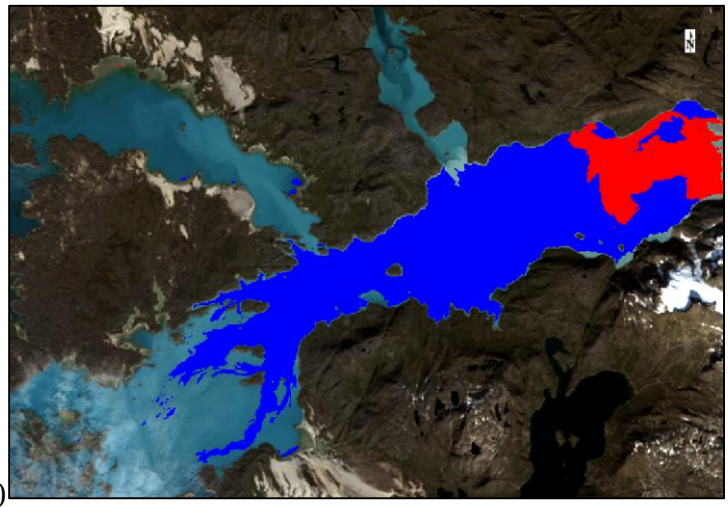

Figure 34 a) Original reflectance image: Outlet 4, 8/9/2014;
b) Core plume (in red) extracted by Chu's Red band threshold (>0.12)
c) Core plume (in red) extracted by McGrath's Red band threshold (>0.10)
d) Core plume (in red) and peripheral plume (in blue) extracted by acdom thresholds;
e) Core plume (in red) and peripheral plume (in blue) extracted by classification of the acdom image;
f) Core plume (in red) and peripheral plume (in blue) extracted by classification of the original image.

In order to test the hypothesis of classification methods being more reliable options for plume delineation especially in late melt season, scenes at these times of year in which classification methods return significantly higher plume proportions than thresholding methods are manually examined, and an example (21/9/2004) is shown in Figure 35 (also circled in red in Figure 31). Visual inspection suggests the existence of turbid plume exiting the outlet on this day, which is

not picked up by either the Red band thresholds or the a_{CDOM} threshold (b & c). Both classification methods (d & e) managed to capture plume-like features, with the core plume part (in red) corresponding reasonably well with the plume feature seen in the reflectance image (a).

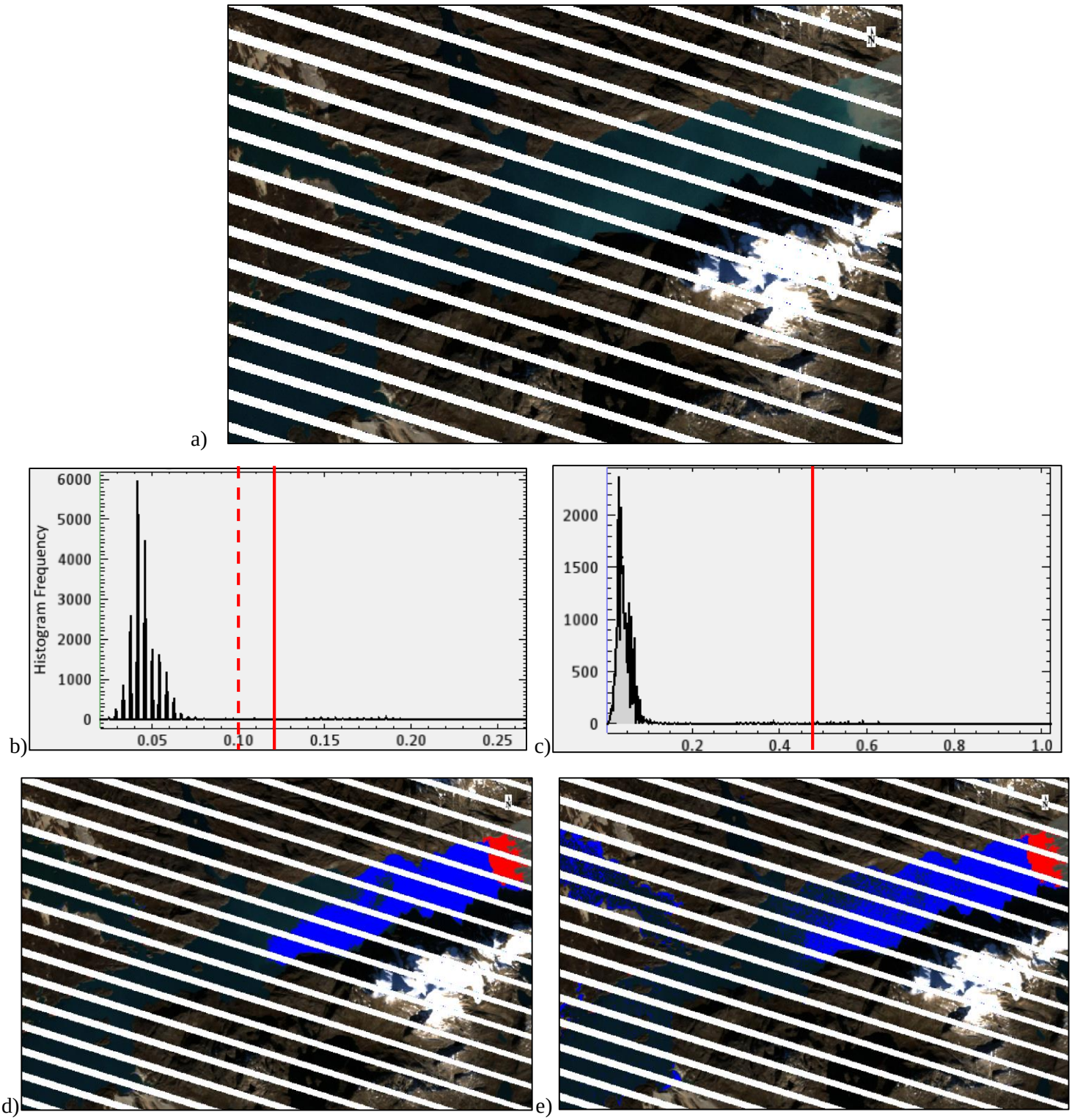

Figure 35 a) Original reflectance image: Outlet 4, 21/9/2004; b) Frequency distribution of reflectance values in Landsat Red band within the open water mask (dashed red line – Chu's Red band threshold: 0.12; solid red line – McGrath's Red band threshold: 0.10); c) Frequency distribution of acdom level within the open water mask (red line: acdom threshold: 0.44); d) Core plume (in red) and peripheral plume (in blue) extracted by classification of the acdom image; e) Core plume (in red) and peripheral plume (in blue) extracted by classification of the original image.

5. DISCUSSION

5.1. Performance of proposed freshwater plume delineation methods

This study explores the possibility of using a_{CDOM} as an indicator of freshwater output from Greenland's glacier outlets, and multiple adaptive plume extraction methods have been examined for their performance in delineating reliable plume features. The performance of these three methods, when compared with Red band thresholds, can be evaluated from two perspectives: inter-comparison between plume proportions derived from each method, and the comparison between plume proportion time series generated by these methods to the variations in melt extent.

The Chu et al. (2012) threshold of 0.12 on the Red band is a conservative choice in order to avoid over-sampling open water region covered by melting ice which is spectrally similar to turbid water. Thus, it produces consistently lower plume proportions than the McGrath et al. (2010) threshold of 0.10. Due to the fact that these thresholds are derived using site-specific studies, their perform inconsistently when being applied to deriving plumes in other locations. In the two land-terminating glaciers (Outlet 3 and 4) where average SSCs are higher, these thresholding methods produce large sediment plume areas, while in the other two outlets, they tend to fail in capturing plume features that are proved to exist by visual inspection. Also, the apparente seasonal hysteresis as reported by previous studies shows that in late melt season when sediment supply has been exhausted, sediment plumes as delineated using the threshold derived from average SSC levels can no longer serve as a reliable indicator of meltwater runoff variations. As discussed earlier, comparisons between the time series of melt extent and plume proportions have revealed many occasions in the late melt season when plume proportions have dropped to near zero while melt extents have not experienced significant decrease, or is even in local peaks. Therefore, it can be concluded that the Red band thresholding technique cannot serve as a viable method of plume delineation when the algorithm is expected to be used to derive plume features in a variety of different regions across long time spans.

The a_{CDOM} thresholding method utilizes the collective information from all available scenes and can objectively delineate plume features that are comparable through different scenes. However, similar to the Red band thresholds, using cut points derived from a collective histogram inevitably means that there are likely to be scenes in which the a_{CDOM} level is too low to be detected by this pre-defined threshold, much like the case with suspended sediments. Compared to the two classification methods, plume proportions derived from the a_{CDOM} thresholding method are more similar to that derived from the Red band tresholding methods, although in some scenes the a_{CDOM} thresholding method manages to capture plume features like the classification method while Red band thresholds cannot (e.g. Figure 25).

The two classification methods have shown to have the most consistent performance when applied to different regions. They are able to detect plume features in late melt season when pre-defined thresholds fail to capture meltwater output carrying significantly lower amount of sediment or CDOM. It should be noted that in this study, plume proportions derived from classification on the reflectance image are consistenly higher than that derived from classification on the a_{CDOM} image. Moreover, classification on the reflectance image often produces plume prorpotions that exhibit unrealistic late melt season increase even when melt extent has dropepd to zero, and in the meantime plume proportions derived from a_{CDOM} classification closer traces melt extent variations. Presumably this is related to the information from the extra bands added to the classification which may not be constructive for the derivation of freshwater signal. The detailed reason behind this systematic difference remains unclear. As discussed earlier, visual check at plume areas derived from these two methods also tend to support the result from a_{CDOM} classification judging from the plume features visible from the reflectance images. Thus, it can be concluded that the a_{CDOM} classification method can be considered as the optimal approach of freshwater plume delineation in this study.

5.2. Sources of error in plume delineation

Due to the limited availability of usable Landsat data, scenes are included in the analysis as long as the study areas are not completely obsured by cloud cover (although a 40% cloud cover threshold is applied when selecting scenes). This along with other data limitations has lead to multiple sources of potential errors (loss of plume areas) in the extraction of freshwater plume features. These errors are only partially offset by the use of proportion of freshwater plume in open water surface.

a. Loss of plume area covered by clouds
b. Loss of plume area covered by sea ice (especially in outlets at higher latitudes)
c. Scenes with incomplete coverage of the outlet area (Landsat 7 image gaps and image borders cutting the study areas)
d. Scenes outside the 1 May – 30 September period that still have detectable CDOM levels (although mostly very low) are excluded from the study (e.g. Figure 36 (d)).

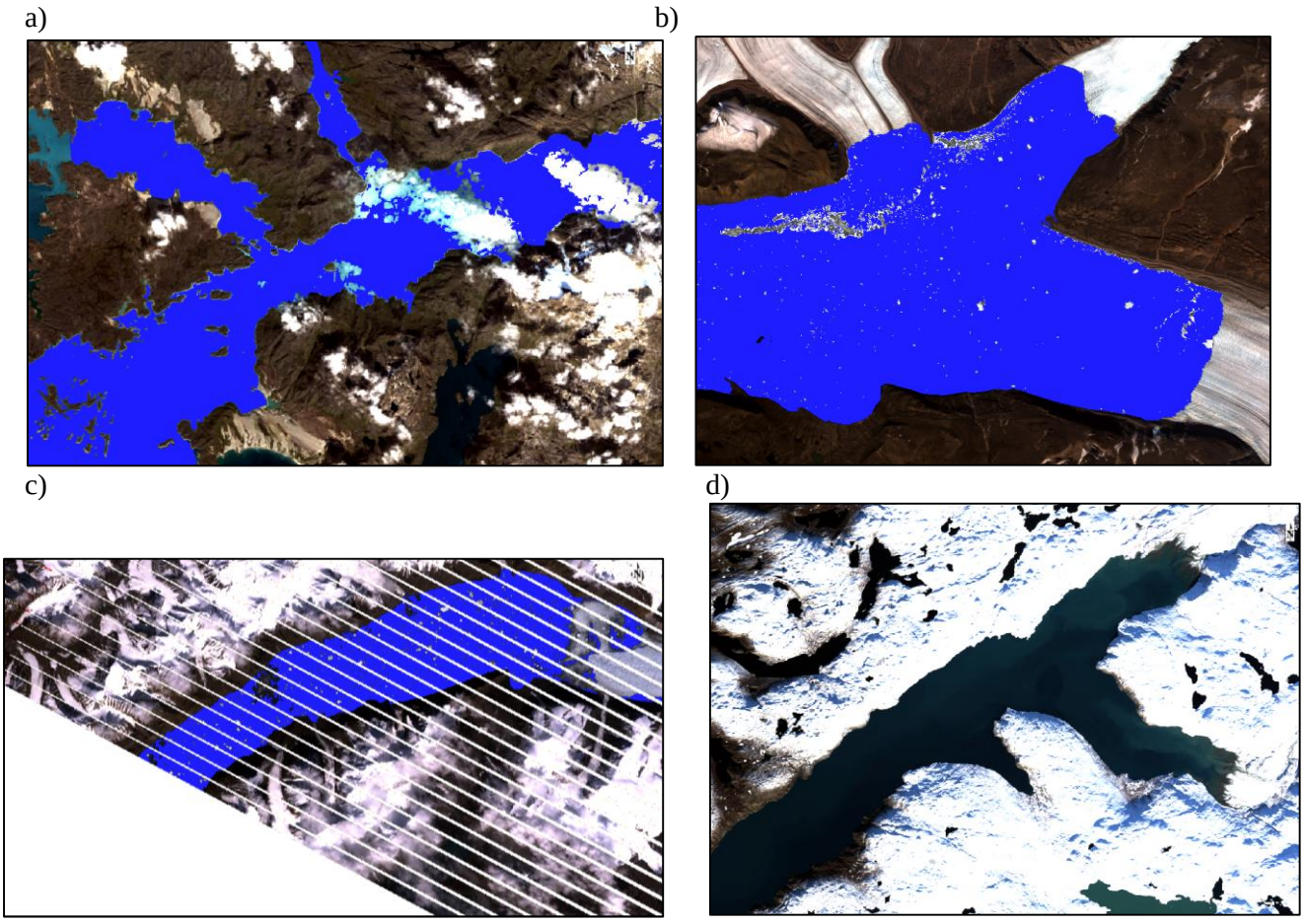

Figure 36 Examples of losses of plume areas. a) Outlet 4, 15/8/2014; b) Outlet 1, 12/8/2014; c) Outlet 2, 5/8/2007; d) Outlet 3, 7/10/2014. Darker blue indicate open water body included in the analysis.

5.3. Future work

A key limitation in this study is the poor availability of cloud-free Landsat scenes. Preivous studies have utilized MODIS imegery for plume delineation which provides much better temporal coverage. During the past decade, a number of spatio-temporal data assimilation algorithms have been developed aiming at combining the advantage of data having high spatial resolution and those having high temporal resolution, e.g. the Spatial Temporal Adaptive Reflectance Fusion Model (STARFM) developed by Gao et al. (2006), the method of spatio-temporal Kriging with external drift developed by Snepvangers et al. (2003) and other geostatistical methods (Kyriakidis & Journel 1999). The application of a model that fully takes into consideration spatio-temporal structure in assimilating temporally frequent coarse resolution data (e.g. MODIS data) with fine resolution images having larger temporal interval (e.g. Landsat data) can potentially deliver a much more detailed time series of plume area than derived in this study. Also, since the freshwater plume extraction method provided in this study is fully automated, it has the potential to be implemented in an inventory study of freshwater output from all the glacier outlet along the Greenland coast given a dataset with both find spatial and temporal resolution is achievable through the approaches suggested above.

This study only analyses plume areas, while preivous research found that sediment concentration has better geographic covariance with surface melt, and plume dimensions best capture interannual runoff dynamics (Chu et al. 2012). Future work can involve the inclusion of SSC into the analysis and possiblity the development of a new index that combines plume dimensions and SSC, e.g. plume dimension weighted by SSC. This approach can be expected to both capture spatial and temporal variations in meltwater release from the GrIS.

Through the examination of plume derivation for the two marine-terminating outlets (Outlet 3 and Oulet 4), apparent switching of plume locations across the melt season as well as interannually has been discovered. Figure 38 is an example comparison of typical core plume locations in Outlet 4 (marked as location A and location B). Note that the the white fragment

extending from plume location B in Figure 38 (a) is sea ice, and no plume is detetcted emenating from location B on this day.

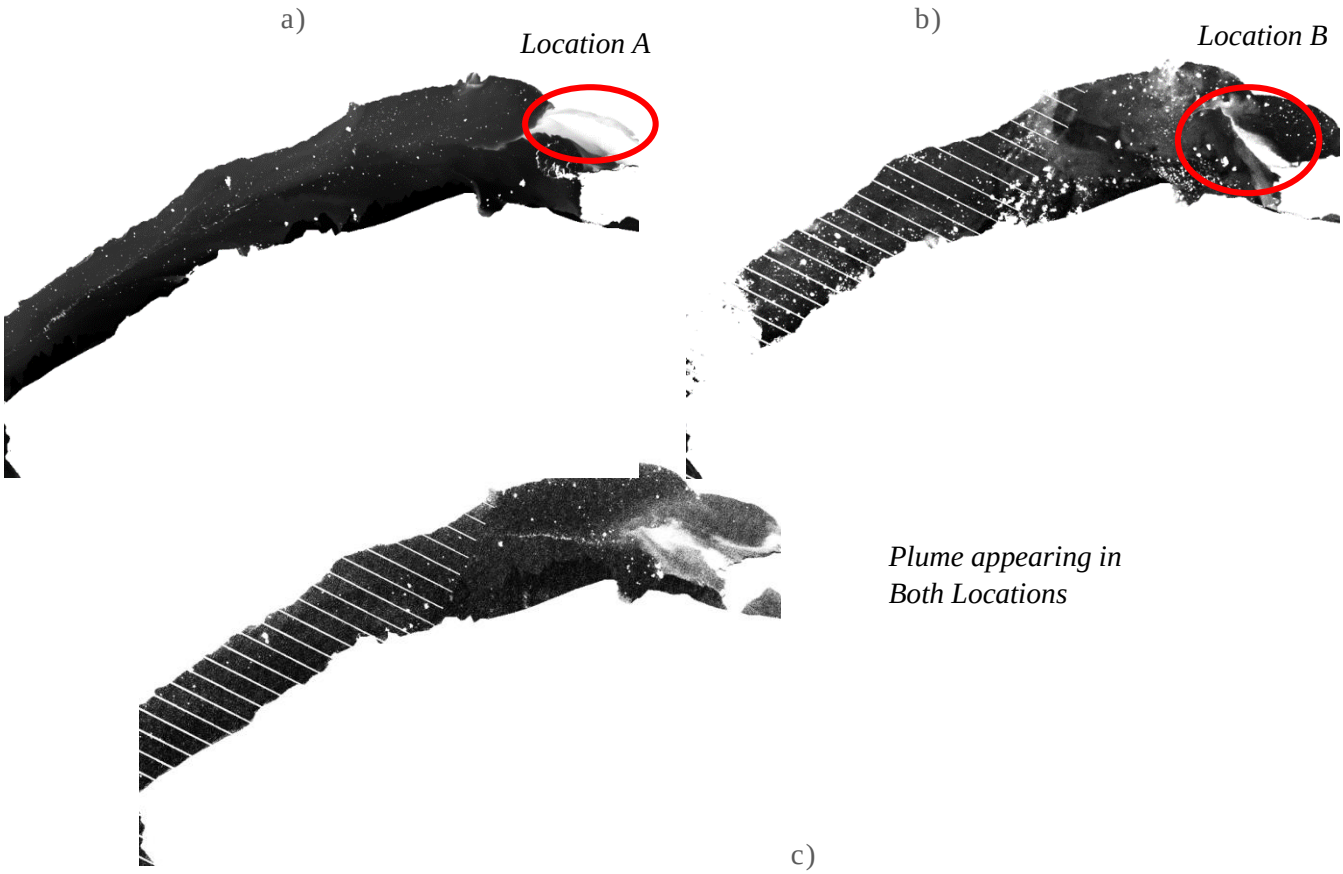

Figure 37 Examples of freshwater plumes appearing in Location A, B and both locations in Outlet 4. a) 27/6/2013; b) 2/8/2013; c) 1/9/2008.

From a visual examination of plume locations throughout the time series, an approximate trend can be identified. Figure 38 summarizes the day of year in which each type of plume location (A or B) is observed from 2000 to 2014. It can be seen from the distribution that location B tend to appear earlier in the melt season while plumes in location A generally appear later, which potentially indicates plume switching associated with variations in englacial or subglacial meltwater routing. There is a substantial period of time when plumes are detected in both locations, indicating inter-annual variations in the switching time. Also, days in which plumes only exist in one location (either Location A: orange in Figure 38 or Location B: blue) have an apparent converging trend, i.e. days with only Location A plumes have generally moved towards

earlier in the melt season from 2000 to 2014, while Location B plumes have the opposite trend, suggesting faster switching of plume location (and presumably closing and opening of different en- or sub-glacial conduits) as the switching time (when plumes appear in both locations) shortens.

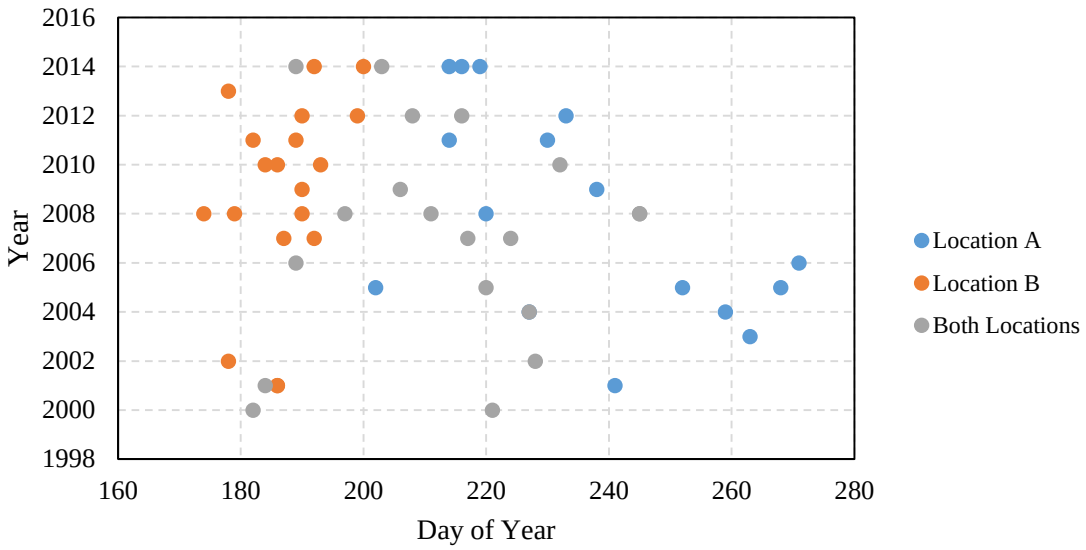

Figure 38 Distribution of plumes appearing in Location A, B and both locations during the melting seasons (1 May to 30 September) in the study period (2000-2014)

Given these discoveries, future work may involve the development of a hydrological model to simulate the configuration of the subglacial drainage system for different assumptions of the steady state subglacial water pressures (which might be expected in different years in response to melt variations). Then, the modelled locations of subglacial conduits at the front where meltwater exits the glacier can be compared against the plume observations.

6. CONCLUSION

A reliable quantification of Greenland's meltwater output is vital in mass balance modelling of the ice sheet. The detection and continous monitoring of this variable is only possible through the use of data from remote sensing platforms. Preivous studies have attempted to use suspended sedimetn in glaicer outlets as an indication of freshwater runoff. However, these studies invariably utilizes a single threshold of one MODIS spectral band in delineating sediment plumes, which can result in unsatisfactory retrieval of plume characteristics due to the fact that these thresholds are derived from site- and time-specific experiments. Also the 250m spatial resolution of MODIS imagery limites the accuracy of plume delineation, especially in narrower outlets expanding only several pixels. Moreover, the use of suspended sediment as an indication of freshwater output can be unreliable, especially in later melt season when sediment exchausion may occur.

This study is an exploratory attempt at solving the above issues in remote sensing of meltwater runoff in Greenland. A new variable, the absorption coefficient of CDOM, or a_{CDOM}, is used to detect the presence and dimensions of freshwater plumes. Three experimental adaptive plume extraction approaches have been implemented and compared in terms of their performance in reliable retrieval of freshwater plumes. This study uses Landsat 7 ETM+ and Landsat 8 OLI imagery in capturing freshwater information, thus providing substantially more details in plume characteristics. Melt areas in the catchment areas of each of the selected glacier outlets are calculated from SSM-I/SSMIS brightness temperature records for comparison with the derived plume area time series.

The two time series track each other more closely for the two land-terminating glaciers. Due to the limitation in the availability of Landsat scenes, quantitative analysis of short-term variations in plume characteristics is not feasible. The presence of land-fast ice, sea ice and icebergs in the marine-terminating margins result in substantial loss of open water surface which interferes with plume retrieval. The method of thresholding the Red band have inconsistent performance in different regions: the pre-defined thresholds result in large plume areas in land-

terminating glacier outlets where SSC is high, and freuqently fail to capture freshwater plumes in marine-terminating margins with lower sediment loads. These methods also have trouble in capturing plume features in late melt season when sediment supply exhausion occurs. Thresholding on the a_{CDOM} images based on cut points automatically generated from collective histograms have similar plume derivation results to the two Red band thresholding methods in that it also fails to capture plume features in the scenes with substantially lower a_{CDOM} levels than average.

The two classification methods perform more consistently in plume retireval due to the fact that they are based on individual information from each scene. Thus, the issue of late melt season exchausion of sediment supply does not have an impact on plume derivation using these methods. However, classification on the entire Landsat image spectrum returns persistently larger freshwater plume areas, and plume proportions derived from this method frequently display a late-melt season increase, which does not agree with trends in the melt extent. On the other hand, classification on the a_{CDOM} images is capable of producing consistent and reliable plume areas not captured by thresholding technqiues, and the annual average plume proportions derived by this method correlate best with melt records. Therefore, among the three plume extraction methods, classification on individual a_{CDOM} image is considered optimal, which has the potential of making remote sensing of estuary freshwater plumes a more reliable tool for monitoring the variability of ice sheet meltwater release.

7. REFERENCE

A. Bjørk, a., M. Kruse, L. & B. Michaelsen, P., 2015. Brief Communication: Getting Greenland's glaciers right – a new dataset of all official Greenlandic glacier names. *The Cryosphere Discussions*, 9(2), pp.1593–1601.

Abdalati, W. & Steffen, K., 1995. Passive microwave-derived snow melt regions on the Greenland Ice Sheet. *Geophysical Research Letters*, 22(7), pp.787–790.

Ahn, Y.H. et al., 2008. Satellite remote sensing of a low-salinity water plume in the East China Sea. *Annales Geophysicae*, 26, pp.2019–2035.

Alsdorf, D.E., Rodr ́guez, E. & Lettenmaier, D.P., 2007. Measuring surface water from space. *Reviews of Geophysics*, 45(2), p.RG2002.

Van Angelen, J.H. et al., 2013. Rapid loss of firn pore space accelerates 21st century Greenland mass loss. *Geophysical Research Letters*, 40(10), pp.2109–2113.

Armstrong, R. et al., 1994. DMSP SSM/I-SSMIS Pathfinder Daily EASE-Grid Brightness Temperatures. Version 2.

Bartholomew, I. et al., 2011. Supraglacial forcing of subglacial drainage in the ablation zone of the Greenland ice sheet. *Geophysical Research Letters*, 38(8), p.n/a–n/a.

Bartholomew, P., 2002. *Mapping and Modeling Chlorophyll- a Concentrations in the Lake Manassas Reservoir Using Landsat Thematic Mapper Satellite Imagery Master of Science In*. Virginia Polytechnic Institute.

Bernstein, L.S. et al., 2005. Validation of the QUick Atmospheric Correction (QUAC) Algorithm for VNIR-SWIR Multi- and Hyperspectral Imagery. *Proceedings of SPIE*, 5806, pp.668–678.

Bowers, D.G. et al., 2000. Optical Properties of a Region of Freshwater Influence (The Clyde Sea). *Estuarine, Coastal and Shelf Science*, 50(5), pp.717–726.

Van den Broeke, M. et al., 2009. Partitioning recent Greenland mass loss. *Science (New York, N.Y.)*, 326(2003), pp.984–986.

Carder, K.L. et al., 1999. Semianalytic Moderate-Resolution Imaging Spectrometer algorithms for chlorophyll a and absorption with bio-optical domains based on nitrate-depletion temperatures. *Journal of Geophysical Research: Oceans*, 104(C3), pp.5403–5421.

Choi, H. & Bindschadler, R., 2004. Cloud detection in Landsat imagery of ice sheets using shadow matching technique and automatic normalized difference snow index threshold value decision. *Remote Sensing of Environment*, 91(2), pp.237–242.

Chu, V.W. et al., 2012. Hydrologic controls on coastal suspended sediment plumes around the Greenland Ice Sheet. *The Cryosphere*, 6(1), pp.1–19.

Chu, V.W. et al., 2009. Sediment plume response to surface melting and supraglacial lake drainages on the Greenland ice sheet. *Journal of Glaciology*, 55(194), pp.1072–1082.

Department of the Interior & U.S. Geological Survey, 2012. *Landsat Data Continuity Mission (LDCM) Mission Data Data Format Control Book (DFCB)*,

Doxaran, D. et al., 2002. Spectral signature of highly turbid waters: Application with SPOT data to quantify suspended particulate matter concentrations. *Remote Sensing of Environment*, 81, pp.149–161.

Du, Z. et al., 2014. Analysis of Landsat-8 OLI imagery for land surface water mapping. *Remote Sensing Letters*, 5(7), pp.672–681.

Fenn, C.R., 1987. Sediment transfer processes in Alpine glacier basins. *Glacio-Fluvial Sediment Transfer: An Alpine Perspective. John Wiley and Sons, New York New York. 1987. p 59-85, 4 fig, 4 tab, 86 ref.*

Fettweis, X. et al., 2013. Brief communication "Important role of the mid-tropospheric atmospheric circulation in the recent surface melt increase over the Greenland ice sheet." *The Cryosphere*, 7(1), pp.241–248.

Ficek, D., Zapadka, T. & Dera, J., 2011. Remote sensing reflectance of Pomeranian lakes and the Baltic**The study was partially financed by MNiSW (Ministry of Science and Higher Education) as a research project N N306 066434 in the years 2008–2011. The partial support for this study was also pro. *Oceanologia*, 53(4), pp.959–970.

Fountain, A.G., 1996. Effect of Snow and Firn Hydrology on the Physical and Chemical Characteristics of Glacial Runoff. *Hydrological Processes*, 10(4), pp.509–521.

Gao, F. et al., 2006. On the blending of the Landsat and MODIS surface reflectance: predicting daily Landsat surface reflectance. *Geoscience and Remote Sensing, IEEE Transactions on*, 44(8), pp.2207–2218.

Griffin, C.G. et al., 2011. Spatial and interannual variability of dissolved organic matter in the Kolyma River, East Siberia, observed using satellite imagery. *Journal of Geophysical Research: Biogeosciences*, 116(3), pp.1–12.

Hall, D.K., Riggs, G. a & Salomonson, V. V, 1995. Development of methods for mapping global snow cover using moderate resolution imaging spectroradiometer data. *Remote Sensing of Environment*, 54(2), pp.127–140.

Hanna, E. et al., 2013. Atmospheric and oceanic climate forcing of the exceptional Greenland ice sheet surface melt in summer 2012. *International Journal of Climatology*, p.n/a–n/a.

Hanna, E. et al., 2011. Greenland Ice Sheet surface mass balance 1870 to 2010 based on Twentieth Century Reanalysis, and links with global climate forcing. *Journal of Geophysical Research D: Atmospheres*, 116(24).

Hanna, E. et al., 2005. Runoff and mass balance of the Greenland ice sheet: 1958-2003. *Journal of Geophysical Research: Atmospheres*, 110, pp.1–16.

Heide-Jørgensen, M.P. et al., 2007. Springtime coupling between chlorophyll a, sea ice and sea surface temperature in Disko Bay, West Greenland. *Progress in Oceanography*, 73(1), pp.79–95.

Hock, R., 2005. Glacier melt: a review of processes and their modelling. *Progress in Physical Geography*, 29(3), pp.362–391.

Hopkins, J. et al., 2013. Detection and variability of the Congo River plume from satellite derived sea surface temperature, salinity, ocean colour and sea level. *Remote Sensing of Environment*, 139, pp.365–385.

Jansson, P., Hock, R. & Schneider, T., 2003. The concept of glacier storage: A review. *Journal of Hydrology*, 282(1-4), pp.116–129.

Jenks, G.F., 1967. The Data Model Concept in Statistical Mapping. In *International Yearbook of Cartography 7*. pp. 186–190.

Ji, L., Zhang, L. & Wylie, B., 2009. Analysis of Dynamic Thresholds for the Normalized Difference Water Index. *Photogrammetric Engineering & Remote Sensing*, 75(11), pp.1307–1317.

Kim, S.-W., Hong, S.-H. & Won, J.-S., 2005. An application of L-band synthetic aperture radar to tide height measurement. *Geoscience and Remote Sensing, IEEE Transactions on*, 43(7), pp.1472–1478.

Kyriakidis, P. & Journel, A., 1999. Geostatistical Space–Time Models: A Review. *Mathematical Geology*, 31(6), pp.651–684.

Lee, Z., Carder, K.L. & Arnone, R.A., 2002. Deriving inherent optical properties from water color: a multiband quasi-analytical algorithm for optically deep waters. *Applied Optics*, 41(27), pp.5755–5772.

Legleiter, C.J. et al., 2014. Mapping the bathymetry of supraglacial lakes and streams on the Greenland ice sheet using field measurements and high-resolution satellite images. *Cryosphere*, 8(1), pp.215–228.

Lewis, S.M. & Smith, L.C., 2009. Hydrologic drainage of the Greenland Ice Sheet. *Hydrological Processes*, 23(14), pp.2004–2011.

Li, X., 2013. Understanding China ' s Behavioral Change in the WTO Dispute Settlement System : Power , Capacity , and Normative Constraints in Trade Adjudication understanding China ' s Behavioral Change in the WTo Dispute Settlement System. *Asian Survey*, 52(6), pp.1111–1137.

Mankoff, K.D. et al., 2012. The role of pine island glacier ice shelf basal channels in deep-water upwelling, polynyas and ocean circulation in pine island bay, antarctica. *Annals of Glaciology*, 53(60), pp.123–128.

Mannino, A., Russ, M.E. & Hooker, S.B., 2008. Algorithm development and validation for satellite-derived distributions of DOC and CDOM in the U.S. Middle Atlantic Bight. *Journal of Geophysical Research: Oceans*, 113(7), pp.1–19.

Marghany, M. & Hashim, M., 2011. A numerical method for retrieving sea surface salinity from MODIS satellite data. , 6(13), pp.3116–3125.

Maxwell, S.K., Schmidt, G.L. & Storey, J.C., 2007. A multi-scale segmentation approach to filling gaps in Landsat ETM+ SLC-off images. *International Journal of Remote Sensing*, 28(23), pp.5339–5356.

McFeeters, S.K., 1996. The use of the Normalized Difference Water Index (NDWI) in the delineation of open water features. *International Journal of Remote Sensing*, 17(7), pp.1425–1432.

McGrath, D. et al., 2010. Sediment plumes as a proxy for local ice-sheet runoff in Kangerlussuaq Fjord, West Greenland. *Journal of Glaciology*, 56(199), pp.813–821.

Mernild, S.H. et al., 2008. Jökulhlaup Observed at Greenland Ice Sheet. *Eos, Transactions American Geophysical Union*, 89(35), p.321.

Mernild, S.H. et al., 2010. Runoff and mass-balance simulations from the Greenland Ice Sheet at Kangerlussuaq (S??ndre Str??mfjord) in a 30-year perspective, 1979-2008. *Cryosphere*, 4(2), pp.231–242.

Mernild, S.H. et al., 2011. Surface mass balance and runoff modeling using HIRHAM4 RCM at Kangerlussuaq (S??ndre Str??mfjord), West Greenland, 1950-2080. *Journal of Climate*, 24(3), pp.609–623.

Mernild, S.H. & Hasholt, B., 2009. ¨kulhlaups and suspended sediment load Observed runoff , jo from the Greenland ice sheet at Kangerlussuaq , West Greenland , 2007 and 2008. , 55(193), pp.855–858.

Miller, R.L. & McKee, B. a., 2004. Using MODIS Terra 250 m imagery to map concentrations of total suspended matter in coastal waters. *Remote Sensing of Environment*, 93, pp.259–266.

Monahan, E.C. & Pybus, M.J., 1978. Colour, ultraviolet absorbance and salinity of the surface waters off the west coast of Ireland. *Nature*, 274(5673), pp.782–784.

Palacios, S.L., Peterson, T.D. & Kudela, R.M., 2009. Development of synthetic salinity from remote sensing for the Columbia River plume. *Journal of Geophysical Research: Oceans*, 114(4), pp.1–14.

Parry, V. et al., 2007. Investigations of meltwater refreezing and density variations in the snowpack and firn within the percolation zone of the Greenland ice sheet. *Annals of Glaciology*, 46, pp.61–68.

Petus, C. et al., 2010. Estimating turbidity and total suspended matter in the Adour River plume (South Bay of Biscay) using MODIS 250-m imagery. *Continental Shelf Research*, 30(5), pp.379–392.

Rignot, E. et al., 2011. Acceleration of the contribution of the Greenland and Antarctic ice sheets to sea level rise. *Geophysical Research Letters*, 38(5), pp.1–5.

Ritchie, J.C., Cooper, C.M. & Schiebe, F.R., 1990. The relationship of MSS and TM digital data with suspended sediments, chlorophyll, and temperature in Moon Lake, Mississippi. *Remote Sensing of Environment*, 33, pp.137–148.

Roy, D.P. et al., 2008. Multi-temporal MODIS–Landsat data fusion for relative radiometric normalization, gap filling, and prediction of Landsat data. *Remote Sensing of Environment*, 112(6), pp.3112–3130.

Snepvangers, J.J.J.., Heuvelink, G.B.. & Huisman, J.., 2003. Soil water content interpolation using spatio-temporal kriging with external drift. *Geoderma*, 112(3-4), pp.253–271.

Stedmon, C.A., Granskog, M.A. & Dodd, P.A., 2015. An approach to estimate the freshwater contribution from glacial melt and precipitation in East Greenland shelf waters using colored dissolved organic matter (CDOM). *Journal of Geophysical Research: Oceans*, 120(2), pp.1107–1117.

Stott, T. a. & Grove, J.R., 2001. Short-term discharge and suspended sediment fluctuations in the proglacial Skeldal River, north-east Greenland. *Hydrological Processes*, 15(3), pp.407–423.

Tedesco, M. et al., 2013. Evidence and analysis of 2012 Greenland records from spaceborne observations, a regional climate model and reanalysis data. *The Cryosphere*, 7(2), pp.615–630.

Tedesco, M. et al., 2008. Extreme Snowmelt in Northern Greenland During Summer 2008. *Eos, Transactions American Geophysical Union*, 89(41), p.391.

Tedesco, M. et al., 2015. Greenland Ice Sheet. *Arctic Report Card 2015*, pp.22–31. Available at: http://www.arctic.noaa.gov/reportcard/.

Tedesco, M. et al., 2011. The role of albedo and accumulation in the 2010 melting record in Greenland. *Environmental Research Letters*, 6(1).

Tedstone, A.J. & Arnold, N.S., 2012. Automated remote sensing of sediment plumes for identification of runoff from the Greenland ice sheet. *Journal of Glaciology*, 58(210), pp.699–712.

Torbick, N. et al., 2008. Mapping Chlorophyll- a Concentrations in West Lake, China using Landsat 7 ETM+. *Journal of Great Lakes Research*, 34(3), pp.559–565.

Turner, D., 2010. *Remote sensing of chlorophyll a concentrations to support the Deschutes Basin lake and reservoir TMDLs*,

Urquhart, E. a. et al., 2012. Remotely sensed estimates of surface salinity in the Chesapeake Bay: A statistical approach. *Remote Sensing of Environment*, 123(November 2009), pp.522–531.

USGS, 2004. SLC-off Gap-Filled Products. Gap-Fill Algorithm Methodology. , pp.1–12.

Wadham, J.L. & Nuttall, A.M., 2002. Multiphase formation of superimposed ice during a mass-balance year at a maritime high-Arctic glacier. *Journal of Glaciology*, 48(163), pp.545–551.

Wang, F. & Xu, Y.J., 2008. Development and application of a remote sensing-based salinity prediction model for a large estuarine lake in the US Gulf of Mexico coast. *Journal of Hydrology*, 360(1-4), pp.184–194.

Xu, H., 2006. Modification of normalised difference water index (NDWI) to enhance open water features in remotely sensed imagery. *International Journal of Remote Sensing*, 27(14), pp.3025–3033.

Zhang, M. et al., 2010. Retrieval of total suspended matter concentration in the Yellow and East China Seas from MODIS imagery. *Remote Sensing of Environment*, 114(2), pp.392–403.

Zhu, W. et al., 2014. An assessment of remote sensing algorithms for colored dissolved organic matter in complex freshwater environments. *Remote Sensing of Environment*, 140, pp.766–778.